



UNIVERSIDAD DE MURCIA

ESCUELA INTERNACIONAL DE DOCTORADO

**Adaptive Optics Visual Simulators to Study the
Impact of Aberrations on Perception**

**Simuladores Visuales de Óptica Adaptativa para
Estudiar el Impacto de las Aberraciones en la
Percepción**

**D. Nikolai Suchkov
2019**

UNIVERSIDAD DE
MURCIA



Universidad de Murcia

Departamento de Física

Laboratorio de Óptica

**ADAPTIVE OPTICS VISUAL SIMULATORS TO STUDY THE
IMPACT OF ABERRATIONS ON PERCEPTION**

**SIMULADORES VISUALES DE ÓPTICA ADAPTATIVA PARA
ESTUDIAR EL IMPACTO DE LAS ABERRACIONES EN LA
PERCEPCIÓN**

*Thesis presented at the Faculty of Medicine
of the University of Murcia by:*

Nikolai Suchkov

To attain the degree of PhD from the University of Murcia.

Laboratorio de Óptica. Departamento de Física. Universidad de Murcia.
September 2019

Summary

Prevalence of myopia has been steadily increasing worldwide. High levels of myopia carry extra risk, tied to the increased possibility of pathological changes in the eye. The optical effects of myopia have been intensively studied. However, the neural component of vision has been scarcely considered in this context. Adaptive optics visual simulators (AOVS) allow to understand the effect of optical changes on vision, but most of them are not suitable to high myopes due to their limited measurement and modulation range.

An adaptive optics visual simulator (AOVS) with enhanced capabilities has been developed in this thesis. A wide dioptric range was developed allowing to expand the application of adaptive optics techniques to highly myopic patients. The working range was extended by separating the tasks of defocus-only phase modulation and modulation of high-order aberrations (HOA). An electrically tunable lens was used for defocus manipulation, while a liquid-crystal-on-silicon spatial light modulator (LCoS-SLM) was used for HOA correction and manipulation in general. A tunable lens was placed in a conjugated plane before a Hartmann-Shack sensor, allowing pre-compensation of defocus before wavefront measurements. A digital video-projector was used as a stimulus generator providing photopic conditions for the visual testing. Pupil diameter control was implemented by a motorized diaphragm, covering any physiological pupil size. A detailed description of the developed AOVS is provided in the thesis, followed by a description of thorough calibration procedures for individual components and the complete system itself.

Proof-of-concept measurements were done in young adults with high myopia. The visual acuity (VA) was compared using refraction obtained with AOVS and manifest refraction provided by the subjects. VA values when correcting AOVS-obtained refraction was consistently higher than with correction of manifest refraction. HOA of high myopes were also analyzed, being similar to the values found in emmetropic and low myopic eyes. VA was also obtained for some of the subjects with full wavefront correction, showing a moderate increase.

Separation of defocus modulation from the rest of phase modulation in the developed instrument has allowed to use diffractive phase masks for longitudinal chromatic aberration (LCA) control. Some aspects of the visual effect of modified LCA are not yet completely understood. As the LCA value is predictable, a number of studies have demonstrated its correction. However, some of them found an improvement of VA, while the others did not find a significant difference in visual performance. The visual performance through the depth-of-focus of the human eye under corrected LCA conditions hasn't been explored.

VA was evaluated through-focus under different modified LCA conditions. Correction of LCA did not provided an increase in through-focus VA, while doubling of the LCA further degraded it. Ray-tracing simulations of the studied LCA conditions coupled with a chromatic eye model was done in order to better understand the experimental results. A semi-empirical equation was used to predict VA values from the optical quality parameters obtained from the model. Simulations have predicted the behavior of VA in the natural LCA case, showcasing the feasibility of the method. In modified LCA conditions, the correlation between predicted and experimental VA values have dropped. A more drastic drop was found in the doubled LCA case. These results suggest that neural and visual compensation phenomena can exist for the natural LCA case.

For a deeper understanding of potential neural compensation mechanism for LCA of the eye, an additional experiment was done. VA was measured continuously for an extended period of time in low and high contrast for natural and corrected LCA. Analysis of the data has shown that in the high contrast conditions there was no evolution of VA through time, with VA being lower for corrected LCA. In low contrast, VA increased in corrected LCA case after time, despite an initial drop compared to natural LCA. These findings suggest that some neural adaptation to LCA exists, affecting vision in modified LCA conditions. The instrument extends the benefits of adaptive optics for visual simulation to high myopes, allowing to evaluate their visual performance. Experiments done in modified LCA conditions have shown an existence of neural adaptation to different LCA states, resulting in practical implications for the design of optical aids for the eye.

Resumen

La miopía es un error refractivo que ha experimentado un gran crecimiento, un cuanto a lo que respecta a su incidencia, en todo el mundo. Estos elevados valores de incidencia de la miopía llevan aparejados un alto riesgo en el incremento de cambios patológicos en el ojo que los sufre. Los cambios que la miopía produce en el ojo, que fundamentalmente se manifiestan en su carácter óptico, son bien conocidos y estudiados desde hace tiempo. No ocurre lo mismo sin embargo con la posible relación de estos cambios con las características neuronales de la visión. Los sistemas ópticos denominados simuladores visuales de óptica adaptativa (AOVS) constituyen una plataforma experimental que permite estudiar, y consecuentemente llegar a entender, los efectos que eventualmente producen los cambios ópticos sobre la visión de los sujetos. Se da la circunstancia de que la mayoría de este tipo de sistemas ópticos no pueden ser usados en aquellos casos que están afectados por niveles altos de miopía. Esto ocurre debido principalmente a las limitaciones técnicas en la medida de la calidad óptica, cuya amplitud es siempre finita, y a los rangos típicos de modulación de fase que se requerirían para actuar sobre dicha amplitud. En esta tesis se describe en detalle el diseño, desarrollo, y calibración de un sistema original del tipo simulador visual de óptica adaptativa dotado de un rango más amplio de manipulación del desenfoque, lo que posibilita de manera natural la medida de pacientes afectados por altos valores de miopía. Además de la medida, el sistema experimental basado en la óptica adaptativa también es capaz de manipular esta miopía, fundamentalmente llevar a cabo su corrección, de manera precisa. Estas características permiten el empleo del sistema óptico en diversas aplicaciones nunca antes exploradas, así como realizar experimentos que hasta la fecha no habían podido ser puestos en práctica. La ampliación del rango útil de trabajo del simulador visual que se ha conseguido en este trabajo se ha alcanzado mediante la separación del problema a resolver en dos partes bien diferenciadas: por un lado, la modulación de fase debida al desenfoque, y en el otro las aberraciones de alto orden (HOA).

Para la corrección, o en general manipulación, del desenfoque se utilizó una lente de potencia variable. Esta lente puede controlarse a través de un ordenador, empleando para ello las señales de voltaje que se envían

a través de cualquiera de los puertos de comunicación usuales. La lente posee un fluido que está contenido dentro del volumen limitado por una delgada membrana con características electrostáticas. Así, mediante la acción de un determinado campo eléctrico, la membrana cambia la forma de su superficie, alterando consecuentemente la potencia óptica del conjunto.

La corrección de las aberraciones de alto orden, conocidas en la literatura como high order aberrations, o también de manera simplificada mediante sus siglas HOA, se planteó mediante la acción de un dispositivo distinto. Para este fin se incorporó en el simulador óptico un sistema electro óptico del tipo conocido como modulador de fase programable (en la literatura especializada se emplea el acrónimo PPM del inglés Programmable Phase Modulator). Este elemento consta de una capa de cristal líquido, en contacto con el chip de silicio que recibe las señales eléctricas. Estos dispositivos son conocidos en la literatura como Liquid Cristal on Silicon Spatial Light Modulators (LCoS-SLM). El principio de funcionamiento de estos dispositivos se basa en la variación controlada, y de forma espacialmente resuelta, del índice de refracción del cristal líquido. El cristal líquido es un material con características ópticas muy peculiares. En particular, en este trabajo se empleó uno del tipo conocido como cristal líquido nemático. Este material está formado por cadenas de polímeros de gran longitud, en el contexto de la química molecular, con una orientación bien definida, y generalmente dada por la geometría del elemento físico que lo contiene. Estas cadenas de moléculas tienen la propiedad de realizar un giro o torsión en respuesta, y de manera proporcional y predecible, a la acción de un campo eléctrico externo. La disposición de las moléculas hace que el material presente propiedades de birrefringencia. Esto supone que el índice de refracción muestra dos valores diferenciados en función de la polarización de la luz incidente. El índice de refracción que se modifica mediante la rotación de las cadenas de polímeros corresponde al de la luz cuyo plano de vibración, o polarización, es paralelo a dichas cadenas moleculares. La luz con la otra polarización no resulta afectada por la rotación de las moléculas. De este modo, para el empleo de estos dispositivos es necesario operar con luz linealmente polarizada en la dirección correcta. Dado que el campo eléctrico actúa sobre la rotación de las moléculas, este puede ser aplicado de forma local, por lo que la alteración del índice de refracción de produce

en un determinado espacio. Este es de manera fundamental el principio de operación del modulador de fase. El chip de silicio recibe distintas señales eléctricas sobre cada uno de los píxeles o elementos básicos, de modo que el índice de refracción es modificado de manera singular sobre el espacio en contacto con el píxel. La modificación de la fase se lleva a cabo por tanto alterando el camino óptico que la luz que incide en el dispositivo. El estado actual de la técnica permite comprimir en un pequeño espacio gran cantidad de píxeles, por lo que resoluciones de varios millones de elementos son posibles.

Para la operación conjunta de la lente ajustable encargada de la manipulación del desenfoque y el modulador de fase basado en el cristal líquido es necesario conjugarlos ópticamente. Con esto se consigue que su efecto neto combinado sea equivalente al que produciría un hipotético corrector capaz de manipular todas las aberraciones de manera simultánea.

Uno de los elementos cruciales en un simulador visual de óptica adaptativa es el sensor de frente de onda. En este trabajo se incorporó al sistema experimental un sensor del tipo Hartmann-Shack. El nombre de este sensor hace honor a su inventor y al investigador que proporcionó la modificación del concepto que lo hizo útil para aplicaciones que involucraran poca intensidad. Este sensor es actualmente uno de los más empleados, en particular en el ámbito de las ciencias de la visión. Su relativamente sencillo funcionamiento y fácil implementación práctica lo han popularizado en muchos campos. El principio de operación del sensor se basa en un muestreo del frente de onda a través de una red de microlentes, que producen una imagen en su foco. Este se hace coincidir sobre la superficie de un sensor, típicamente una cámara CCD o CMOS. Cuando la porción del frente de onda muestreada por una determinada microlente es perpendicular al eje óptico de esta, la imagen se produce sobre el propio eje óptico. Esta imagen, sin embargo, sufre un desplazamiento si la porción del haz muestreado presenta una inclinación con respecto al eje óptico. El desplazamiento de la imagen focal puede emplearse para recuperar la pendiente local del frente de onda. Cuando esta operación se realiza a través de varias microlentes, puede reconstruirse el frente de onda incidente sobre el sensor. De nuevo, para una correcta medida del sensor, se hace necesario colocar este sobre la

pupila a través de la cual se quieren estimar las aberraciones. En el caso concreto del ojo humano, esta no es sino la pupila de salida, que es la imagen virtual que produce la córnea del iris. Debido a la imposibilidad de colocar el sensor en ese plano, se emplea la conjugación óptica, realizando imagen de dicho plano sobre la superficie del sensor. Con el fin de poder controlar la generación de aberraciones, tanto el plano del modulador de fase como el de la lente ajustable deben estar conjugados. Además de entre sí, deben estarlo con la superficie del sensor de Hartmann-Shack. Esto permite por ejemplo compensar el desenfoque, e ir refinando la medida del sensor, de modo que la estimación final prácticamente no muestre desenfoque. En el caso particular de la medida de pacientes con gran miopía esto resulta crítico. En efecto, el sensor de Hartmann-Shack exhibe un rango de operación lineal, superado el cual sigue proporcionando una estimación del frente de onda incidente, pero afectada por un error dependiente de la amplitud del desplazamiento de la imagen focal de cada microlente. Así, resulta muy conveniente medir siempre en condiciones de mínima desviación, para garantizar la operación lineal del sensor.

Con el fin de medir la visión, es necesario realizar medidas que involucren la percepción del sujeto. En este trabajo, se estudiaron fundamentalmente condiciones de iluminación fotópicas. Para asegurar estas condiciones de gran iluminación, como por ejemplo las que se tienen de manera natural durante el día con luz natural, se empleó un proyector de video digital, encargado de generar los estímulos. El control del diámetro de la pupila se llevó a cabo mediante la implementación de un diafragma motorizado, cubriendo así cualquier tamaño fisiológico de pupila. En esta tesis, se proporciona una descripción detallada del desarrollo del simulador visual de óptica adaptativa, además de los procedimientos para la calibración de cada componente del sistema y del sistema en conjunto. Se realizaron medidas en adultos jóvenes con alta miopía. La agudeza visual se comparó utilizando la refracción obtenida con el simulador visual y la refracción proporcionada por los sujetos. Los valores de agudeza visual cuando la refracción obtenida mediante el simulador visual estaba corregida eran mayores que cuando se compensaba la refracción proporcionada por el sujeto, y obtenida mediante el procedimiento habitual de lentes de prueba o un foróptero. Las

aberraciones de alto orden en sujetos con alta miopía también fueron analizadas, obteniendo resultados similares a los medidos en ojos emétopes o con baja miopía. Asimismo, la agudeza visual con corrección de todo el frente de onda se midió para algunos de los sujetos, mostrando un incremento moderado. La separación de la modulación del desenfoque del resto de la modulación de fase ha permitido el uso de máscaras de difracción de fase para el control de la aberración cromática longitudinal (LCA). Algunos de los efectos visuales de las modificaciones de aberración cromática longitudinal aún no se comprenden del todo. Dado que el valor de aberración cromática longitudinal es predecible, numerosos estudios han demostrado cómo corregirlo. Sin embargo, algunos de ellos han observado una mejora de la agudeza visual mientras que otros no han encontrado ninguna diferencia significativa en la función visual tras la corrección. La agudeza visual para distintos desenfoques con la aberración cromática longitudinal corregida no ha sido estudiada aún. En este trabajo, la agudeza visual se evaluó bajo diferentes condiciones de aberración cromática longitudinal. La corrección de la aberración cromática longitudinal no provocó ningún incremento de la agudeza visual, mientras que doblando el valor de la aberración cromática longitudinal la agudeza visual se degradaba aún más. Para comprender mejor los resultados experimentales se realizaron simulaciones de trazado de rayos de las condiciones de aberración cromática longitudinal estudiadas en un modelo cromático de ojo. Se utilizó una ecuación semiempírica para predecir los valores de agudeza visual a partir de los parámetros de calidad óptica obtenidos del modelo. Las simulaciones predicen el comportamiento de la agudeza visual en el caso de aberración cromática longitudinal natural, demostrando la viabilidad del método. En condiciones de aberración cromática longitudinal modificada, la correlación entre los valores de agudeza predichos y experimentales decrece. Una disminución aún mayor de los valores de agudeza visual se observa en el caso de aberración cromática longitudinal doble. Estos resultados sugieren que puede haber fenómenos de adaptación neural en el caso de aberración cromática longitudinal natural. Se realizaron otros experimentos para tratar de entender mejor el mecanismo de compensación neural para la aberración cromática longitudinal en el ojo. La agudeza visual fue medida de manera continuada durante un determinado período de tiempo con alto y bajo contraste

para los casos de aberración cromática longitudinal natural y corregida. El análisis de los datos muestra que en condiciones de alto contraste no hubo cambios temporales de la agudeza visual, siendo la agudeza visual menor para la aberración cromática longitudinal corregida. Para bajo contraste, la agudeza visual se incrementó con el tiempo en el caso de la aberración cromática longitudinal corregida, a pesar de la caída inicial en comparación con la aberración cromática longitudinal natural. Estos hallazgos sugieren que existe cierta adaptación neural a la aberración cromática longitudinal, lo cual afecta la visión en casos de aberración cromática longitudinal modificada. El dispositivo desarrollado en este trabajo extiende a los miopes de alta graduación los beneficios de la óptica adaptativa para simulación visual, permitiendo evaluar así su función visual. Los experimentos realizados en condiciones de aberración cromática longitudinal modificada muestran la existencia de adaptación neural a diferentes estados de aberración cromática, lo cual conlleva implicaciones prácticas para el diseño de dispositivos de ayuda óptica para el ojo.

Contents

Summary	iii
Resumen	v
List of Figures	xv
1 Introduction	1
1.1 Anatomy of the eye	3
1.1.1 Cornea	3
1.1.2 Iris	4
1.1.3 Crystalline lens	4
1.1.4 Retina	6
1.2 Optical quality of the eye	9
1.2.1 Monochromatic aberrations	9
1.2.2 Myopia	13
1.2.2.1 Prevalence of myopia	13
1.2.2.2 Optical quality of myopic eyes	15
1.2.3 Chromatic aberrations	15
1.2.4 Modified LCA and its influence on vision	17
1.3 Adaptive optics	19
1.3.1 Applications in the eye	20
1.3.2 Wavefront measurement	22
1.3.3 Wavefront modulation	23
1.3.4 Psychophysics for AOVS	25
1.4 Motivation	27
2 Methods	29
2.1 Wide-range adaptive optics visual simulator	30
2.1.1 Measurement relay	31

2.1.2	Visual simulation relay	34
2.1.3	Pupil monitoring	36
2.2	System operation	37
2.3	System alignment	40
2.4	Hartmann-Shack wavefront sensor	43
2.5	LCoS-SLM	45
2.5.1	Linearization	46
2.5.2	Centering	48
2.5.3	Polarization setting	50
2.5.4	Phase flicker	51
2.6	Tunable lens	53
2.6.1	Hysteresis and lens control	55
2.6.2	Temperature control	59
2.6.3	Optical quality	60
2.6.4	Predictability of the response among distinct TL units	61
2.7	Stimulus projector	63
3	Experiments	67
3.1	Measurements of high myopes	68
3.1.1	Subjects	68
3.1.2	Aberrometry	69
3.1.3	Visual quality with AO correction	70
3.1.4	Discussion	74
3.2	Vision through modified longitudinal chromatic aberration (LCA)	77
3.2.1	Experimental measurements	78
3.2.1.1	Subjects	80
3.2.1.2	Validation of the chromatic shift	80
3.2.1.3	Through-focus VA measurements	83
3.2.2	Ray-tracing simulations	84
3.2.2.1	Optical model	84
3.2.2.2	VA prediction	88
3.2.3	Discussion	90
3.3	Adaptation to corrected LCA	94
3.3.1	Experimental procedure	94

3.3.2	Subjects	95
3.3.3	Results	95
3.3.4	Discussion	98
4	Conclusions	101
	Acknowledgements	121

List of Figures

1.1	Horizontal cross-section of the eye	3
1.2	Structure of the crystalline lens	5
1.3	Absorption of photoreceptors in the retina	7
1.4	Zernike polynomials up to 6 th order	12
1.5	Chromatic aberrations of the eye	16
1.6	LCA of the eye	17
1.7	Schematic of a basic AO system	20
1.8	Working principle of a Hartmann-Shack sensor	23
1.9	Schematic of a typical LCoS-SLM	25
2.1	Full schematic of the system	30
2.2	Simplified schematic of the system	31
2.3	Measurement relay of the system	32
2.4	Visual relay of the AOVS	34
2.5	Interface of the control software of AOVS	37
2.6	Determination of VA from the test responses	38
2.7	Setup for calibration of the AOVS	41
2.8	EFFL measurement of HS sensor	43
2.9	Photo of the LCoS-SLM used in AOVS	45
2.10	Interface of the software for controlling the gamma curve of the LCoS-SLM	46
2.11	LCoS-SLM linearization setup	47
2.12	LCoS-SLM linearization	48
2.13	Graphical representation of centering of a digital pupil on an LCoS-SLM	49
2.14	LCoS-SLM pupil centering setup	50
2.15	Ghost metric along the two axes	51
2.16	Ghost metric for varying polarization axis	52

2.17	Comparison of ghost metric for different control sequences and different discretization levels	53
2.18	Schematic of Optotune EL-16-40-20D	55
2.19	Hysteresis exhibited by the tunable lens	56
2.20	Final tunable lens control function	57
2.21	Tunable lens response after the calibration	58
2.22	Shift of principal planes in the Optotune lens	58
2.23	Temperature testing of Optotune lens	59
2.24	Zernike polynomials representing high order aberrations produced by the tunable lens	60
2.25	Calibration defocus curves for three different units of the TL .	61
2.26	Stimulus projector - DLP4710EVM	63
2.27	Working principle of a digital micromirror device	64
2.28	Normalized spectrum of the DLP with input currents set at 1 A	64
3.1	Zernike polynomials of participating subjects	71
3.2	Comparison of RMS wavefront errors of normal population to participating high myopes	71
3.3	Visual acuities exhibited by the subjects	72
3.4	Optical quality of subjects S5, S6 and S7	73
3.5	VA values achieved by subjects S5, S6 and S7	74
3.6	Representation of the three chromatic conditions used in the experiment	78
3.7	Theoretical produced defocus as a function of the wavelength in the visible range	79
3.8	Experimental measurements of chromatic shift	81
3.9	Measured chromatic shift for compensation and doubling of the eye's LCA	82
3.10	Averaged measured LCA curves for four subjects	82
3.11	Average VA across the depth-of-focus for four subjects	84
3.12	Spectral weighting function used for the simulations	86
3.13	LCA produced in ray tracing simulations	87
3.14	Weighted MTF area calculation	89
3.15	MTF area and predicted VA values comparison	89
3.16	Comparison between predicted VA for different eye models .	92

3.17 Visual acuity from simulations and experimental measurements	92
3.18 Visual acuity measured through time in high contrast	95
3.19 Visual acuity measured through time in low contrast	96
3.20 Adaptation to compensated LCA for subjects S1, S3, S4 and S5	99

1 Introduction

Human vision is a sophisticated and fascinating system involving different mechanisms and processes. The vision starts with the light coming from a stimulus which is projected onto the retina by the optics of the eye. The information received by the photoreceptors in the retina is then processed and transmitted to the brain. Then, the final perception of the scene is accomplished by the brain through psychological mechanisms. Each part involved in vision is equally important for the correct perception of the scene. The complexity of each visual step typically yields to its individual characterization, although the interactions and connections among them are also crucial, for the correct understanding of the entire process.

Optically, the human eye is relatively simple and is often compared to an optical camera. It includes the imaging optics - the cornea and the crystalline lens, the iris to limit the amount of light forming images, similar to a diaphragm, and the retina, acting as the light sensor. The eye can also change its refractive power to focus at the objects placed at different distances. This is known as accommodation, and, once again, it resembles focusing optics in photographic cameras.

The resemblance of the eye with a photographic camera has been a classic topic, possibly initiated by Helmholtz in his now famous quote: "Now it is not too much to say that if an optician wanted to sell me an instrument which had all these defects, I should think myself quite justified in blaming his carelessness in the strongest terms, and giving him back his instrument" (Helmholtz, 1873). However, disregarding the apparent faults of the eye as an optical instrument, which is one of the topics of this Thesis, the eye is still a very robust and adaptable system (Artal, Benito, and Tabernero, 2006), capable of detecting scarce amounts of light (Rose, 1948), and operating in a wide range of different luminance levels.

Helmholtz further debated that any of the faults of the eye should be apparent, however they do not affect the normal visual performance. Because

of this, it is important to consider optical, neural and perceptual aspects of vision as a whole in vision research.

This introductory chapter will start with a general description of the eye and the visual system. It will be followed by a closer look at the topics on which this work will focus on later: high myopia, and the chromatic aberration of the eye and its impact on vision. An introduction to adaptive optics for visual simulation, the experimental technique developed in this work, will be provided. A general overview of the methods for characterizing the visual function will also be presented.

1.1 Anatomy of the eye

The normal eye, taken as a whole, has a near-spherical shape, with a diameter of approximately 24 mm in a sagittal meridian (Atchison and Smith, 2000). The optical power of the emmetropic eye is around 60 D, although it varies across individuals. Figure 1.1 shows a horizontal cross-section of the human eye.

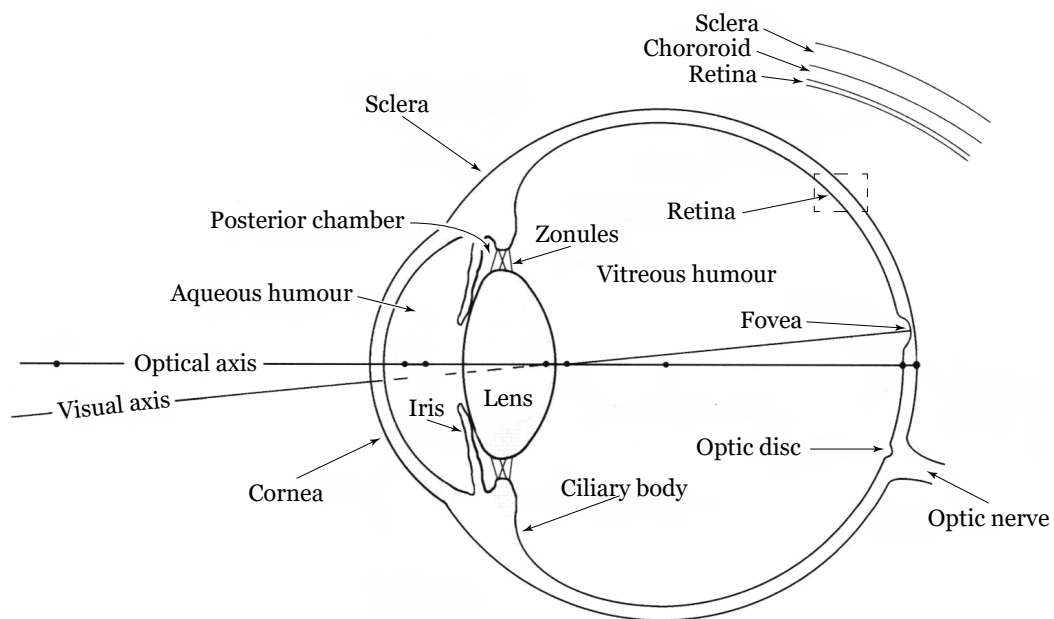


FIGURE 1.1: Horizontal cross-section of the eye. Figure adapted from Atchison and Smith, 2000.

1.1.1 Cornea

The outer part of the eye is composed by the cornea and the sclera. Sclera has a protective function. It shows a white and opaque aspect, and it is made of a dense fibrous tissue, compounded by several layers. The cornea is the first refractive element of the eye, with an optical power of approximately 42 D (Atchison and Smith, 2000), contributing around 2/3 of the total power of the eye. Most of the refractive power comes from the anterior surface of the cornea, where the largest change in refractive index (air-cornea) occurs.

The anterior surface of the cornea is aspheric, with increasing radius of curvature towards the periphery. The posterior cornea, exhibiting a resembling aspherical shape, separates the two media with rather similar refractive indexes (cornea-aqueous humor), so its optical power is modest compared to the anterior surface. Its optical power is around -7 D.

1.1.2 Iris

The posterior cornea limits the anterior chamber, a cavity filled with the aqueous humor. This chamber is posteriorly limited by the iris. The iris is a circular muscle with a central aperture called the pupil. This aperture acts as the effective aperture stop of the eye, taken as an optical system. It controls the amount of light entering the posterior part of the eye by adjusting its diameter. Physiological pupil diameter ranges from 2 to 8 mm (Atchison and Smith, 2000). The iris is controlled by two muscles, acting opposite of each other: sphincter pupillae, which contracts the pupil; and dilator pupillae, which dilates the pupil. The size of the pupil of the eye controls not just the amount of light, but also the optical quality of the images formed on the retina.

1.1.3 Crystalline lens

The posterior chamber is the space between the iris and the crystalline lens. The crystalline lens is the second important refractive element in the eye, for it contributes 1/3 of the total optical power (20 D). It is an aspheric bi-convex lens with an inhomogeneous refractive index structure. One of the most important property of the lens is the ability to change its shape and, consequently, its power during accommodation. The external shape of the lens continuously changes through the life span, as it keeps growing. Aside from the shape change, aging also results in a change of the refractive index structure (Hemenger, Garner, and Ooi, 1995), and in a reduction of its transparency (Boettner and Wolter, 1962). Eventually the loss of transmission and increase of scatter leads to age-related cataract. The mechanical properties of the lens also change with age, leading to the loss of accommodation, i.e., presbyopia. For younger people the aberrations between the

cornea and the lens compensate each other, especially the spherical aberration (Artal and Tabernero, 2008), but that balance gets disturbed with age as well.

The accommodation mechanism is controlled by the ciliary muscle. A set of zonular fibers connects the lens to the ciliary muscle. According to a widely accepted Helmholtz accommodation theory from 1855, forces applied to the crystalline lens change during the accommodation process by interactions between the ciliary muscle and choroid. Suspensory zonules transfer these forces to the crystalline lens itself and its capsule. When fixating at a near target, ciliary muscle contracts, which leads to anterior movement of the choroid and relaxation of the zonules suspending the crystalline lens. Due to the relaxation of the zonules, crystalline lens becomes thicker with lower radius of curvature, thus increasing optical power of the eye. When fixating to a far target, ciliary muscle relaxes resulting in a posterior retraction of the choroid, thus tightening the zonules and flattening the crystalline lens. Figure 1.2 shows the schematic of the lens and its accommodation system.

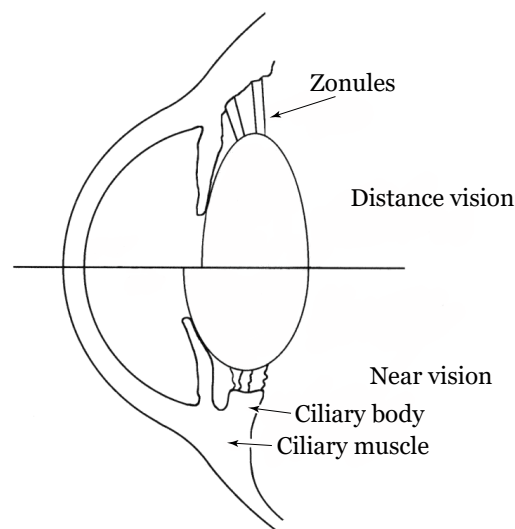


FIGURE 1.2: Structure of the crystalline lens. Figure adapted from Atchison and Smith, 2000.

1.1.4 Retina

Retina is a light-sensitive tissue that allows to gather the information contained in the images formed by the eye's optics. It is separated from the posterior surface of the crystalline lens by the vitreous chamber (approximately 16 mm in length), which contains the vitreous humor. This humor contributes up to the 80% of the total volume of the eye.

The human retina is formed by a large variety of cells organized in a very stratified manner. The cells responsible for the transduction of light from the images are the photoreceptors. There are two types of them: rods and cones. Rod photoreceptors are responsible for scotopic vision (dim lighting condition), while cone photoreceptors perform under photopic conditions. The combination of both types of photoreceptors allows vision to operate within a remarkable dynamic luminance range of approximately 12 log units. In addition, there are three types of cones (S, L and M) exhibiting different spectral sensitivity, whose combination enables color vision. Rods present the same spectral sensitivity, preventing the sensation of color to appear under low light conditions.

The absorption of the light within the rod photoreceptors is done by a special protein molecule known as rhodopsin, belonging to the wider type of photopsin molecules. The absorption peak of rhodopsin is around the 496 nm wavelength. Cones exhibit three different types of photopsins, corresponding to short, medium and long wavelengths (S-, M-, and L-cones), with absorption peaks at 419, 531, and 559 nm (Bowmaker and Dartnall, 1980). Figure 1.3 graphically shows the photoreceptors absorption curves. The relative amount of the cone types is individual, and it changes across the retina. Typical values are around 5% for S-cones, 30% for M-cones, and 65% for L-cones.

The number of rods in the human retina is significantly higher than that of the cones: 120 million versus 6 million, correspondingly. Their spatial distribution is also drastically different. The central part of the retina, known as the fovea centralis, consists solely of cones. Their number rapidly drops as eccentricity increases. As their distribution becomes scarce, the space between them is filled by the rods (Curcio et al., 1990). The spatial distribution and density of the photoreceptors limits the resolution of the eye. As the

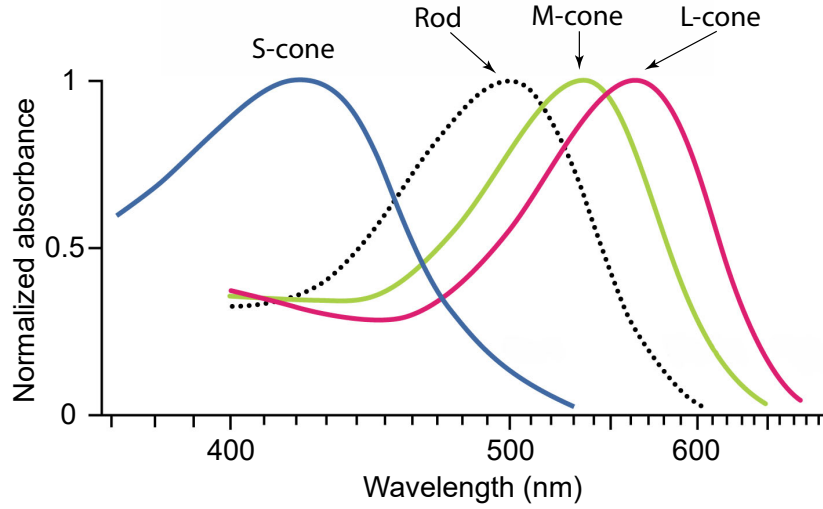


FIGURE 1.3: Absorption of photoreceptors in the retina.

sampling of the image on the retina is done discretely, the visual system is also affected by sampling artifacts, i.e. aliasing. The maximum resolvable spatial frequency satisfying the Nyquist criterion is around 60 cycles per degree at the fovea, rapidly dropping at the periphery (Anderson et al., 1991).

The ability of the light to excite a photopsin molecule depends on its incident direction. The photoreceptors act as a biological wave guide, resembling the directional properties of optical fibers. This circumstance is the origin of a phenomenon known as Stiles-Crawford effect. Back in 1933, Stiles and Crawford reported that the sensitivity of the eye was a function of the pupil location (Stiles and Crawford, 1933). The light visibility drops away from the point of maximum visibility, which is located close to the center of the pupil, typically displaced in the nasal direction by 0.5 mm (Aplegate and Lakshminarayanan, 1993). This behavior was fittingly named the Stiles-Crawford effect of the first kind (SCE-I). It is usually described by a Gaussian function: 1.1:

$$\eta(r) = 10^{-\rho r^2}, \quad (1.1)$$

where η is relative visibility, r - distance from the point of highest visibility, and ρ is the directionality parameter.

The SCE-I is typically modelled as a Gaussian apodization filter applied

to the entire pupil area. That affects the impact of optical aberrations on the final image, as well as the overall optical quality of the retinal images. SCE-I is included in some more comprehensive eye models.

Another effect of the directionality of the photoreceptors is described as Stiles-Crawford effect of the second kind (SCE-II) (Hansen, 1943). When the intensity of the light coming through an off-axis pupil point is adjusted to balance the brightness drop, there is an associate change in the perceived hue (Stiles, 1937).

1.2 Optical quality of the eye

The optical quality of the images projected on the retina depends on several factors: scattering, diffraction, and aberrations. Scattering is mainly generated by the crystalline lens, resulting in a diffusion that produces glare and reduces the contrast of the image. Scattering properties of the eye change with age, as the crystalline lens becomes more opaque, eventually leading to cataract, which is the leading cause of vision loss worldwide (Bourne et al., 2013). Diffraction is essentially produced by the edges of the pupil and affects the maximum resolving power of the eye, acting as a low pass filter for spatial frequencies of the image. The spatial cutoff frequency for an optical system without any aberrations is described by the Eq. 1.2:

$$f_C = \frac{1}{\lambda \cdot (f/D)}, \quad (1.2)$$

where f_C is the cutoff frequency (mm^{-1}), λ - wavelength (mm), f - focal length (mm), D - diameter of the entrance pupil (mm).

As seen from Eq. 1.2, the effect of the diffraction also depends on the pupil size, which is affected by the luminance conditions, alongside other factors.

As it has been mentioned in the beginning of the section 1.1, the human eye is not perfect, so it also suffers from optical aberrations. Those can be divided in two main groups: monochromatic and chromatic aberrations. The following sections will describe them with more detail.

1.2.1 Monochromatic aberrations

As in any optical system, monochromatic aberrations of the eye arise because of irregular shapes, misalignments of the optical surfaces relative to the optical axis, and inhomogeneities in the refractive indexes of the media. In the case of the eye, the most prominent sources of aberrations are the cornea, the crystalline lens, and the axial length of the eye. The so-called low-order aberrations: defocus and astigmatism exhibit the largest amplitude among the others in the normal eye. Defocus in the eye is referred to as ametropia, with myopia for the negative sign of defocus (an excess of power, shifting the image plane in front of the retina), and hyperopia for the

positive sign (a lack of power, shifting the image plane behind the retina). The eyes with no significant defocus and astigmatism (lower than 0.5 D) are referred to as emmetropic. It has to be mentioned that the optometric convention is to assign the signs of aberrations to be equal to the sign of the appropriate correction. Section 1.2.2 provides a closer insight to myopia in particular, its prevalence and associated complications.

Aside from the low-order aberrations, the eye also suffers from other high-order aberrations (HOA). Those are the aberrations associated with distortions of the wavefront of higher spatial frequencies. Due to the aberrations of the eye, rays entering the pupil through different areas are projected onto different areas of the image plane. These displacements are referred to as transverse aberrations (Born and Wolf, 1993). They are usually represented as wave aberrations, defined as deviations of the wavefront from a plane wave.

The combination of the wave aberrations exhibited by an optical system is usually described using a series of polynomials. Zernike polynomials are typically used to characterize the aberrations of the eye. Initially introduced by a Nobel laureate Frits Zernike in 1934 in the context of phase contrast imaging, it has become, over the years, a standard in ophthalmological research (Thibos, Bradley, and Zhang, 1991).

Zernike polynomials represent an orthogonal basis of functions defined for a circular pupil. The phase of any wavefront is then described as follows (in polar coordinates):

$$W(\rho, \theta) = \sum_{n=0}^{\infty} \sum_{m=-n}^n c_n^m Z_n^m(\rho, \theta), \quad (1.3)$$

where ρ is the normalized radial distance, θ is the radial angle, c_n^m are the Zernike coefficients, Z_n^m are Zernike polynomials, $n = 0, 1, 2, \dots, n$, and $m = -n, -n + 2, -n + 4, \dots, n$.

General form of Zernike polynomials is:

$$Z_n^m(\rho, \theta) = \begin{cases} N_n^m R_n^{|m|}(\rho) \cos(m\theta) & \text{for } m \geq 0, \\ -N_n^m R_n^{|m|}(\rho) \sin(m\theta) & \text{for } m < 0, \end{cases} \quad (1.4)$$

where $R_n^{|m|}(\rho)$ is the radial component and is calculated as follows:

$$R_n^{|m|}(\rho) = \sum_{s=0}^{\frac{n-|m|}{2}} \frac{(-1)^s (n-s)!}{s! \left(\frac{n+|m|}{2} - s\right) \left(\frac{n-|m|}{2} - s\right)!} \rho^{n-2s}, \quad (1.5)$$

N_n^m is a normalization factor:

$$\sqrt{\frac{2(n+1)}{1 + \delta_{m0}}}, \quad (1.6)$$

where δ_{m0} is the Kronecker delta (resulting in $\delta_{m0} = 1$ for $m = 0$ and in $\delta_{m0} = 0$ in other cases).

Figure 1.4 shows the graphical representation of Zernike polynomials up to 6th order.

Optometric refraction, i.e. defocus and astigmatism in diopters, can be calculated from Zernike polynomials using the following formulas (Thibos, Wheeler, and Horner, 1997; Thibos et al., 2004):

$$M = \frac{-c_2^0 4\sqrt{3}}{r^2}, \quad (1.7)$$

$$J_0 = \frac{-c_2^2 2\sqrt{6}}{r^2}, \quad (1.8)$$

$$J_{45} = \frac{-c_2^{-2} 2\sqrt{6}}{r^2}, \quad (1.9)$$

where coefficients are in micrometers, and r is the pupil radius in mm.

The methods of measurement of the wave aberrations of the eye are reviewed further in section 1.3.2.

A useful metric for describing quality of the wavefront is the root-mean square (RMS) wavefront error (Guirao and Williams, 2003). This is the standard deviation of the wave aberration. It can be calculated using the Zernike polynomial coefficients as follows:

$$RMS = \sqrt{\sum_{m,n} c_n^{m2}}, \quad (1.10)$$

As will be discussed in more detail in section 1.3.2, monochromatic aberrations are measured using a monochromatic light, most often in IR range.

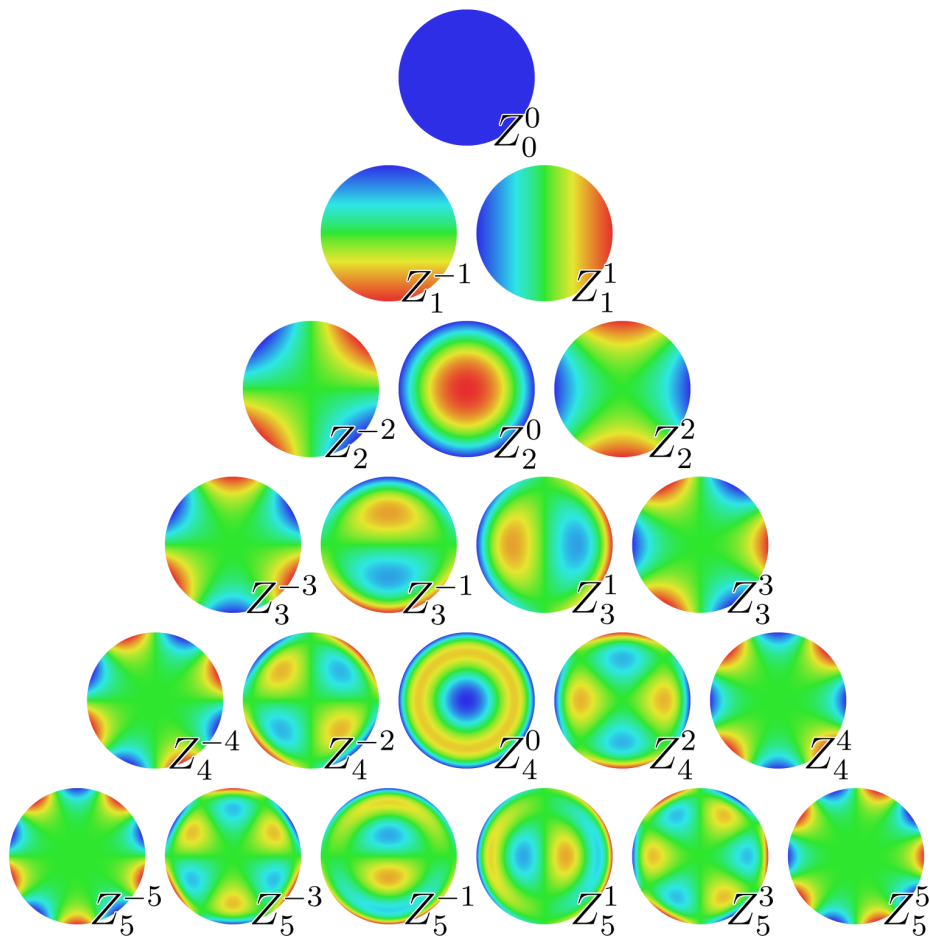


FIGURE 1.4: Zernike polynomials up to 6th order.

However, for evaluating the effect the aberrations would have on visual performance, it is necessary to consider them in visible spectrum. However, it has been experimentally shown that HOA measurements in NIR and in green light are nearly identical (Marcos et al., 1999; Llorente et al., 2003; Fernández et al., 2006b; Pérez-Merino et al., 2013). The only significant change occurs in defocus due to the longitudinal chromatic aberration of the eye (which will be discussed in section 1.2.3), and it can be calculated from the difference in wavelengths (Fernández et al., 2006b).

1.2.2 Myopia

Myopia is the leading cause for vision impairment worldwide, as well as the second most common cause of blindness (Bourne et al., 2013). The prevalence of myopia has rapidly grown in recent decades, especially in Asia, reaching epidemic levels (Holden et al., 2016). This section takes a closer look at myopia, its prevalence, associated dangers, and characterization.

Myopia is typically divided into two different groups, depending on its origin: axial myopia and refractive myopia. The first one refers to the defocus caused by the excessive axial elongation of the eye, accounting for the position of the retina, while the second one refers to the excessive power of the refractive surfaces of the eye (essentially cornea and crystalline lens) to form the images onto the retina. Actually, the distinction is mainly academic for both factors are typically associated to a certain extent, and in practice one can only speak of prevalence of a factor as compared to the other. In this context, axial myopia is more common, being the primary risk factor for myopia progression (Flitcroft et al., 2019).

For practical purposes, an additional classification based on the amplitude of the defocus is also used. Myopia in general is described as a refractive error of more than -0.5 D in the eye. High myopia refers to a higher amplitude of the refractive error, with the thresholds at -5 D (Holden et al., 2016) or -6 D (Flitcroft et al., 2019). In this Thesis, high myopia will be defined for cases where the equivalent sphere is below -5 D.

1.2.2.1 Prevalence of myopia

A study by Holden et al. estimates that the number of people suffering from myopia will rise from 2.5 billion people in 2019 to approximately 5 billion people (Holden et al., 2016) in 2050. The number of people affected by high myopia specifically will rise from 300 million people to almost 1 billion people in 2050. It is important to consider high myopia separately, as it drastically increases the risk of pathological changes, such as retinal detachment, myopic macular degeneration and glaucoma, causing permanent vision loss.

It should be noted that the prevalence of myopia heavily depends on the geographic area, and ethnic groups (Rose et al., 2008). As an example,

myopia is twice as common among East Asians compared to white Caucasians of similar ages (Pan et al., 2015). In countries with higher myopia prevalence, myopic macular degeneration is the leading cause of permanent blindness (Iwase et al., 2006).

The predictions assume that increased urbanization and development of countries will continue to spread the associated lifestyle changes, such as decreased time outdoors and increased near-work time (Morgan, Ohno-Matsui, and Saw, 2012). The so-called high-pressure educational systems in East Asian countries (e.g. Singapore, South Korea, China and Taiwan) seems also a factor in the growth of myopia prevalence.

High myopia is associated with a significantly increased risk of structural changes of the eye (Saw et al., 2005; Flitcroft et al., 2019). The term “pathologic myopia” is used to describe situations where high myopia levels have resulted in ocular irreversible changes. The myopia-associated excessive axial elongation of the eye leads to structural changes in the posterior segment, such as myopic maculopathy, high myopia-associated optic neuropathy, and retinal detachment. High myopia is the main risk factor to develop pathologic myopia, although it can also occur in lower levels of myopia.

Myopic macular degeneration develops due to posterior staphyloma (outward protrusion of all layers of the posterior eye globe) formation and progressive thinning of the RPE-choroid with age on top of the axial length increase. Myopic macular degeneration is defined as a vision threatening condition, occurring in people with high myopia, that comprises diffuse, patchy macular atrophy with or without lacquer cracks, CNV, and Fuchs’ spot (Flitcroft et al., 2019).

The axial elongation associated with highly myopic eyes often creates myopia-associated glaucoma-like optic nerve damage. This is defined as an optical neuropathy characterized by a loss of neuroretinal rim, and enlargement of the optic cup. This is typically occurring in highly myopic eyes with a secondary macro disc or peripapillary delta zone at a normal IOP (Flitcroft et al., 2019). Optical neuropathy causes irreversible loss of vision.

Retinal detachment is another common complication of high myopia. The risk increases with higher refractive error (Flitcroft, 2012) due to the changes in the peripheral retina. The risk of retinal detachment also greatly

increases with age, and can happen in non-myopic eyes as well, albeit at a much lower rate (Algvere, Jahnberg, and Textorius, 1999; Mitry et al., 2010).

1.2.2.2 Optical quality of myopic eyes

Studying HOA of the myopic eyes can potentially help to understand whether the retinal image quality has any impact on myopia development. Some studies did not find any correlation or difference between HOA and refractive error (Porter et al., 2001; Cheng et al., 2003) in large population groups. Other studies have found a higher amount of HOA in myopes compared to emmetropes (Collins, Wildsoet, and Atchison, 1995; He et al., 2002; Paquin, Hamam, and Simonet, 2002). Spherical aberration in particular have shown a significant correlation with refractive error (Collins, Wildsoet, and Atchison, 1995). Another open question is the visual performance of myopes and especially high myopes. While some studies have reported a decrease in visual acuity when myopia was corrected (Collins and Carney, 1990; Strang, Winn, and Bradley, 1998; Chui et al., 2005) and hypothesised that the decrease was due to retinal stretching; other studies did not find a decrease when refractive error was corrected with contact lenses (Collins and Carney, 1990). This suggests that this topic is still open, with age being a possible factor explaining the differences among studies.

1.2.3 Chromatic aberrations

Chromatic aberration appears as a consequence of the chromatic dispersion of the ocular media (Howarth and Bradley, 1986), producing a change in the aberrations as a function of wavelength. Chromatic aberration of the eye is typically divided in two components: longitudinal chromatic aberration (LCA); and transverse chromatic aberration (TCA). LCA results in a wavelength-dependent change of refractive power (Bedford and Wyszecki, 1947; Howarth and Bradley, 1986; Zhang, Thibos, and Bradley, 1997). TCA produces a wavelength-dependent change in magnification of extended image (Howarth, 1984; Thibos, Cheney, and Walsh, 1987; Thibos et al., 1990). While LCA have been reported to be relatively constant among subjects (Millidot, 1981; Thibos et al., 1990), TCA has a high variability (Rynders et

al., 1995), preventing its correction using average values. Figure 1.5 graphically describes the effect of chromatic aberrations.

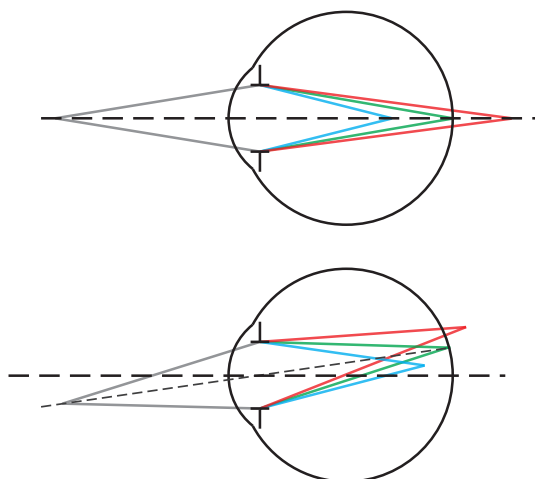


FIGURE 1.5: Chromatic aberrations of the eye. Top panel shows the LCA of the eye, bottom panel show the TCA of the eye.

The refractive index of the ocular media in the human eye is lower for the longer wavelengths than for the shorter ones. Due to that, if the eye is emmetropic for the green wavelength, it is myopic for blue light and hyperopic for the red light. The amplitude of LCA in the eye reaches almost 2 D across the visible spectrum (from 400 to 700 nm) (Campbell and Gubisch, 1967; Thibos et al., 1992; Atchison and Smith, 2005). On the basis of experimental measurements of the ocular LCA, Thibos et al. (Thibos et al., 1992) developed a first chromatic eye model. The model eye was calculated to be emmetropic for 589 nm (sodium D-line). Atchison et al. then improved upon the model and expanded it into the near IR (Atchison and Smith, 2005). Figure 1.6 shows the LCA of the eye, as measured in multiple studies.

In spite of its value, under normal viewing condition the effects of LCA are not noticeable. This fact suggests an existence of some perceptual mechanism compensating the distortion. The topic of chromatic aberration perception and its potential effects on vision will be discussed with more detail in the next section 1.2.4.

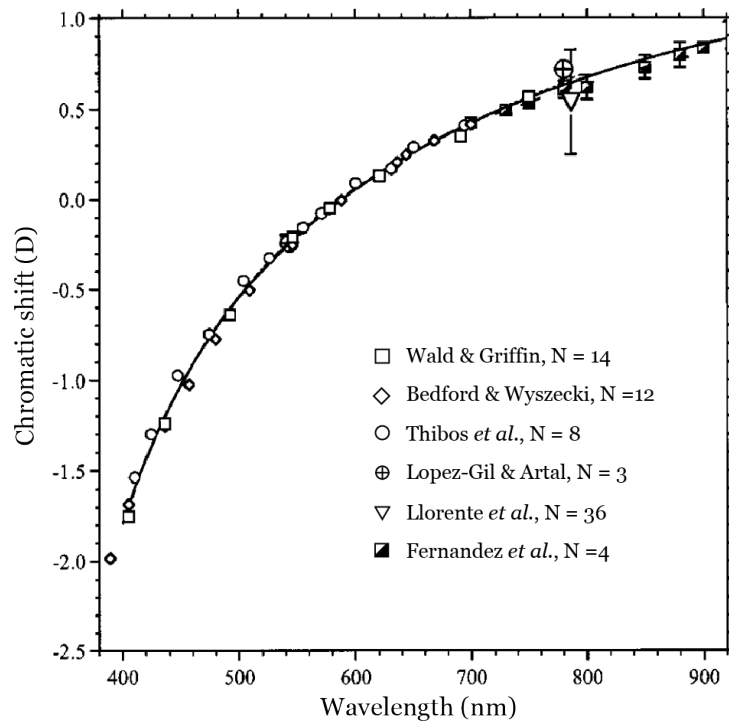


FIGURE 1.6: LCA of the eye. The data is shifted to 0 D at 590 nm. Solid line represents best-fit Cauchy equation. Figure adapted from Atchison and Smith, 2005

1.2.4 Modified LCA and its influence on vision

Given that the LCA can be considered approximately constant among subjects, its correction has been a classic topic in visual sciences for decades (Heel, 1946; Thomson and Wright, 1947; Powell, 1981; Howarth and Bradley, 1986; Bradley, Zhang, and Thibos, 1991; Zhang, Bradley, and Thibos, 1991; Yoon and Williams, 2002; Benny et al., 2007; Artal et al., 2010). Most of the attempts to correct LCA were accomplished by with using the so-called achromatizing lenses, which exhibit a LCA similar in magnitude to that from the eye, but with an opposite sign. The possibility of implementing LCA corrections in intraocular lenses (IOLs) has been also recently studied (Franchini, 2007; Fernández and Artal, 2017).

The effect of correcting LCA in visual performance remains controversial, as different studies have found distinct results. Some have reported a benefit in visual acuity (VA) and contrast sensitivity (CS) (Yoon and

Williams, 2002; Artal et al., 2010), while others did not find a significant improvement (Campbell and Gubisch, 1967; Thibos, 1987; Bradley, Zhang, and Thibos, 1991; Thibos, Bradley, and Zhang, 1991; Benny et al., 2007. This is a remarkable fact since from an optical perspective the benefit of correcting the chromatic aberration is considerable, well above the depth of focus of the eye (Campbell, 1957. Bradley et al. discussed the topic in detail (Bradley, Zhang, and Thibos, 1991), proposing some hypotheses to explain the lack of visual improvement. These can be summarized as follows: A) achromatizing lenses may correct the LCA incorrectly, B) Effect of LCA on image quality is insignificant, C) TCA has a greater effect on vision than LCA, D) achromatizing lenses introduce extra aberrations of the eye. Out of these hypotheses, two are related to the achromatizing lenses themselves, either their design (A) or decentering (D). These limitations are just technical ones, and they can be properly handled with the current technology and laboratory methods. Hypotheses (B) and (C) pertain to the optics of the eye, raising the question of to what extent LCA affects vision. The role of the spectral efficiency of the photoreceptors is implicit in this discussion, so photometric considerations should also be taken into account.

There are many aspects of vision affected by LCA. For example, it is well known that the color perception is affected by the LCA. Kruger et al. accomplished a number of experiments characterizing accommodation under different chromatic conditions (Kruger and Pola, 1986; Kruger et al., 1993; Aggarwala, Nowbotsing, and Kruger, 1995). LCA seems to be involved in many visual tasks. In order to fully understand the perception of light in modified LCA, there is a need to study the visual performance under tightly controlled experimental conditions.

1.3 Adaptive optics

When the light passes through an inhomogeneous medium, the wavefront gets distorted. A possibility of correction exists if the aberrations could be measured. The technique to measure and correct the optical aberrations is known as adaptive optics (AO). Initially the technique was proposed in 1953 by Babcock for astronomical applications (Babcock, 1953) in order to correct distortions introduced by the atmosphere on the astronomical images retrieved by ground-based telescopes.

The practical implementation of AO was accomplished in the 1970s (Hardy, Lefebvre, and Koliopoulos, 1977), using a shearing interferometer to measure the aberrations generated by a turbulent medium, and corrected them by a piezoelectric deformable mirror. Since then, the technique has been widely used in the field of astronomy. Normally, an artificial guide star is generated by a laser source from the ground to measure the aberrations induced by the atmosphere at any point of the sky. The correction is then performed by dedicated optics within the telescope.

The AO systems can be separated in two groups: open-loop and closed-loop systems. In closed-loop systems, measurement of aberrations and their modulation are done iteratively following a feedback loop. In open-loop systems, a single measurement of aberrations is done with a single correction, and no feedback is provided by the sensor. For closed-loop systems the wavefront sensor has to be located after the wavefront modulator in the path of the light. For open-loop systems, however, the wavefront sensor is typically located before the corrector.

The AO techniques were also applied to the study of the eye, starting from the 1990s. Similar to the implementation in astronomy, the aberrations are typically measured with the help of an artificial beacon light, which is a point-like spot emitting from the observer's retina. Normally, it is created by using a laser beam passing through the ocular media. AO provides an unprecedented platform to study the optics of the eye and its visual performance. Figure 1.7 graphically shows a basic layout of an AO system for the eye. AO concepts were first applied in the eye by Derher et al. in a laser scanning ophthalmoscope (Dreher, Bille, and Weinreb, 1989), where a deformable mirror was used for a static correction of ocular aberrations.

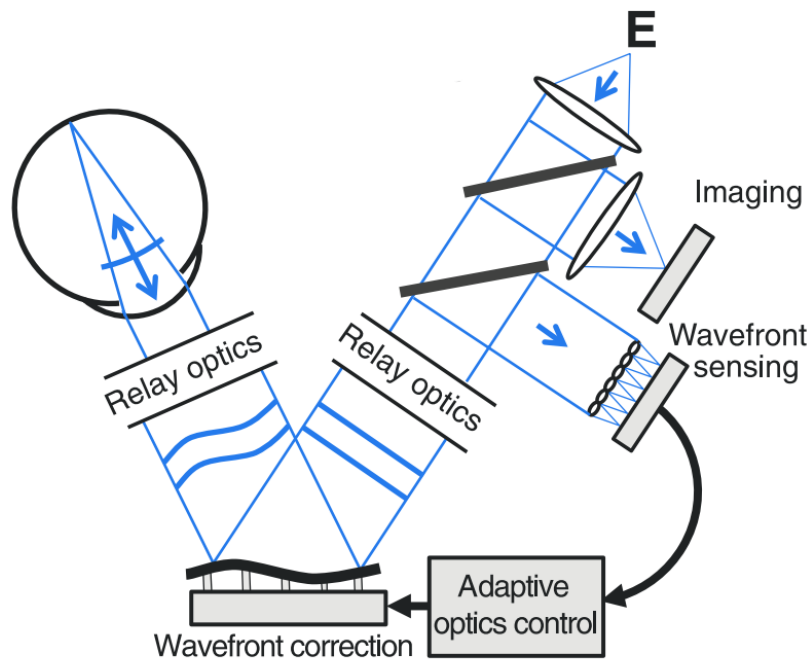


FIGURE 1.7: Schematic of a basic AO system. Adapted from Roorda, 2011.

1.3.1 Applications in the eye

AO applications in the eye can be divided into two categories: studies of retinal morphology and visual simulation.

In retinal morphology studies, usage of AO techniques allowed to produce a number of important results *in vivo*, as almost every imaging technique was merged with AO. One of the earliest beneficiaries were flood illumination fundus cameras, permitting *in vivo* recordings of photoreceptors mosaics (Roorda and Williams, 1999). Dynamic correction of aberrations of the eye using a closed-loop system was then demonstrated in 2001 (Hofer et al., 2001a), demonstrating an improvement in retinal images. A number of studies followed, analyzing the limitations of AO for retinal imaging (Doble et al., 2002; Fernández and Artal, 2003; Dalimier and Dainty, 2005; Miller, Thibos, and Hong, 2005; Fernández et al., 2006a). Combining AO with a laser scanning ophthalmoscope (SLO) allowed to drastically improve its performance Roorda et al., 2002. Optical coherence tomography (OCT) is another

technique which has massively benefitted from AO. The first implementation was done in 2003 (Miller et al., 2003), with a lot of works following (Hermann et al., 2004; Fernández and Artal, 2005; Fernández and Drexler, 2005; Fernández et al., 2005b; Merino et al., 2006; Zhang et al., 2006; Bigelow et al., 2007; Zawadzki et al., 2007). Systems combining OCT and SLO techniques employing AO were also described (Pircher et al., 2008 and Zawadzki et al., 2011).

Adaptive optics visual simulators (AOVS) combines the benefits of AO technology with vision testing, allowing to understand the correlation between optical quality and visual performance. Usage of adaptive optics for visual simulation started with correcting aberrations, allowing vision to reach its physiological limits (Liang, Williams, and Miller, 1997), where dramatic improvements of contrast sensitivity were demonstrated. Closed-loop correction of aberrations of the eye for visual simulation was demonstrated by Fernández et al. (Fernández, Iglesias, and Artal, 2001), allowing aberration control in real-time. Studies which followed had confirmed the benefits AO offered for VA and CS (Yoon and Williams, 2002; Artal et al., 2010; Li et al., 2009), and even for basic tasks such as facial recognition (Sawides et al., 2010b). AO showed to provide a benefit even for the peripheral optics, where a spatial resolution of photoreceptors seem to be the limiting factor (Lundström et al., 2007).

Using adaptive optics for visual simulation allowed to characterize the ability of visual system to adapt to certain monochromatic aberrations (Artal et al., 2003; Chen et al., 2007; Rossi et al., 2007; Sawides et al., 2010a; Venkataraman et al., 2015). One of the first experiment showing the importance of considering both of those vision modalities was shown by Artal et al., 2004, where a group of subjects were shown rotated patterns of the HOA. Subjects have achieved better visual performance with their own natural orientation of HOA, showcasing a degree of neural adaptation. Works by Sabesan et al. (Sabesan et al., 2007; Sabesan and Yoon, 2009; Sabesan and Yoon, 2010) have further explored the ability of visual system to adapt to aberrations of large amplitudes present in keratoconic eyes.

AOVS provide a useful testbed for advanced optical solutions, such as multi-zone contact lenses and intraocular lenses (IOLs), giving an opportunity to test a design and to evaluate its effect on vision even before the

production. AOVS were used to induce aberrations in order to evaluate their effect on visual performance. For instance, AOVS were used for studies of extending depth of focus for presbyopic eyes, evaluating a practical approach of intraocular lenses with induced spherical aberration (Piers et al., 2004; Piers et al., 2007; Artal et al., 2010; Villegas et al., 2014; Manzanera and Artal, 2016). Simulation of multifocal IOLs was also previously demonstrated (Radhakrishnan, Dorronsoro, and Marcos, 2016).

Adaptive optics visual simulators (AOVS) have continued to improve through the years, employing spatial light modulators for the aberration control in place of deformable mirrors (Vargas-Martín, Prieto, and Artal, 1998; Prieto et al., 2004; Manzanera et al., 2007; Cánovas et al., 2010, and extending the simulation to binocular vision (Fernández, Prieto, and Artal, 2009a; Fernández, Prieto, and Artal, 2010; Schwarz et al., 2011). A commercial AOVS was developed and is on the market today, enabling further vision research (VAO, Voptica S.L., Murcia, Spain) without the need of development of the instrument itself.

1.3.2 Wavefront measurement

One of the most extended method to estimate the ocular aberration uses sampling of the wavefront by means of a Hartmann-Shack (HS) sensor. There are other alternatives, already demonstrated in the context of physiological optics, such as a pyramid sensor (Iglesias et al., 2002; Chamot, Dainty, and Esposito, 2006; Daly and Dainty, 2010), or a curvature sensor (Roddier, 1988). The HS sensor was first proposed in 1971 (Platt and Shack, 1971), as a variation of the Hartmann test dramatically increasing signal to noise ratio, permitting its use with astronomical objects, where typically the photon flux is scarce. In 1994 the HS sensor was successfully applied for the first time in the human eye (Liang et al., 1994). Figure 1.8 graphically shows the working principle of a HS sensor.

A lenslet array, consisting of identical microlenses, samples the wavefront, projecting each image onto a camera sensor placed in the focal plane of the microlenses. When the wavefront is perfect, each lenslet produces a focal image at its optical axis. In the case of an aberrated incoming wavefront, the spots or focal images through each microlens are displaced from

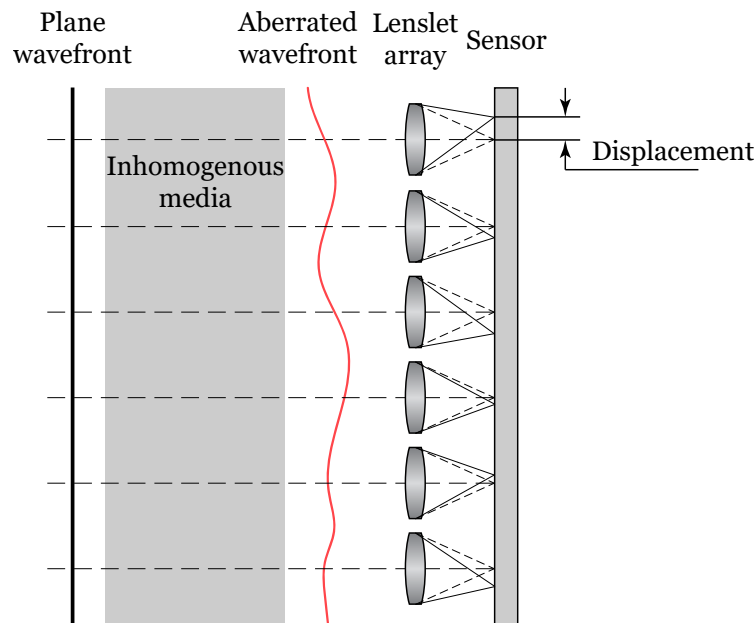


FIGURE 1.8: Working principle of a Hartmann-Shack sensor.

the centers of their optical axes. The magnitude and orientation of those displacements are then used to retrieve the local slope of the wavefront sampled by each microlens. Under certain contour and continuity constraints, the overall wavefront shape can then be estimated by merging the individual local slopes. An aberrated wavefront can also be used as a reference, in which case the deviation from that wavefront is measured.

1.3.3 Wavefront modulation

Wavefront modulators, or simply correctors, are devices that are able to change the incoming phase of the wavefront in a controlled manner. This action is typically accomplished by altering the optical path of the light. The use of such devices in AO systems is fundamental. The choice of a wavefront modulator is a critical part of the design of an AO system. Usually, it is also the most expensive element. Characteristics of the modulators like the spatial resolution and the temporal response, need to be carefully evaluated prior to their incorporation in an AO system, as they affect and eventually limit the performance of the instrument.

In the context of AO for visual sciences, there are two main types of wavefront modulators: deformable mirrors (DMs) and liquid crystal spatial light modulators (LC-SLMs).

DMs are devices that allow a fast control of the wavefront. DMs can be divided into three main types: membrane DMs, piezoelectric DMs (Liang, Williams, and Miller, 1997), and microelectromechanical (MEMS) DMs (Hofer et al., 2001b; Doble et al., 2002). Membrane type DMs can be further divided into electrostatically driven (Fernández and Artal, 2003) and magnetically driven types (Fernández et al., 2006a). MEMS DMs exhibit a small stroke resulting in lower range of phase modulation, but with a higher resolution compared to other types. Due to that difference in available stroke and precision, two DMs of different types are often used in a "woofer-tweeter" arrangement, with one DM taking care of aberrations with high amplitude, while the other one allows for a precise wavefront correction (Zou, Qi, and Burns, 2008). DMs typically have to operate in a closed-loop system to ensure accurate modulation (Fernández and Artal, 2003). A significant advantage of the DMs over LC-SLMs is their achromaticity.

LC-SLM devices introduce a phase retardation by locally changing the refractive index of the liquid crystal (LC) material. An applied voltage to an LC cell changes the orientation of the molecules inside. A typical device contains a large number of cells, or pixels (up to 8 million), allowing for a precise phase modulation. LC-SLMs operate either in transmission, or in reflection (e.g., liquid-crystal-on-silicon (LCoS) SLMs), with reflective SLMs exhibiting higher resolution. Although the stroke of a single SLM cell is not large (usually up to 4π , dependent on the wavelength), phase wrapping can be employed in order to extend the working range dramatically. The modulation depth changes with the wavelength, negatively affecting their performance in wide spectrum light. Figure 1.9 graphically shows a typical LCoS-SLM.

Lately LC-SLMs have been used more commonly, overcoming some of their limitations (Vargas-Martín, Prieto, and Artal, 1998; Prieto et al., 2004; Fernández et al., 2005b; Manzanera et al., 2007; Fernández, Prieto, and Artal, 2009b; Cánovas et al., 2010).

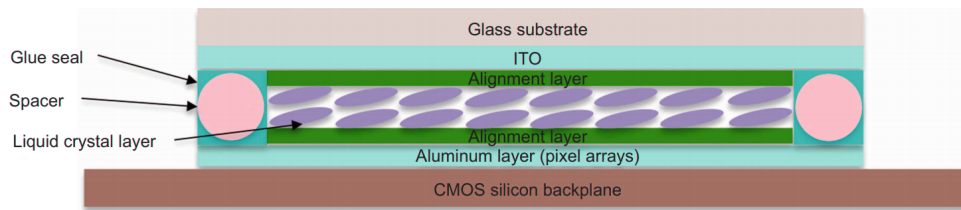


FIGURE 1.9: Schematic of a typical LCoS-SLM. Adapted from Zhang, You, and Chu, 2014.

Due to the high fidelity and stability of LC-SLMs, open loop operation is perfectly possible (Prieto et al., 2004). Due to their working principle of changing refractive index of LC material, LC-SLMs are wavelength-sensitive. Using them in white light or in polychromatic conditions in general requires special considerations, which will be later discussed in detail in this work. LC-SLMs also are able to generate discontinuous phase profiles, allowing to simulate complex optical profiles, for instance diffractive intraocular lenses (IOLs).

LC-SLMs were used in this work as a wavefront modulator of choice.

1.3.4 Psychophysics for AOVS

The final step of vision is the interpretation of the scenes. The perception of the visual images is a combination of complex phenomena occurring in the brain. Visual performance can be described by using detection thresholds for different visual functions, such as visual acuity (VA) or contrast sensitivity (CS). Those thresholds can be obtained by applying psychophysical methods.

Adaptive psychophysical methods are more efficient than constant stimuli methods in determining the visual thresholds (Watson and Fitzhugh, 1990). Instead of showing a pre-set stimuli values (e.g., size, contrast), adaptive methods adjust the value of the stimulus according to the responses of the subject. That allows to reach a threshold value with the same accuracy in a smaller number of trials. Some of the commonly used techniques are QUEST (Watson and Pelli, 1983) and PEST (Bach, 1996). The visual tasks to

characterize vision can be relatively simple ones. For visual acuity, for example, it can be the identification of letters of different sizes on the screen; for contrast sensitivity the task can be the detection of a grating of different spatial frequency and orientation. A single trial produces a right or wrong answer. The probability of correct responses can then be statistically estimated from a sufficient number of trials. In this work, the quality of vision was mostly estimated from visual acuity. The exact procedure will be discussed in section [2.2](#).

1.4 Motivation

One of the main goals of this work is to develop an adaptive optics visual simulator with a wide range of measurement and modulation, offering the benefits of adaptive optics technology to the highly myopic people. Myopia prevalence has been increasing for the last decades, especially in Asian countries, reaching epidemic levels. High myopia is especially dangerous, often leading to pathological complications. Changes in the morphology of the eye, and consequently, optics due to myopia are well known, but the neural aspect of vision also has to be considered. Adaptive optics visual simulators allow to account for the neural system and to determine the real visual impact of any aberrations, and, of course, myopia in particular.

Most conventional methods of wavefront modulation do not offer the dioptric range necessary for high myopes, so a combination of wavefront modulation devices needs to be implemented. The developed instrument needs to be compact and easy to use in order to allow future studies in clinics. Proof-of-concept measurements need to be done for evaluation of the capabilities of the developed system.

Another major topic investigated in this thesis is the effects of longitudinal chromatic aberration (LCA) on human vision. It is a controversial and not yet completely resolved topic. Despite being significant in its amplitude, LCA does not seem to have a considerable effect on visual performance. Number of studies didn't find any visual improvement when LCA was corrected, which goes against logic if only optical quality is considered. That seems to suggest that there is a neural mechanism affecting the perception of polychromatic light.

If the defocus modulation in the developed system is decoupled from the conventional liquid-crystal based modulator (LC-SLM), it would allow to use the LC-SLM for modifying the LCA of the observer's eye using diffractive profiles. In such case, visual performance should be evaluated through-focus for different chromatic conditions in order to better understand the effect of LCA on vision. A possibility of a neural adaptation mechanism existing should also be investigated.

2 Methods

This chapter provides a detailed description of the instrument, its calibration and various techniques used in this thesis. The developed instruments provided an extended defocus range of -12 to 10 D, with a changeable entrance pupil size, and a bright stimulus providing pure photopic conditions. The developed system itself was compact, providing a possibility of transfer into a clinical environment.

Section 2.1 gives a description of the instrument itself, with a closer look at its separate relays. Section 2.2 provides an explanation of the way the system was operated. Section 2.3 explains the optical alignment of the AOVS. Section 2.4 describes a used custom-made Hartmann-Shack wavefront sensor, and its calibration. Section 2.5 provides a detailed description of the LCoS-SLM with the calibration procedure. Section 2.6 describes the tunable lens used in the system. Finally, section 2.7 provides a look into the stimulus projector used in the system.

2.1 Wide-range adaptive optics visual simulator

The instrument was compounded by three main parts: measurement, visual simulation, and pupil monitoring relays. Subsections below will describe each relay in detail. The description of key components used in the relays are provided in a separate chapter 3.

Figure 2.1 shows the full schematic of the system, including the folding mirrors to reduce the size of the apparatus

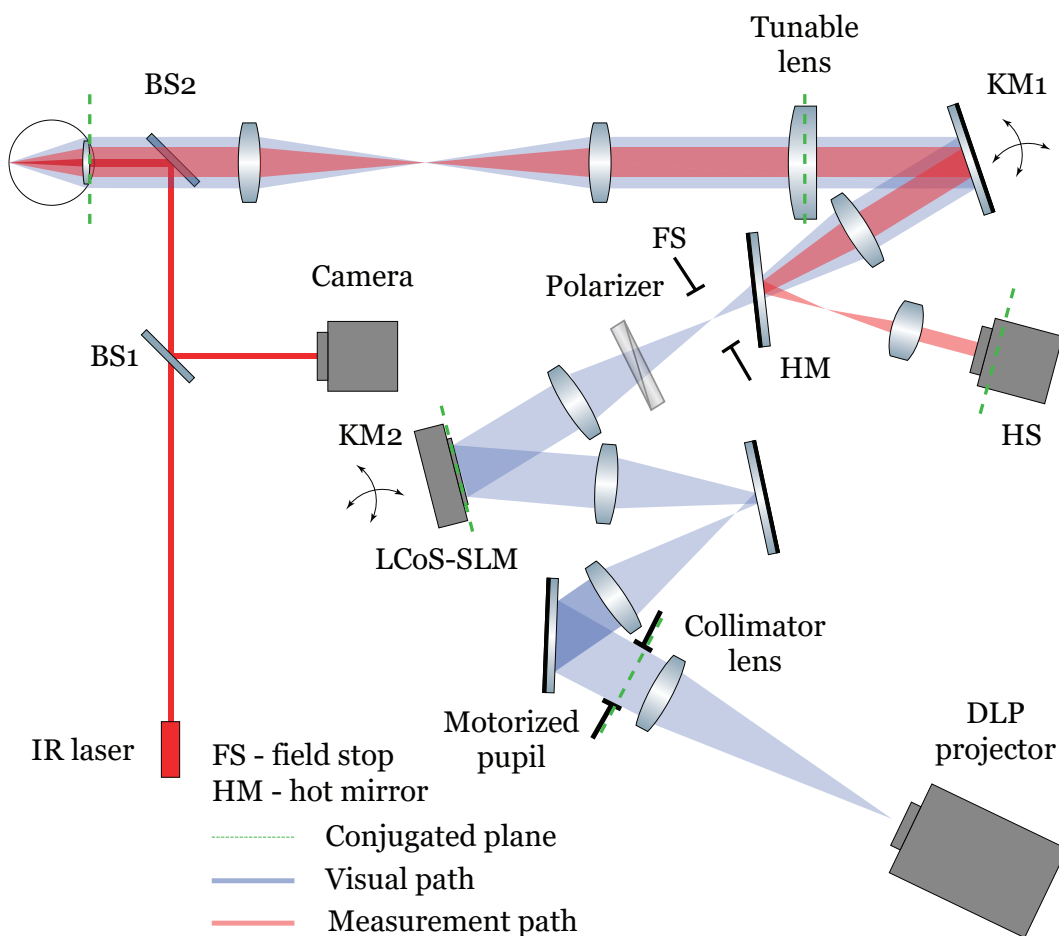


FIGURE 2.1: Full schematic of the system, with extra mirrors for folding the optical path. KM1 and KM2 - kinematic mounts. KM1 mounts a mirror, KM2 mounts the LCoS-SLM. Conjugated planes are shown by dashed green lines.

For clarity purposes, the following diagrams of the systems will depict

a simplified version not including the folding mirrors. Simplified AOVs schematics is shown in Fig. 2.2

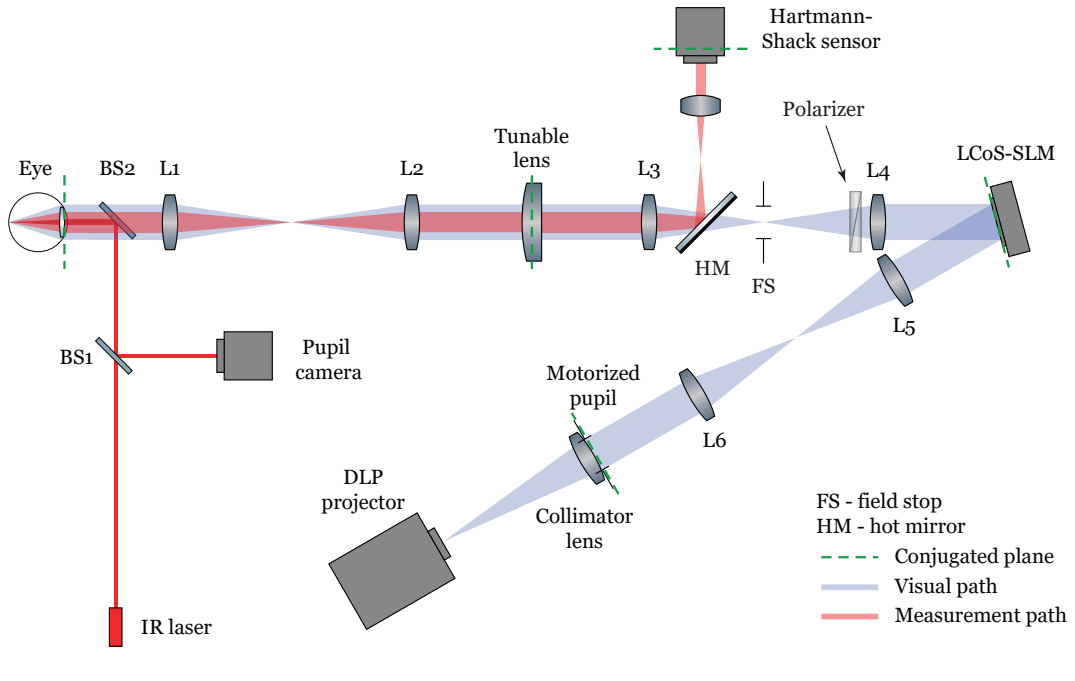


FIGURE 2.2: Simplified schematic of the AOVs, with extra mirrors omitted. Conjugated planes are shown by dashed green lines.

A simplified layout would be used throughout the thesis as it is functionally the same.

2.1.1 Measurement relay

The measurement relay of the system used a Hartmann-Shack wavefront sensor to retrieve the aberrations of a subject. The measurement relay operated in the near infrared (780nm).

A laser diode (shown as IR laser in Fig. 1) (L780P010, Thorlabs Inc, Newton, New Jersey, United States) was used to provide a reference for the HS sensor. The laser diode emitted at 780 nm wavelength with a maximum power of 10 mW. The wavelength was chosen for it provided a good balance between visual comfort to the subject during the measurements, due the poor response of the eye to the NIR (Schnapf, Kraft, and Baylor, 1987),

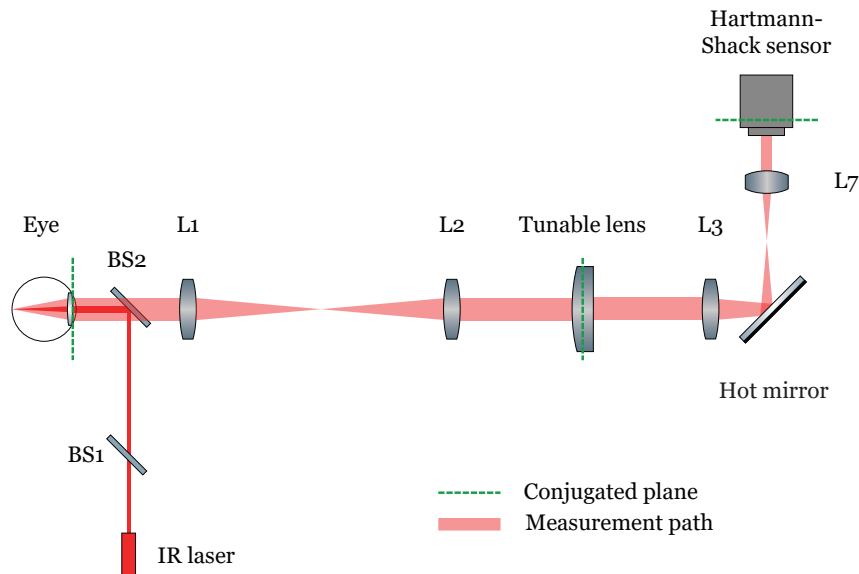


FIGURE 2.3: Measurement relay of the AOVS. Only a part of the wavefront coming from the eye that is transmitted through the BS2 is shown. Wavefront reflecting from BS2 (and consequently BS1) is a part of the pupil monitoring relay.

and the typical CMOS camera sensitivity (Holst and Lomheim, 2007). The IR laser was mounted in the system limited by a circular aperture of diameter 1 mm. To control the power of the laser entering the eye, a neutral density filter was used (NDC-25C-4M, Thorlabs Inc, Newton, New Jersey, United States). With such a configuration the resulting power at the pupil plane was reduced to 20 μW , well below the maximum exposure limit (Delori, Webb, and Sliney, 2007). Before reaching the eye, the beam had also passed through two beamsplitters (BS1 and BS2 in Fig. 2.3), (both models - EBS1, Thorlabs Inc, Newton, New Jersey, United States). The light passed through the BS1, which was used for pupil control, as will be explained further, and reflected from the BS2, to guide the light into the eye. The subject was positioned at the system using 2 lateral translation stages.

With the described configuration, the IR laser produced a near point-like image on the retina. The light coming from that point-like image passed through the ocular media, forming the wavefront containing optical aberrations of the subject's eye. For a perfect eye, the wavefront would be flat. The wavefront is then propagated through BS2.

When the subject was aligned correctly and its pupil was at the focal plane of lens L1 (controlled by the pupil monitoring relay), the wavefront was then optically relayed to the plane of the tunable lens (TL in Fig. 2.3) without any changes by a telescope consisting of lenses L1 and L2 (both achromatic doublets with focal length of 100 mm, AC254-100-A, Thorlabs Inc, Newton, New Jersey, United States).

Power of the tunable lens (Optotune EL-16-40-TC-VIS-20D, Optotune Switzerland AG, Dietikon, Switzerland) changes depending on the applied current, providing a specified dioptric range of -10 D to +10 D.

The tunable lens is used in the measuring relay for manipulation of defocus received by the HS wavefront sensor. The performance validation and calibration procedure of the tunable lens are described in section 2.6. The lens was controlled from a computer using a USB driver (Lens Driver 4, Optotune Switzerland AG, Dietikon, Switzerland).

Another telescope compounded by the lenses L3 ($f' = 100$ mm, AC254-100-A, Thorlabs Inc, Newton, New Jersey, United States) and L7 ($f' = 50$ mm, AC254-50-B, Thorlabs Inc, Newton, New Jersey, United States) was used to conjugate the planes of the subject's pupil and the tunable lens to the plane of microlenslet array of the HS wavefront sensor. The telescope introduced a magnification of -0.5. A hot mirror (DMSP650, Thorlabs Inc, Newton, New Jersey, United States) reflecting the R portion of the light was used to avoid visible light entering to the wavefront sensor. The cutoff wavelength of the hot mirror was 650 nm. The lens L3 and L4 formed a telescope for the visual simulation relay. The software to control the instrument was developed in C++. Because the HS wavefront measurements were done with IR light, some correction must be introduced to estimate the aberrations for the visible portion of the spectrum. A shift in defocus was thus introduced to account for the typical longitudinal chromatic aberration of the eye between 550 nm and 780 nm (Atchison and Smith, 2005; Fernández et al., 2005a).

The optical path of the system was additionally folded by using mirrors (PF10-03-P01, Thorlabs Inc, Newton, New Jersey, United States) in order to minimize the space taken by the system.

2.1.2 Visual simulation relay

The visual simulation relay of the AOVS presented the stimuli to the subjects through a modified version of the wavefront. The manipulation of the wavefront was accomplished by using two separate devices: the LCoS-SLM, and the TL. In a similar manner than for the measuring relay, The TL modified defocus while the LCoS-SLM controlled the rest of aberrations (i.e. astigmatism, high order aberrations, and other diffractive profiles). Figure 2.4 shows the visual simulation relay of the system.

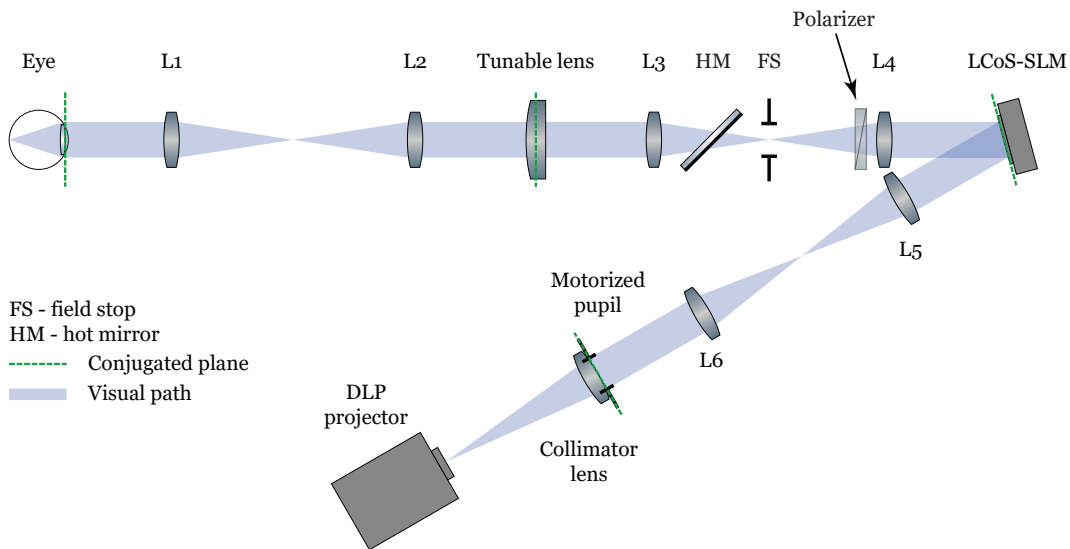


FIGURE 2.4: Visual relay of the AOVS

The visual relay included a high definition digital light processing projector (DLP projector in Fig. 2.4) (DLPDLCR4710EVM-G2, Texas Instruments, Texas, USA). The projector is based on a digital micromirror device (DMD). Detailed information about the DLP projector and its working principle are provided in section 2.7. The DLP projector provided a high resolution (1920 × 1080 pixel) stimulus display.

The projection optics of the DLP was removed to expose the DMD array, which acted as the object for the visual simulation relay. The projector had an HDMI interface that was controlled as a regular additional monitor from the computer. An achromatic doublet (collimator lens) with a focal length of 200 mm (AC254-200-A, AC254-100-A, Thorlabs Inc, Newton, New Jersey,

United States) was used to collimate the light emitted by the DMD array, forming its image at infinity. The angular pixel size in this configuration was 6 arc seconds.

The total magnification of the system was 1, resulting in a maximum theoretical decimal VA value of 10 for the pixel size of the display. While such high VA values are not achievable by a human eye, it was important to allow for small steps between adjacent VA values so that subtle differences can be eventually detected, at least from the instrument point of view.

The entrance pupil of the system was limited by a motorized diaphragm (8MID8.2-0.8-N, Standa Ltd, Vilnius, Lithuania) ranging from 0.8 to 8.2 mm. The diaphragm was placed after the collimator lens, as close as physically possible to reduce propagation of the wavefront. The diaphragm was controlled from the computer. The diameter range covered the physiological pupil of the human eye. A set of neutral density filters ranging from 0.6 to 4 OD was placed in a rotating mount next to the diaphragm in order to control the light flux coming from the DLP projector.

A telescope consisting of lenses L5 and L6 was used to optically relay the plane of the entrance pupil to the plane of the LCoS-SLM. The position of the image of the entrance pupil on the LCoS-SLM was finely calibrated as it will be described in detail in section 3.2.2. The LCoS-SLM exhibited full HD resolution (1920 × 1080 pixels), with a pixel size of 8 μm and a diagonal of 0.7". LCoS-SLM was connected to the computer by using a DVI interface, from where it was controlled as a regular display. The phases on the modulator were encoded by different gray levels from the computer. The plane of the LCoS-SLM was optically conjugated to the plane of the subject's pupil. The LCoS-SLM was used to correct aberrations measured by the HS sensor, or to induce any other phase profile.

A telescope consisting of lenses L4 and L3 was used to optically relay the plane of the LCoS-SLM to the plane of the tunable lens. In the intermediate image plane between the lenses L3 and L4, a rectangular aperture acted as the field stop, also filtering the diffractive effects produced by the pixels of the LCoS-SLM. The field of view was limited to an angular size of 3.1 by 1.7 degrees. The hot mirror allowed the visible light to reach the eye.

2.1.3 Pupil monitoring

The axial position of the subject must be controlled to guarantee that conjugation of the pupil of the eye between planes in the system is properly conserved. The lateral position of the eye is also critical, especially when aberrations are generated by the LCoS-SLM, so that the pupil of the modulator and that at the eye coincide. Small misalignments can distort the results, especially when high order aberrations are considered.

For positioning the eye of the subject, 2 orthogonal translation stages (for axial and horizontal lateral movement) were coupled into the system to support a chinrest or a dental impression of a subject undergoing the testing. Vertical lateral translation was implemented in the used chinrest and in the dental impression mount.

A set of 4 LEDs emitting at 780 nm was placed in front of the exit plane of the visual simulation relay, surrounding the pupil. The LEDs were used to illuminate a subject's pupil to control of the position of the subject. Beam-splitters BS1 and BS2 (as shown in Fig. 2.2) enabled to form the image of a subject's pupil onto an auxiliary camera, which was focused at the exit pupil of the AOVs. The plane corresponded to the focal plane of lens L1.

2.2 System operation

In general, the setup was controlled from a single computer. However, in some experiments where precise psychophysics were required, an extra laptop was employed for providing the stimulus and for the response collection. The software for the AOVS control was written in C++, while various data processing was done using Matlab. Figure 2.5 shows the interface of the control software.

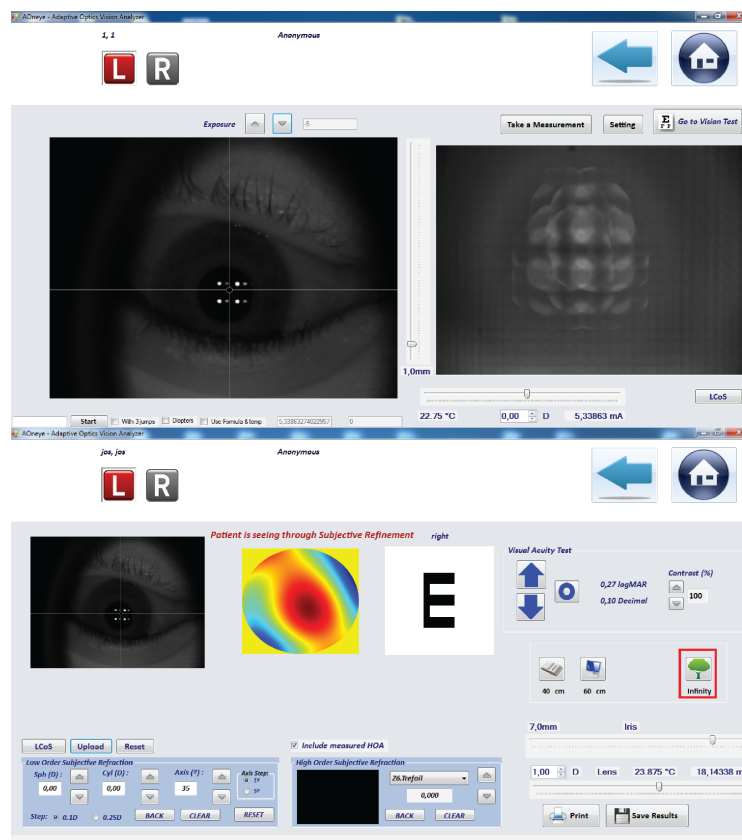


FIGURE 2.5: Interface of the control software of AOVS. Top panel shows pupil alignment/HS measurement procedure, while bottom panel shows visual simulation procedure

The aberrations of the subject were measured using the HS sensor, with the LED array in front of the eye turned off, and the IR laser turned on. As a first step, the tunable lens was in a resting state at 0 D of defocus in order to get an estimation of the refractive error of the subject. Then the lens was

used to compensate for that previously found defocus, and the HS measurement was repeated again. In such case, final results were considerably more accurate, as the HS sensor had to measure a much “flatter” wavefront, due to the removed defocus.

Using HS measurements as the baseline, the visual simulations were done with the objective correction in place. The IR laser was turned off, and the LED array was turned on in order to monitor the position of subject’s pupil. In some cases, subjects were also allowed to do subjective correction of the refraction, directly controlling the lens power using a Bluetooth keyboard.

In this work, visual acuity was determined using Freiburg test (Bach, 1996; Dehnert, Bach, and Heinrich, 2011), based on PEST algorithm. A tumbling E test was used, with four directions. The testing program provided the raw data consisting of: trial number, size of the E letter features, response (1 for correct, 0 for wrong), and the answer time. For the determination of VA threshold, a custom Matlab script was written, fitting the raw data to the Boltzmann sigmoid function, as shown in Eq. 2.1

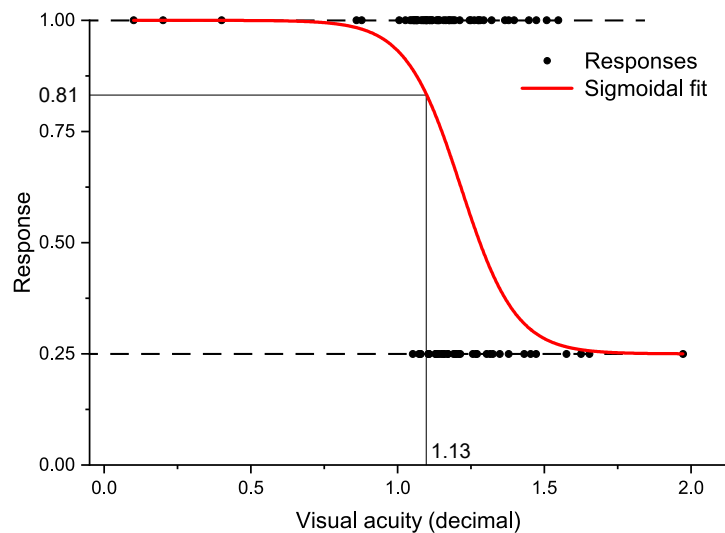


FIGURE 2.6: Determination of VA from the test responses. Wrong answers set at 0.25 to account for statistical error. Threshold for finding the final VA is set at 75% of correct answers, or at 81.25% accounting for guessing possibility.

$$y = A_2 + \frac{A_1 - A_2}{1 + \exp \frac{x-x_0}{dx}} \quad (2.1)$$

where A_1 , A_2 , x_0 , and dx are fitting parameters.

When determining the threshold value from the sigmoid fit, it is important to consider the statistical fluctuations. In the case of 4 orientation of the stimulus, the chance of guessing correctly is 1/4, or 25%. Due to that the bottom asymptote A_1 has to be set at 0.25. Figure 2.6 graphically shows the fitting process and the determination of the final VA value.

For every experiment, participating subjects were informed about the experiment procedure, and gave their informed consent. All presented studies adhered to the Declaration of Helsinki tenets.

2.3 System alignment

The system had to be precisely aligned and calibrated in order to operate correctly and with precision.

The initial optical alignment of the AOVS was done using an auxiliary collimated laser beam as a reference. HeNe laser emitting at 543 nm (HGP005-1, Thorlabs Inc, Newton, New Jersey, United States) was chosen for the reference, as this wavelength was easier to see with a naked eye (Schnapf, Kraft, and Baylor, 1987). The reference laser was spatially filtered with the help of a microscopic objective (10X DIN Semi-Plan, Finite Intl Standard Objective, Edmund Optics, Barrington, New Jersey, USA) focusing the light on to a 50 μm pinhole. The light was then collimated using a 300 mm collimator lens. Near to the collimator lens, a variable iris was introduced as well for controlling the diameter of the reference beam. Figure 2.7 shows the configuration in which the reference laser was coupled into the system.

Two kinematic mounts KM3 and KM4 allowed to direct the laser beam coinciding with the optical axis of the system. The alignment of the lenses within the system was done using a shear plate (SI100, Thorlabs Inc, Newton, New Jersey, United States), which causes interference fringes to appear. As all the lenses aside from the collimator were parts of telescopes, the plane wavefront after passing through each of the lenses had to stay flat. In that case, the interference fringes would appear straight and parallel to the center line on the shear plate. Any tilt or lateral misalignment of the lenses would affect the fringes, making them curved rather than straight. Back reflections from the lenses were also used in order to minimize their tilt in relation to the optical axis. Other components, such as TL, motorized pupil, and LCoS-SLM, which needed to be in the conjugated planes, i.e. at the back focal planes of the lenses within telescopes, were also aligned to keep them at the correct plane and centered relative to the reference beam. To help with the axial alignment, an extra camera with an objective focused at the infinity was used. When looking through lenses L2 and L3 for the tunable lens, L4 and L5 for the LCoS-SLM and L6 for the motorized pupil, these components had to be in focus, as that would mean they were positioned in the focal planes of those lenses, ensuring correct optical conjugation. The same

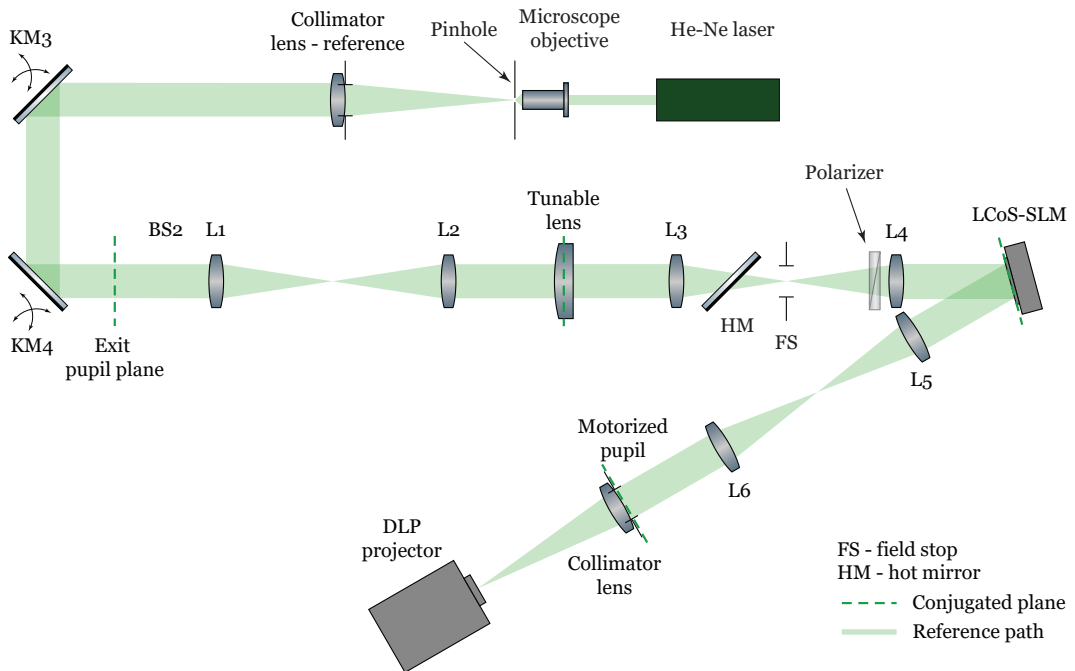


FIGURE 2.7: Setup for calibration of the AOVs. Path of the reference relay is shown in light green color. Exit pupil plane denoted the plane of the AOVs when operating for visual simulation.

method was used with the collimator lens and the HS sensor. When the DMD array was in focus, that meant that wavefront coming out of the collimator lens would be flat, as no defocus was desired in the resting state of the system (i.e., with no modulation from the LCoS-SLM or the tunable lens). HS positioning was crucial as well, as any axial displacement would result in the shift away from the conjugated plane. In such case the aberration of the eye would propagate some distance from the conjugated plane, changing their values. The LCoS-SLM itself was placed on a kinematic mount (shown as KM2 in Fig. 2.1) to help with the optical alignment.

The IR laser used for eye measurements was placed to be parallel to the optical axis, but shifted laterally by a small distance (around 1.5 mm). That would assure that the laser spot would be in the center of the fovea, while the lateral shift would help with avoiding reflections from cornea. For this alignment an artificial eye consisting of a 50 mm lens and a paper with a target on it was placed in the exit pupil of the system. The IR laser was then

adjusted until the desired position was reached.

2.4 Hartmann-Shack wavefront sensor

The HS sensor uses a microlenslet array (APO-Q-P192-F3.17, Flexible Optical B.V., Rijswijk, Netherlands) with a nominal focal length of 3.17 mm (at 633 nm). The microlenses array was mounted in front of a CMOS sensor (DMK 72AUC02, The Imaging Source Europe GmbH, Bremen, Germany). The camera had a resolution of 2592 x 1944 pixels, with a pixel pitch of 2.2 μm . 2x binning was enabled to reduce readout noise and speed up the processing.

Control software for the HS sensor was developed in C++. The program allowed the estimation of the Zernike polynomials describing the wavefront for different pupil sizes.

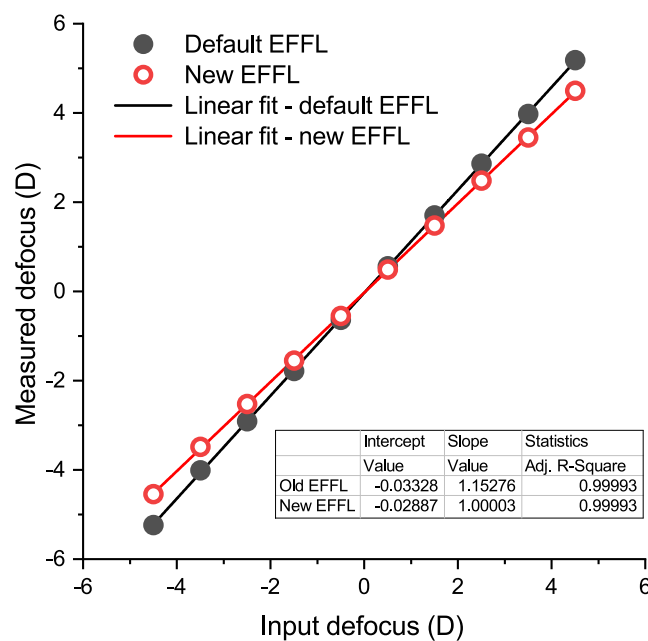


FIGURE 2.8: EFL measurement. Black circles indicate HS measurements with the default EFL, with the black line showing the fitting. Red circles show the HS with the corrected EFL, with red line showing the fitting. Data about the fitting is shown in the table.

The effective focal length (EFL) of the HS sensor had to be calibrated in order for the wavefront to be measured correctly. The effective focal length usually cannot be taken from the technical specifications, as it depends on

the relative position of the camera sensor to the microlens array, which is affected by mechanical tolerances.

Ophthalmic trial lenses ranging from -4 D to 4 D (with a step of 1 D) were used for the EFL calculations. They were introduced in a conjugated pupil plane, as shown in Fig. 2.7. Wavefront was measured using the HS for each of the lens using a manufacturer-specified EFL. The experimentally measured defocus was plotted as a function of the trial lens power. A linear fit was then calculated, as shown in Fig. 2.8 by the red dashed line. A value of the slope different from 1 indicates the mismatch of the EFL with the focal length specified by the manufacturer. The correct EFL value of 2.75 mm was then calculated from the measured slope and the manufacturer focal length of 3.17 mm.

Although the HS measurement was done with IR light, the visual simulation was done in visible light. To take this into account, a chromatic shift in defocus of -0.8 D was introduced. The value was calculated using the longitudinal chromatic aberration of the human eye between IR and visible range (Fernández et al., 2005a).

2.5 LCoS-SLM

The LCoS-SLM contained a layer of parallel-aligned nematic liquid crystal material sandwiched between a silicon wafer with an etched pixel array and a transparent electrode. When voltages are applied to the electrode, they cause the molecules to turn, resulting in a change of the refractive index. The change in the refractive index is transferred to a phase retardation, which can be spatially resolved. It should be noted that, as the liquid crystal is birefringent, so the change occurs only for the component of the light polarized parallel to the direction of the director axis of the fluid. The rest of the components suffer no modulation of the refractive index. Due to this, the polarization state of the incoming light should be accurately set. Accordingly, the thickness of the liquid crystal layer plays an important role in the capability to modulate the phase. The electronic driver for the LCoS-SLM translates the input of gray-level images sent from the computer into voltages to be generated at every pixel. The device had at the the back of the liquid crystal layer a dielectric mirror.

The model used was a PLUTO-VIS-014 (Holoeye Photonics AG, Berlin, Germany), with its photo shown in Fig. 2.9.



FIGURE 2.9: Photo of the LCoS-SLM used in AOVs, Holoeye Pluto. Source: <http://holoeye.com>

The modulator exhibited full HD resolution (1920 x 1080 pixels) on a 0.7" diagonal with a pixel size of 8 μm . Reflectivity was 65%.

The LCoS-SLM allowed to control its internal parameters by a COM port, giving access to calibration settings. These allow to upload a look-up table for the conversion of input gray levels into voltages in order to obtain a precise phase modulation. Figure 2.10 shows the interface of the calibration software of the LCoS-SLM.

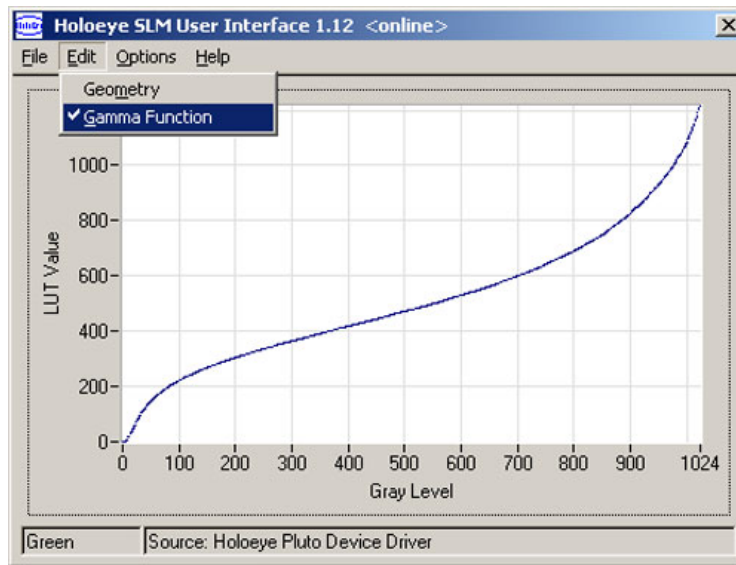


FIGURE 2.10: Interface of the software for controlling the gamma curve of the LCoS-SLM. Source: <http://holoeye.com>

2.5.1 Linearization

A properly calibrated LCoS-SLM is able to provide a reliable and precise phase modulation (Martínez et al., 2014). A number of techniques for calibrating parallel aligned liquid SLMs exist, for example based on interferometry (Bergeron et al., 1995; Reichelt, 2013), transmission of intensity using crossed polarizers (Xun and Cohn, 2004; Reichelt, 2013), and using diffractive gratings (Zhang, 1994; Engström et al., 2013). The manufacturer of the modulator provided a dedicated software for the calibration using a two-beam interference scheme. In such a configuration, two coherent beams are projected onto two halves of the SLM; and then merged together, forming interference fringes. When the gray level in one half of the SLM is altered, the fringes move. From the analysis of the movement, a relationship

between the gray level and phase may be obtained. This method is quite complicated in terms of alignment, as two separate coherent beams are required. Furthermore, optics with high numerical aperture (such as microscopic objectives) are required for merging the two beams. An alternative method was devised (Martínez et al., 2016) which significantly simplified the calibration procedure. Briefly, the method uses the LCoS-SLM itself to separate a single circular beam in two parts, one of which has a varying uniform phase levels (piston), while the other one acts as a reference wavefront with a constant carrier frequency (diffraction grating) in order to produce interference fringes on the camera sensor plane. When the grey level of the piston is changed, interference fringes move laterally. A phase shift is calculated from the movement captured by a camera.

The linearization procedure can be done in the system itself, or in a separate setup. The simplest configuration is shown in Fig. 2.11. The method significantly simplifies the procedure, as only a roughly collimated beam and a regular camera are required.

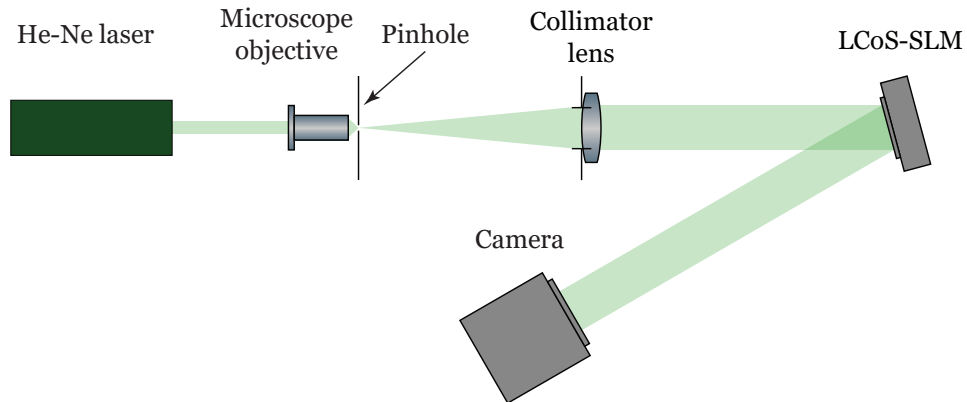


FIGURE 2.11: LCoS-SLM linearization setup.

After the calibration and the subsequent linearization of the device the control exhibits high fidelity and the modulator can be operated in open loop. Figure 2.12 shows the results of the calibration procedure.

Final phase modulation range after the calibration equaled 2.0056π . A least squares linear fit of the phase modulation produced a correlation coefficient above 0.99.

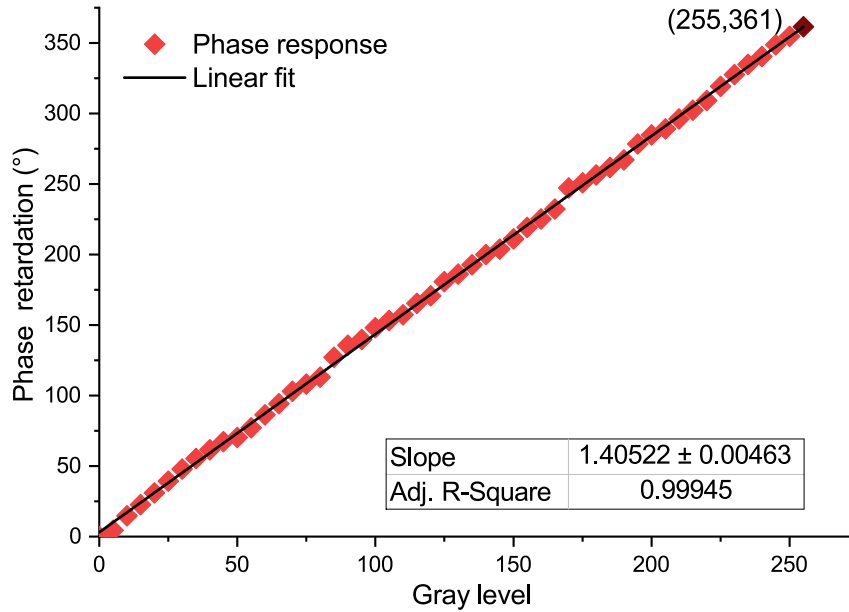


FIGURE 2.12: LCoS-SLM linearization.

2.5.2 Centering

A crucial part of the LCoS-SLM calibration was an adjustment of the digital pupil position so that its center would coincide with the optical axis and the physical pupil image. Any mismatch of the physical and digital pupils would result in some portion of light reflecting from the LCoS-SLM with no modulation. Figure 2.13 graphically shows a case of aligned pupils and a case of misaligned pupils.

To ensure the correct centering a procedure was devised. DLP projector was set to show a white vertical stripe with a width of 100 pixels on a black background. Entrance pupil diameter of 4.5 mm was enforced by the motorized diaphragm, with the digital pupil on the LCoS-SLM of the same diameter. Phase mask inside the digital pupil on the LCoS-SLM was set to modulate 9 D of defocus. If the pupils perfectly coincide then the portion of the non-modulated light would appear only because of the diffractive efficiency of the LCoS-SLM and a usage of polychromatic light (Martínez et al., 2017). However, in case of a misalignment, a larger portion of light would be non-modulated. An auxiliary camera placed in the intermediate image plane between the lenses L1 and L2, as shown in Fig. 2.14, was capturing

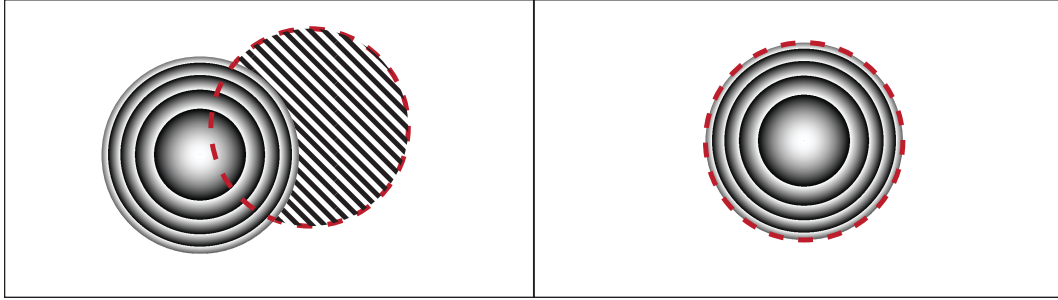


FIGURE 2.13: Graphical representation of centering of a digital pupil on an LCoS-SLM and the eye's pupil. Left panel shows misaligned pupils. In this case, the striped area would allow nonmodulated light to enter the eye. Right panel shows the current situation with aligned pupils. In this case, all the light enters the eye properly modulated.

the images of stimulus passing through the system.

To have a quantitative metric for the estimation of the non-modulated light, the ratio between the central area of the image (shown in Fig. 2.15 in purple), and two peripheral areas (shown in Fig. 2.15 in orange), was calculated. As the peripheral areas only contain the highly defocused part of the image, while the central area contains both defocused and non-modulated parts of the image, the devised metric – ghost metric – allows to characterize the amount of non-modulated light. The perfectly aligned pupils would result in the lowest value. Eq. 2.2 shows the calculation of the ghost metric.

$$GM = \frac{\int_{a-50}^{a+50} I(x)dx}{\int_{a-200}^{a-150} I(x)dx + \int_{a+150}^{a+200} I(x)dx}, \quad (2.2)$$

where GM is the ghost metric, $I(x)dx$ is intensity at a given pixel, and a is a central coordinate for the central pixel of the image of the white stripe.

For finding the center of the physical pupil image on the LCoS-SLM, crucial to match the optical axis, a scanning procedure was devised. First, the pupil center was moved along the horizontal axis, for 400 pixels around the physical center of the LCoS-SLM, with a step of 10 pixels. For each step, the ghost metric was calculated. The lowest value indicated the closest position to the optical axis. The procedure was repeated along the vertical axis. Lowest values from both scans represent the coordinates of the optimal

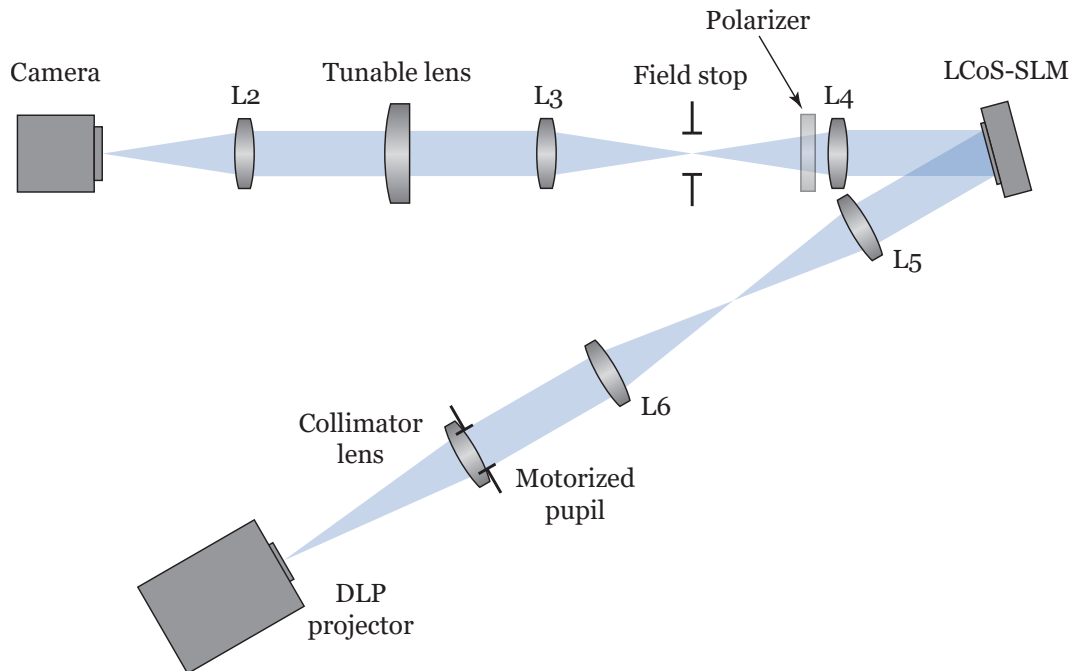


FIGURE 2.14: LCoS-SLM pupil centering setup

digital pupil position. Figure 2.15 shows the ghost metric values along the scanned directions. A second order polynomial was then fitted in order to find the minimum position. For X axis, the center of the pupil was found at 948 pixels, while for Y axis it was at 451 pixels.

2.5.3 Polarization setting

As was explained previously, phase-only modulation occurs when LCoS-SLM receives the incoming light with polarization along the same direction than the director axis of the liquid crystal molecules. For finding the polarization axis in practice, a method similar to the one explained to obtain the center was applied. The polarizer was rotated ± 10 degrees around the theoretical horizontal polarization axis. Figure 2.16 shows the ghost metric calculated from different polarization axis values. The best position was found to be at 91 degrees.

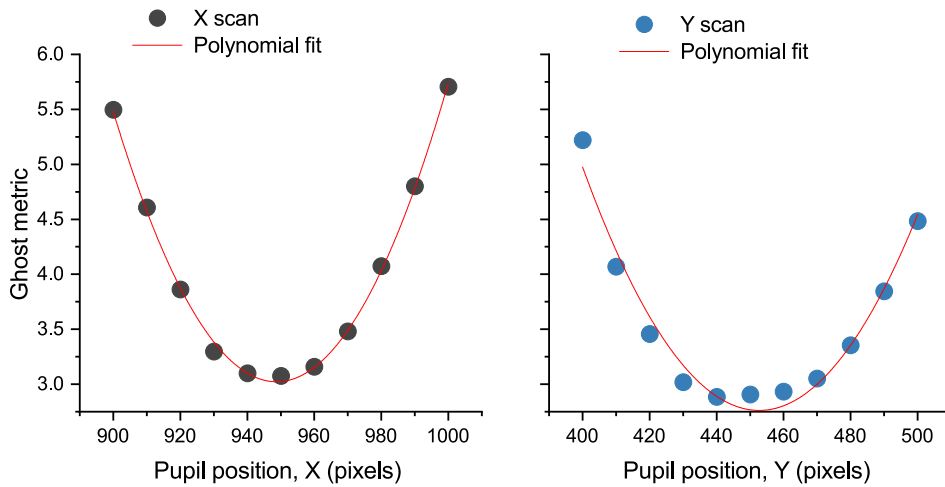


FIGURE 2.15: Ghost metric along the two axes. Left panel shows the scan in the X axis, right - in Y axis. Fitted second order polynomials are shown in both cases with red solid lines.

2.5.4 Phase flicker

The LCoS-SLM is driven by a digital-to-analog converter. Analog signals encoding gray levels from the PC are converted into digital signals corresponding to voltages on the LCoS-SLM itself. This conversion results in temporal fluctuations of the modulated phase - or phase flickering. As a result, the modulated phase might fluctuate around the target value. The fluctuation is related to the binary encoding of the gray level information. The fluctuations are typically in the kHz range, so they cannot be perceived visually. However, they may result in an error in phase modulation. The firmware control of the LCoS-SLM allowed to use different control sequences, which change the quantization of the input signal, affecting the phase flicker. Different sequences were evaluated in order for the AOVS to attain the best possible performance. Figure 2.17 shows the ghost metric values, as previously described, calculated for the different sequences and quantizations, taken as the number of steps that the phase range is distributed for control.

From the results shown in the Fig. 2.17, the 5-5 sequence produced the lowest ghost metric. As a general trend, lower discretization resulted in a

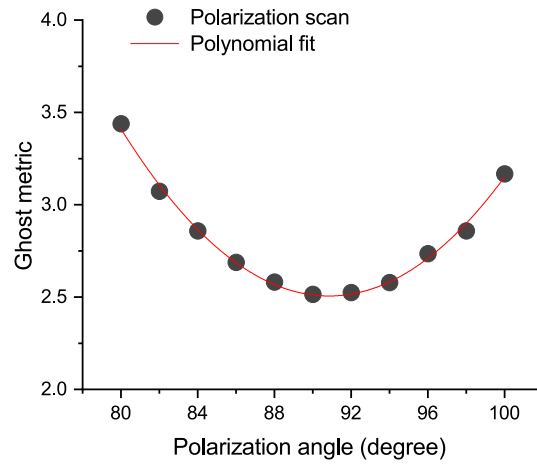


FIGURE 2.16: Ghost metric for varying polarization axis. Red solid line shows the fitted second order polynomial.

better performance. As an exception for 5-5 sequence the lowest discretization level has not shown the best result, although it was similar to it. This may be due to a potential variability. Due to the used quantization, not all 256 gray levels are available for phase modulation, and some are skipped. However due to the very high resolution of the LCoS-SLM, that does not pose a problem for the visual testing purposes.

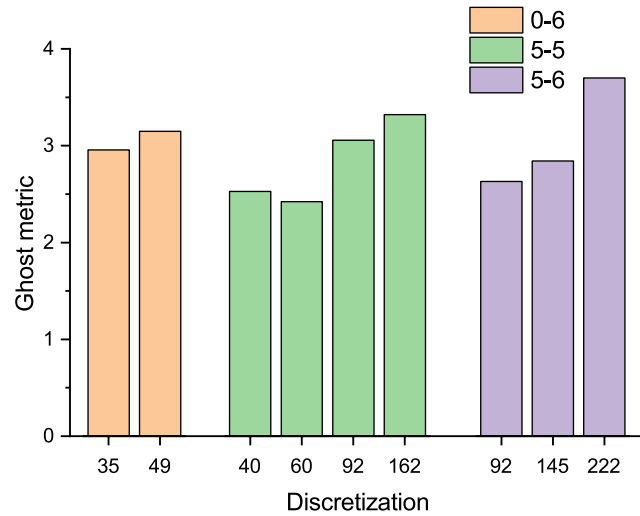


FIGURE 2.17: Comparison of ghost metric for different control sequences and different discretization levels.

2.6 Tunable lens

The operating principle of a tunable lens in general is rather simple. The lens itself consists of optical fluid within a container. One of the optical surfaces of the container is glass, while the other one is an elastic polymer membrane. An electrode (either ring-shaped or a set of stripes) is attached to the elastic surface, either pulling or pushing the edges of the membrane, changing the shape of the lens. Thus, depending on the electrical current applied to the coil of the electrode, the optical power changes. A working principle is shown in Fig. 2.18, with the TL in three different states: plano-concave, plano-parallel and plano-convex.

Multiple tunable lenses were considered for the instrument. The summary of their key characteristics is shown in Table 2.1.

Varioptic Visayan allowed correcting astigmatism. However, it was discovered during the calibration stage that the lens exhibited high temporal instability preventing accurate control. The base power of the lens would shift by up to 1 D with the same calibration state. Moreover, the lens had a very high Abbe number, which would result in a significant amount of induced LCA. This extra LCA would not be able to be corrected, as it would change with induced defocus.

TABLE 2.1: Summary of tunable lenses considered for the AOVS. Abbe number for Varioptic Visayan is unknown.

Tunable lens	Dioptric range, D	Clear aperture, mm	Abbe number	Modulation
Optotune EL-10-30	10 – 33	10	36	Defocus
Optotune EL-16-40-20D	-12 – 10	16	108	Defocus
Varioptic Visayan	-10 – 10	8	—	Defocus & Astigmatism

Optotune EL-10-30 only had a positive dioptric range, so it would have to be offset by a negative lens to produce a desired range. At the moment of system design, that lens was also unavailable with a temperature sensor, which would result in a temporal instability, as the lens would heat up during operation.

Optotune EL-16-40-20D was chosen for the AOVS. It has a bigger clear aperture of 16 mm, easily covering the whole physiological pupil range. It also exhibits a high Abbe number of 108, being almost achromatic for visual testing purposes. Finally, it also employs a temperature sensor, allowing for a better temporal stability. Figure 2.18 shows a schematic of Optotune EL-16-40-20D.

The defocus response of the TL as a function of the input current is not linear. Due to that, developing a look-up table was useful for controlling the device. The tunable lens was calibrated within the AOVS instrument itself. Compared with the normal state of the instrument, the hot mirror was exchanged for a silver-plated mirror, as the Hartmann-Shack sensor had to work with the visible light instead of the near IR. Reference image for the HS sensor was taken through the system with the tunable lens taken off. A reference beam from a HeNe laser emitting at 543 nm was employed.

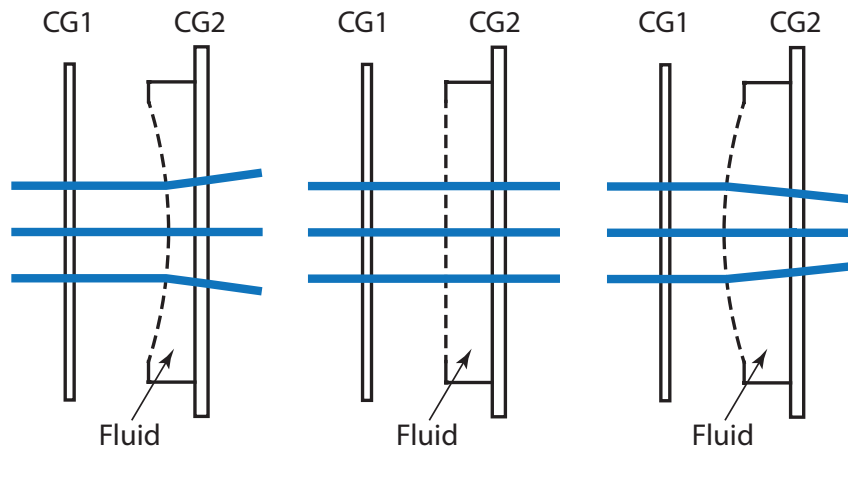


FIGURE 2.18: Schematic of Optotune EL-16-40-20D. CG1 and CG2 - cover glasses. Dashed line shows the elastic membrane surface.

2.6.1 Hysteresis and lens control

The Hartmann-Shack sensor was used for measuring the defocus generated by the lens. A set of electrical currents within the range of -200 mA to 200 mA was sent to the TL, with the HS sensor retrieving the corresponding defocus. Initial measurements indicated that the TL suffered from hysteresis: the output optical power depended on the previous power state. This behavior is graphically shown in Fig. 2.19.

Four different sequences are presented in the Fig. 2.19: ssequence 1 corresponds to input current being changed from -180 to 180 mA in steps of 20 mA; sequence 2 is the same as 1 but in opposite direction; sequence 3 corresponds to input current being reset to -180 mA before the target value; sequence 4 is the same as 3 but with the reset current value of 180 mA. The maximum defocus difference between sequences for the same current value reached 1.2 D at -140 mA. Considering the the depth-of-focus of the eye (Atchison, Charman, and Woods, 1997), the uncertainty was unacceptable for visual applications.

To alleviate the effects of the hysteresis, an alternate protocol to control defocus was devised. A set of 1000 random current values was sequentially programmed on to the lens within the AOVs. Defocus values achieved by

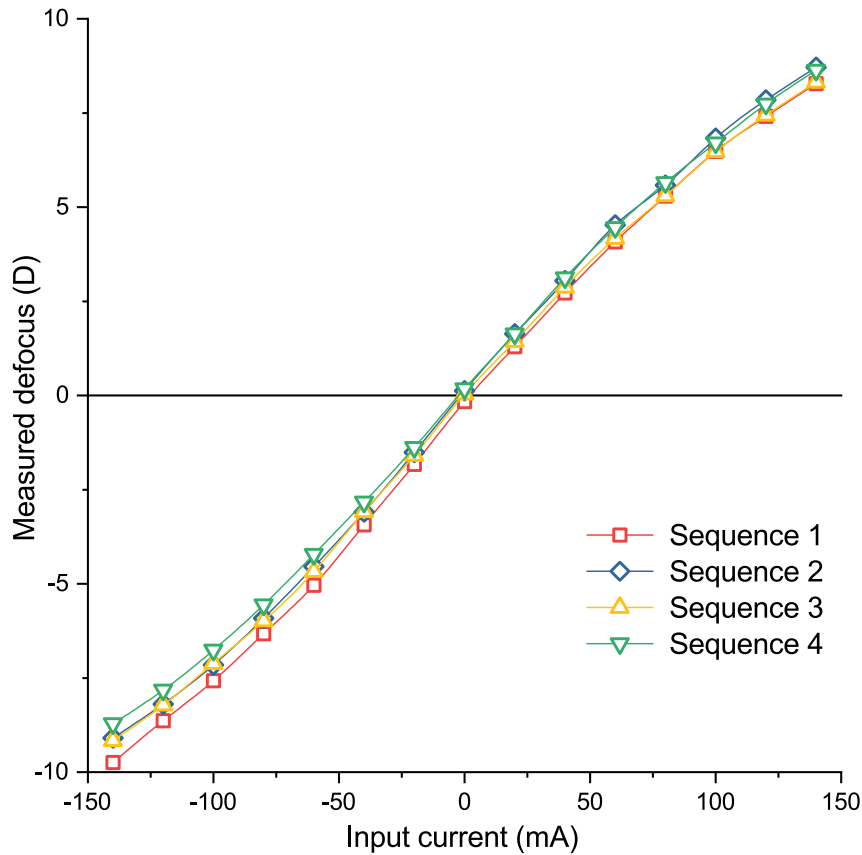


FIGURE 2.19: Hysteresis exhibited by the tunable lens. Description of the sequences can be found in the text.

each of the input currents were measured by the HS sensor. A 5th order polynomial was fit to the defocus values as a function of input current, which then served as a control function for the tunable lens. Figure 2.20 shows the measured defocus values as well as the fit. Eq. 2.3 shows the equation describing the fitted function.

$$y(x) = 9.72 \cdot 10^{-12}x^5 + 4.17 \cdot 10^{-10}x^4 - 9.29 \cdot 10^{-7}x^3 - 2.28 \cdot 10^{-5}x^2 + 0.07x + 8.08 \cdot 10^{-4}, \quad (2.3)$$

where y is resulting defocus in D , x is input current in mA.

In order to reproduce the same behaviour in practice, the lens was programmed to operate without a continuous change in defocus, but rather

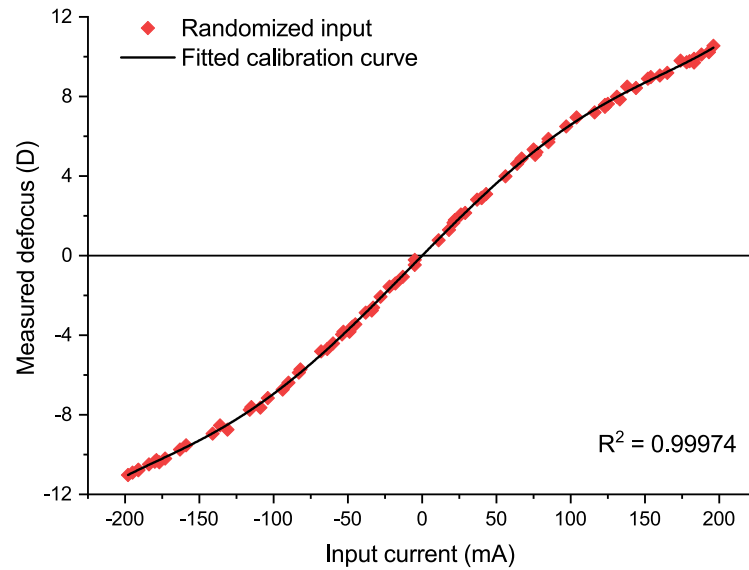


FIGURE 2.20: Final tunable lens control function. For clarity, only 100 values are shown. Polynomial of 5th order fit to the experimental values is shown as a red line.

using discrete changes from one value to another. Using this control function resulted in the lens having an operational range of -12 D to 10 D, which was more than the value specified by the manufacturer. After the calibration tunable lens showed a defocus uncertainty (described by standard deviation) of 0.11 D, which is well within the usual depth of focus of the eye (Marcos, Moreno, and Navarro, 1999). Figure 2.21 shows the response of the tunable lens after calibration.

It is important to note that due to the principle of operation of the TL, the position of principal planes also vary as a function of defocus. The maximum shift in the front principal plane position of 4 mm occurred when the lens transitioned from a plano-concave to a plano-convex shape. Fig. 2.22 shows the principal planes shift, as calculated using ray-tracing software (Zemax, Zemax LCC, Washington, USA).

Ordinarily, that would pose a problem, as the AOVS depends on accurate conjugation of the planes, as otherwise aberrated wavefront would propagate, changing all aberrations and most importantly, defocus. However, using current method of calibration this is taken into an account, as the HS measures the wavefront in a conjugated plane, and not in the back

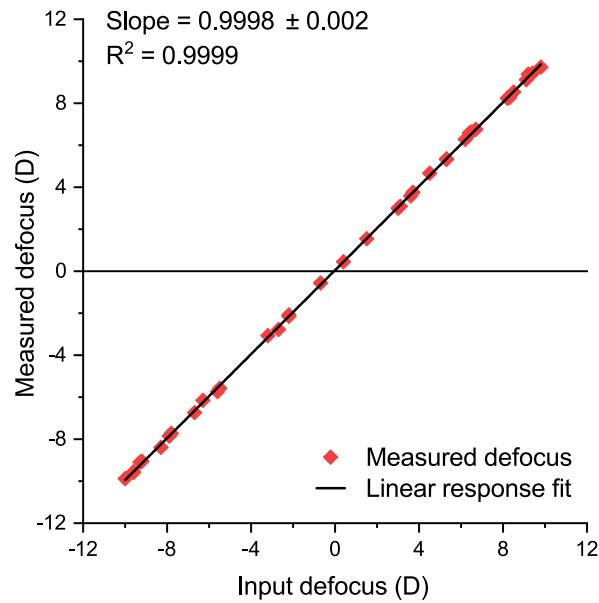


FIGURE 2.21: Tunable lens response after the calibration. Black line shows a fitted linear function. Slope of the fitted function together with quality of the fit are shown in the top left corner.

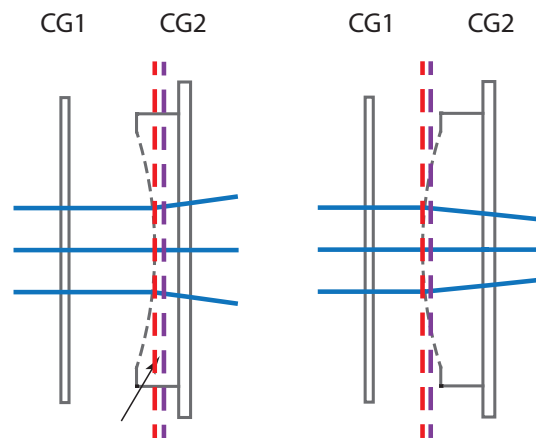


FIGURE 2.22: Shift of principal planes in the Optotune lens. Red line denotes the front principal plane, while purple - the back principle plane. Note the shift of both planes relative to the cover glasses (GS1 and GS2). Angles of refraction and distances are exaggerated for visual purposes.

principal plane of the lens. Thus the wavefront propagation issues are accounted for automatically.

2.6.2 Temperature control

The stability of the TL with changing temperature was studied. When tunable lens is producing defocus, current is applied, and, naturally, its temperature rises. Due to changing temperature, refractive index of the fluid contained within the lens changes, affecting the modulated defocus. As the tunable lens chosen for the AOVS had a temperature sensor, it was possible to implement temperature control for keeping induced defocus values temporally stable.

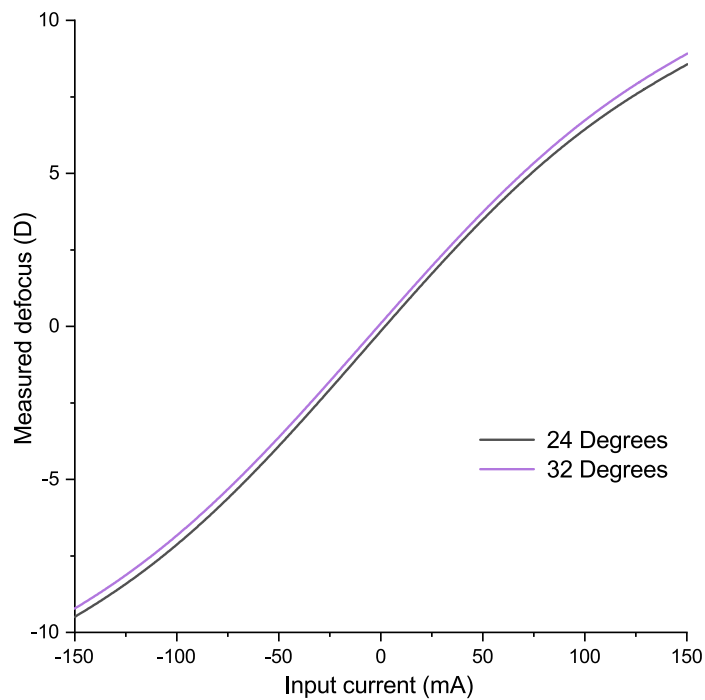


FIGURE 2.23: Temperature testing of Optotune lens. Only defocus response curves for 24 and 32 degrees are shown for clarity.

Calibration curves were retrieved for different temperatures. As a first step, a set of 200 measurements was taken with the lens at a room temperature of 24 degrees Centigrade. When the lens temperature reached 26 degrees, another set of 200 measurements was taken. Same procedure was

repeated for 28, 30 and 32 degrees Centigrade. During each set of measurements, lens temperature stayed within ± 0.5 degrees of starting temperature. The results are shown in Fig. 2.23.

After fitting 5th order polynomials to the three curves, it was found that the difference between them was essentially constant, especially considering the uncertainty of the operation of the lens. That showed the temperature effect to be linear, contributing to 0.033 D of shift for each degree Centigrade.

2.6.3 Optical quality

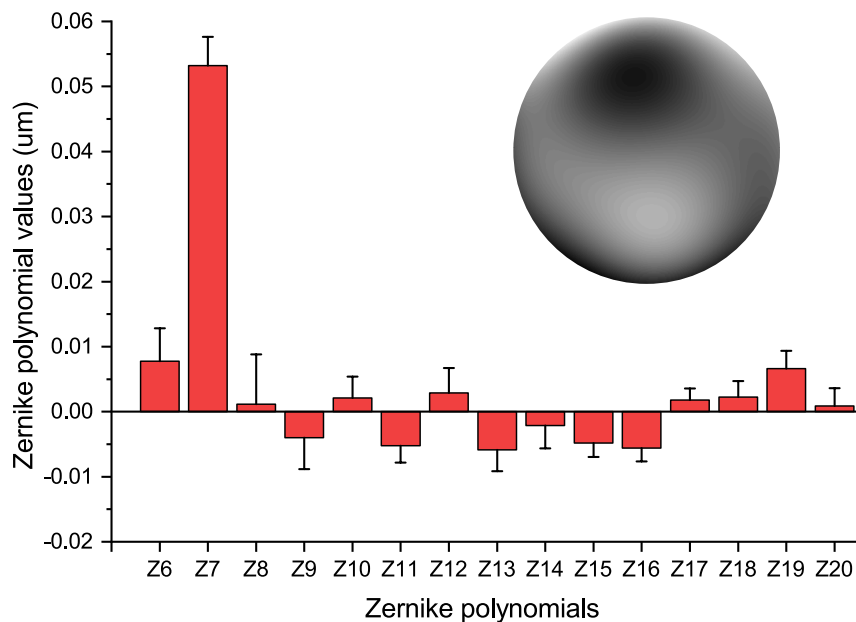


FIGURE 2.24: Zernike polynomials (shown in μm) representing high order aberrations produced by the tunable lens. Values are averaged from 1000 measurements for different defocus values. Average wavefront reconstructed from the average values is given in the top right corner of the figure. Pupil diameter was set at 4.5 mm, error bars show standard deviation.

Optical quality of the lens was also evaluated within the AOVS, using a reference beam and the HS sensor. 1000 random defocus values were programmed on the lens within the operational range, recording the associate wavefront for each condition. Pupil diameter was set to 4.5 mm. Average

results for high order aberrations are shown in Fig. 2.24. The aberrations were measured across the whole operational range.

The most prominent aberration in amplitude was the vertical coma aberration, which appeared as a consequence of vertical operation of the TL. The gravitational force affects the elastic membrane containing the fluid, causing a vertically oriented asymmetry. The amplitude of other high order aberrations were irrelevant for visual applications (Applegate et al., 2003).

2.6.4 Predictability of the response among distinct TL units

Multiple units of the TL Optotune EL-16-40 were also tested to evaluate whether it is possible to use the same control function, or individual calibration is required. Figure 2.25 shows the obtained calibration curves applying the method explained before in this section. The same driver was used for all lenses, keeping the same experimental conditions and hardware among the runs.

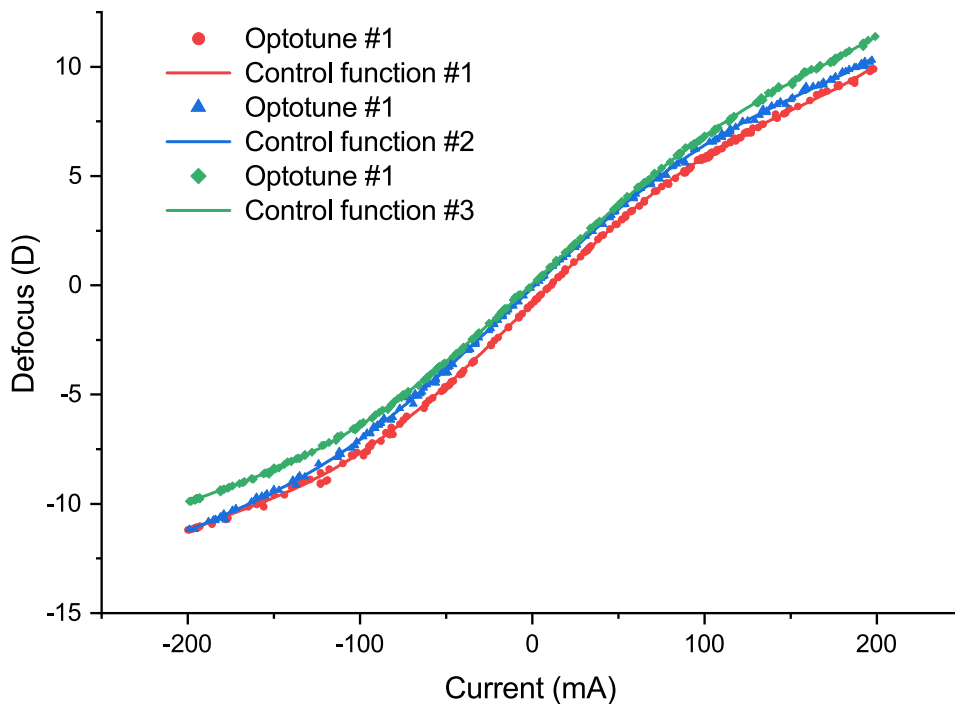


FIGURE 2.25: Calibration defocus curves for three different units of the TL.

Results showed that each lens behaves very differently, as shape of the control curve and even the defocus values at 0 mA were different. Due to this, each lens has to be calibrated separately and have its own control function.

2.7 Stimulus projector

A projector based on digital micromirror technology (DMD) was chosen for stimulus presentation. The illumination is accomplished by light-emitting diodes (LED), generating a high luminous flux comparatively to the OLED display technology. As the AOVS was intended for a very accurate vision evaluation, a DMD with the highest resolution on the market (at the moment of system design) was chosen. The DMD array had a resolution of 1920×1080 micromirrors, with a pixel size of $5.4 \mu\text{m}$, resulting in a diagonal of $0.47''$. A commercial module from Texas Instruments (Texas, USA) was acquired.



FIGURE 2.26: Stimulus projector - DLP4710EVM. For using in the AOVS, the projector lens was taken off, exposing internal DMD array. Source: ti.com

The DMD contained an array of aluminum micromirrors, which presented two different positions: “on” and “off”. The working principle is graphically shown in Fig. 2.27.

“On” position of a micromirror reflects the light onto a $+17$ degree angle, sending the light into the optical path, resulting in a white pixel. The “off” position deflects the light out of the optical system, resulting in a black pixel. Due to the high speed of the micromirror array, any intermediate grey

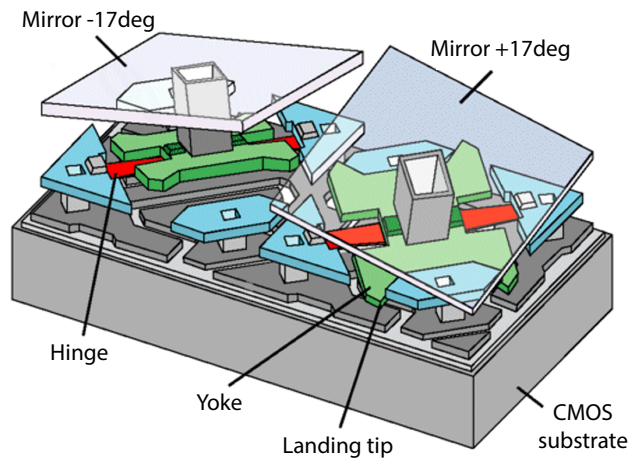


FIGURE 2.27: Working principle of a digital micromirror device. Further description is given in the text. Figure adapted from Travinsky et al., 2017.

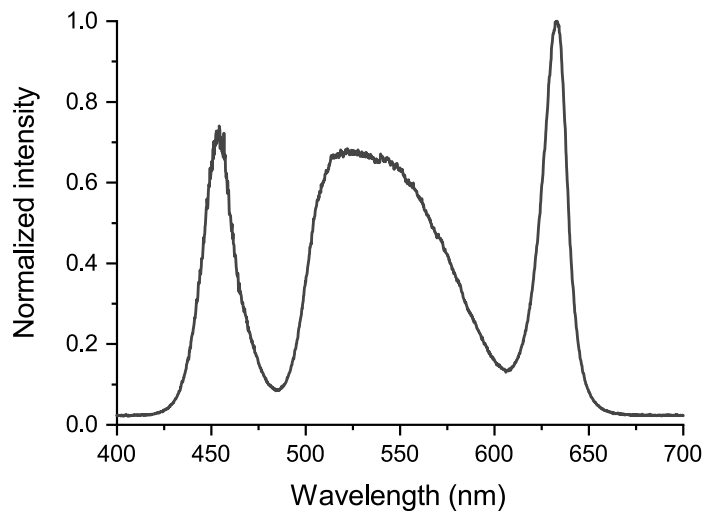


FIGURE 2.28: Normalized spectrum of the DLP with input currents set at 1 A.

levels are possible by using temporal multiplexing, i.e. switching between “on” and “off” states at a given frequency. A color image is generated multiplexing different sources.

Micromirrors were illuminated with three different light emitting diodes (LEDs), corresponding to the red, green and blue channels, providing a

maximum luminous flux of 600 lm. The refresh frequency for a color image was 30 Hz. Current of individual LED channels was adjustable from 1 to 12 A (up to 16 A for blue LED), giving the possibility to manipulate both the luminous flux and the spectral shape of the emitted light.. The spectrum of the DLP with all of LED currents set at 1A is presented in Fig. 2.28.

3 Experiments

This chapter presents the experiments performed in the scope of this thesis. All of the experiments were done using the developed AOVS.

First section describes the proof-of-concept measurements of high myopes to showcase the capabilities of the developed instrument. Aberrations of seven highly myopic subjects were measured and compensated, then the visual performance was evaluated. For three subjects high-order aberrations were corrected as well, and visual acuity was compared with a case of low-order aberrations correction.

Second section describes the manipulation of the longitudinal chromatic aberration with the developed AOVS and its effect on vision. Visual acuity was measured through-focus for four healthy adults in three different chromatic conditions. To complement the experimental results, a thorough ray-tracing modeling of the eye coupled with the studied chromatic conditions was performed. VA was then predicted from the optical quality, and compared with the experimental values.

Third section the visual adaptation to corrected longitudinal chromatic aberration in different contrast levels with five subjects participating in the experiment. VA was measured continuously along the course of 20 minutes in both natural and compensated LCA conditions. The adaptation process was then quantified using Boltzmann sigmoid fits.

3.1 Measurements of high myopes

Most of the AOVS have a significant shortcoming - the limited range of the refraction that they can operate with. The instrument developed here enhanced this capability through the incorporation of the TL, discharging the LCoS-SLM for the correction of this term. Some high myopes were selected for this experiment to demonstrate the capability of the instrument to operate in subjects with large refraction.

Measurements consisted of two stages - aberrometry and visual simulation, with a total time of around 30 minutes. In order to ensure the correct operation of the AOVS, subjects were accurately aligned at the system by using a chin rest.

Cycloplegics were not instilled, resulting in natural pupil diameters. However, for the purposes of HS measurements as well as the visual simulation, pupils were limited to 4.5 mm. Pupil at the HS sensor was limited by the software, while for visual simulation the entrance pupil was imposed by the motorized pupil.

3.1.1 Subjects

Seven young adults with a mean age of 23.5 years ($SD = 2$, range - 21 to 27 years old) participated in the experiment. Subjects were selected amongst optometry students with myopia refraction above -5 D. The subjects were fixed at the system by using a chin rest. Their pupils were monitored with the auxiliary camera to assure correct axial and lateral alignment to the system. No cycloplegics were instilled, and the pupil was limited to 4.5 mm of diameter by the motorized diaphragm for visual testing purposes. Aberrations were retrieved at the maximum physiological pupil by the HS, and subsequently limited digitally for matching the other physical pupil. Measurements were performed monocularly. The subjects declared their manifest refraction obtained within the past two years by a professional optometrist. The values of such refraction are presented in the Table 3.1.

3.1.2 Aberrometry

The experimental procedure started with the estimation of the subject's refraction through the AOVS. Provided that the reported manifest refraction was obtained by using ophthalmic lenses, appropriate correction was done to compare these values with those obtained in the AOVS, where the pupil plane is taken as reference. The used formula is shown in Eq. 3.1 An average distance ophthalmic lens-eye of 12.5 mm was taken for the calculation.

$$D_p = \frac{D_l}{1 + d \cdot D_l'} \quad (3.1)$$

where D_p is defocus in the pupil plane, D_l is defocus in the ophthalmic lens plane, and d is the distance between the planes.

The equivalent sphere was obtained from the wavefront measurements retrieved by the HS sensor. Zernike polynomials up to 6th order were fitted to the wavefront. A second refinement for the measurement of the wavefront was performed by repeating the procedure, this time incorporating the correction of the equivalent sphere in the TL. This procedure allowed to reduce the displacement of the spots, due to the defocus being mostly eliminated from the second measurement. Consequently, linear and precise operation of the HS is guaranteed. (Primot, 2003). With the pre-compensation of defocus, full correction of defocus and astigmatism was introduced. The subjects found their best subjective refraction around this starting condition using the visual simulation relay. For this purpose, a Maltese cross subtending 1 degree was presented.

Direct control of the defocus modulated by the tunable lens was given to the subject, using an auxiliary keyboard. For each subject, the final defocus value including the subjective refinement did not differ from the objective measurement by the HS sensor by more than 0.2 D, which is within the physiological depth of focus of the human eye for the pupil of 4.5 mm (Campbell, 1957; Atchison, Charman, and Woods, 1997; Marcos, Moreno, and Navarro, 1999). Table 3.1 shows the comparison between the manifest refraction, provided by the subjects in the beginning of the experiment, to the experimental values obtained by using the AOVS.

Aside from the refraction value, high order aberrations represented by

TABLE 3.1: Comparison between refraction achieved with trial lenses and using AOVS.

Subject	Trial lenses		AOVS	
	Sphere, D	Cylinder, D	Sphere, D	Cylinder, D
S1	-10	—	-10.6	—
S2	-4.2	-4.65 x 175°	-5.2	-4 x 175°
S3	-9	—	-8.8	-1.5 x 170°
S4	-7.5	—	-7.1	-2.2 x 175°
S5	-7	-0.5 x 30°	-7.6	-0.6 x 0°
S6	-7	—	-7	-0.5 x 30°
S7	-5.5	—	-5.5	-0.6 x 45°

the Zernike polynomials of 3rd to 6th order were also analyzed. Three wavefront measurements were taken, and the mean Zernike polynomials were calculated. Figure 3.1 shows the averaged values of high-order Zernike polynomials for all subjects.

Zernike polynomials were within the range of normal or emmetropic population (Francisco Castejón-Mochón et al., 2002; Thibos et al., 2002; Marsack, Thibos, and Applegate, 2004; Charman, 2005; Salmon and Pol, 2006). The spherical aberration exhibited the largest amplitude, yet small in absolute value as expected in the young eye. Figure 3.2 shows a comparison of the RMS wavefront errors obtained from a normal population (Salmon and Pol, 2006) with the results from high myopes.

Figure 3.2 shows a good agreement between normal and highly myopic populations. Some studies show the high order aberrations increasing for highly myopic eyes compared to the emmetropic ones.

3.1.3 Visual quality with AO correction

VA was initially obtained with the correction prescribed by the AOVS, and then confronted with the one obtained when applying the manifest refraction for every subject. DLP projector was set to produce a luminance of

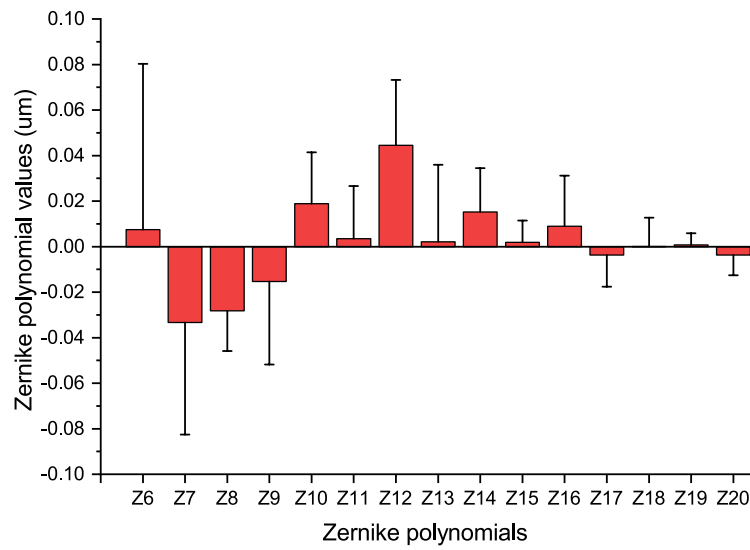


FIGURE 3.1: Zernike polynomials of participating subjects. Error bars show standard deviation.

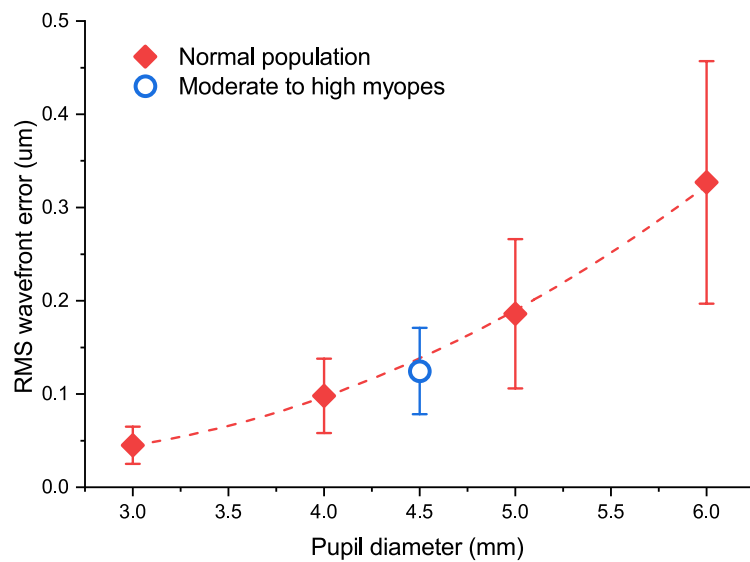


FIGURE 3.2: Comparison of RMS wavefront errors of normal population to the ones of high myopes participating in the experiment. Standard deviation is shown by the error bars. Data for normal population (filled rhombus) is taken from Salmon and Pol, 2006.

60 cd/m^2 at the pupil plane. A black tumbling E letter was shown at four orientations on a white background, with 100% contrast.

VA was obtained following the procedure disclosed at section 2.2. The VA was measured using the Freiburg test (Bach, 1996; Dehnert, Bach, and Heinrich, 2011). 3 repetitions of 90 trials was done under each visual condition. Subjects indicated the perceived direction of the letter using a dedicated keyboard. Their responses were recorded as a raw data consisted of the answer (1 for the right answer, 0 for the wrong), along with the angular size of a single line of the letter. Custom software written in Matlab (Mathworks, Natick, MA, USA) was then used to analyze the data. A Boltzmann sigmoid function, with an asymptote set at 0.25 (representing a statistical possibility of guessing a correct orientation of the E letter from 4 different choices) was fitted to the data. VA was the found at the threshold value of 75% of correct answers. The slope of the sigmoid function was set to be a free parameter in the fitting.

The VA obtained in the experiment are shown in Fig. 3.3. Prescribed Rx indicates cases when manifest refraction values were corrected.

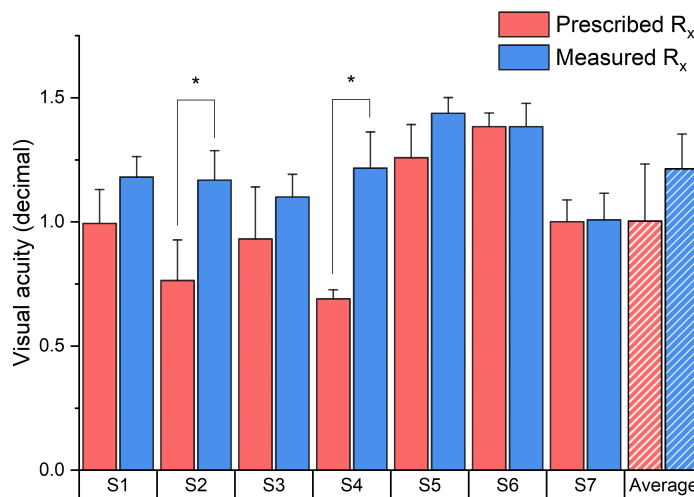


FIGURE 3.3: Visual acuities exhibited by the subjects. Error bars indicate standard deviation. Asterisks show the statistically significant cases ($p < 0.05$).

For three subjects (S5, S6 and S7) the impact of compensation of the

HOA on VA was obtained. For the case of HOA correction the fixation and alignment of the pupil is critical. Due to this, position of the subjects was fixed to the system by their dental impression. After removing equivalent sphere with the TL, a second run permitted to estimate and correct the rest of aberrations by the LCoS-SLM up to 6th order. Figure 3.4 shows the wavefronts and associated PSFs of the three subjects after removing defocus and astigmatism-related Zernike polynomials. Wavefronts are 2π wrapped at 550 nm. The Strehl ratio is also shown.

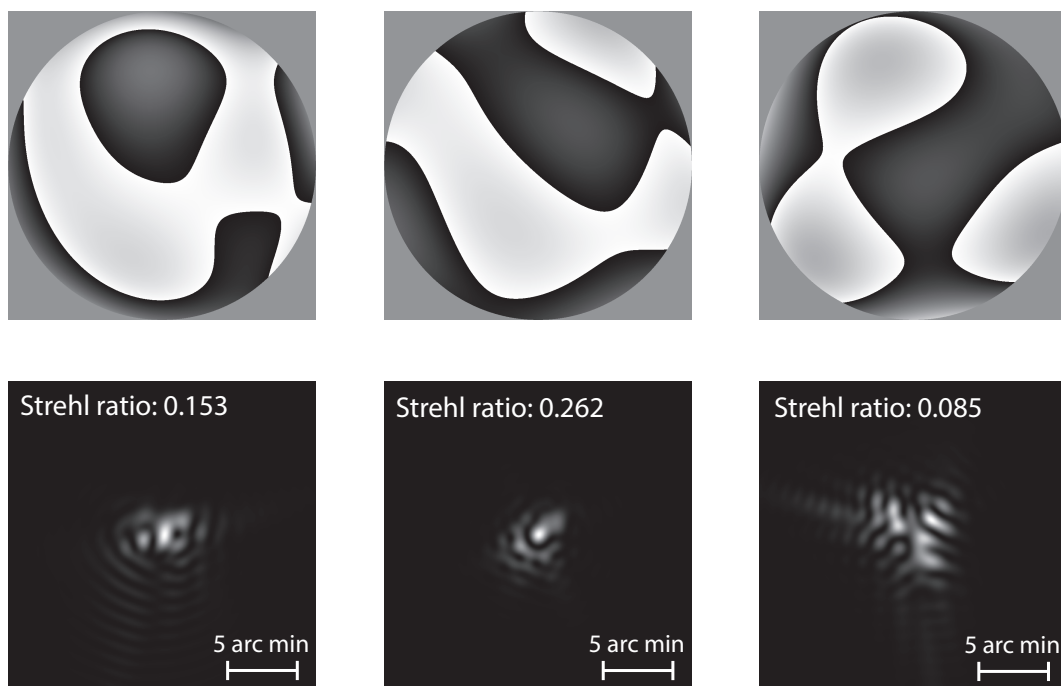


FIGURE 3.4: Optical quality of subjects S5, S6 and S7 (by columns, left to right). Only high order aberrations are shown. Top row: 2π -wrapped wavefronts. Bottom row: associated PSFs. Strehl ratios are also shown in the top left corner of the lower panels.

Amplitude of HOA in these three subjects were similar to the values found in emmetropes (Salmon and Pol, 2006). Strehl ratios provided a useful qualitative metric of optical quality, showing a high inter-subject variability.

The VA with HOA correction are shown in Fig. 3.5. In all cases, the mean VA was higher for full wavefront correction (i.e., including HOA).

Even though subjects S5 and S6 showed relatively high VA values for low-order aberration correction, there was still a benefit when HOA correction was enabled. It is interesting to note that subject S7, who presented the lowest refraction of -5.5 D (vs -7 D of subjects S5 and S6), but higher HOA amplitude, attained the poorest VA, both for low-order and full wavefront corrections.

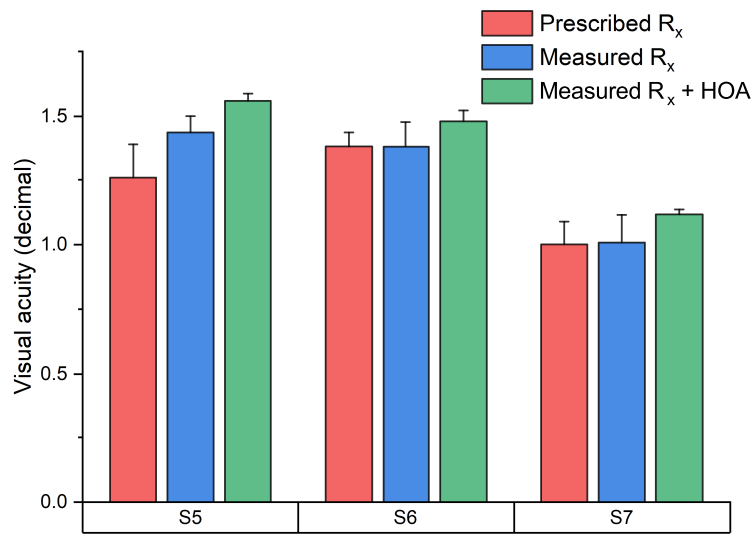


FIGURE 3.5: VA values achieved by subjects S5, S6 and S7 compared for low-order-only wavefront correction and a full wavefront correction (Zernike polynomials of up to 6th order). Standard deviation is indicated by error bars.

3.1.4 Discussion

The estimation of refraction for high myopes were very accurate in all cases. The subjective refinement of the sphere and astigmatism barely changed the values estimated from wavefront measurements, with changes in defocus below 0.2 D, which can be considered within the depth of field for the 4.5 mm pupil (Marcos, Moreno, and Navarro, 1999). Accurate HOA estimation (Primot, 2003) was achieved because of the pre-compensation of equivalent sphere accomplished by the TL. The amplitude of the HOA were comparable to that found in the emmetropic eyes (Cheng et al., 2003; Salmon and Pol, 2006; Rossi et al., 2007). Some previous studies have reported contradictory

results, in the direction of higher HOA in the myopic eye as compared to the normal eye (He et al., 2002; Paquin, Hamam, and Simonet, 2002). Other studies nevertheless have not found any correlation between HOA and defocus (Collins, Wildsoet, and Atchison, 1995; Carkeet et al., 2002; Charman, 2005). The question still remains open for future studies. Because of the limited number of subjects participating in the study, no general conclusions can be made. Possibly, the results might change when other pupil size is considered. On the other hand, the HS measurements presented here were more accurate than those in earlier studies (Collins, Wildsoet, and Atchison, 1995; Carkeet et al., 2002; He et al., 2002; Paquin, Hamam, and Simonet, 2002) as the linear operation of the sensor was assured (Primot, 2003).

Separating the task of wavefront modulation between the LCoS-SLM and the TL was especially advantageous for the AOVS operation with high myopes. As the LCoS-SLM was free of correcting defocus (which is usually the dominant aberration in the human eye), the negative diffractive effects associated to phase wrapping were reduced (Fernández, Prieto, and Artal, 2009a). A higher amplitude of modulated aberrations results in more phase wrapping, which reduces contrast of the image because of the parasitic diffractive orders. Phase wrapping also causes chromatic effects, which may be undesirable (Martínez et al., 2017).

In contrast to the LCoS-SLM, the TL, being before the HS in the optical path, also allowed for a true closed-loop real time operation for defocus. Meanwhile, closed-loop is usually not possible for the LCoS-SLM, as it operates in a certain spectrum range, around the calibration wavelength. Visual testing is typically done in visible light, while measurements are done in the IR (in order to not disturb the subject with very bright visible light), resulting in the wavelength mismatch.

The defocus range of the TL is -12 to +10 D, which should be enough for most high myopes (Holden et al., 2016). However, in case a higher defocus range is needed, it can be shifted in a myopic direction by simply changing the object's distance to the collimating lens. As the hyperopic eyes above 5 D are rarely found (Vitale et al., 2008), the TL range can be shifted by 5 D, resulting in a -17 to +5 D range.

The subjects participating in the study achieved normal VA values during the experiment, once their defocus and astigmatism were corrected.

Some studies have previously demonstrated that high myopes had lower visual performance due to the retinal stretching (Collins and Carney, 1990; Strang, Winn, and Bradley, 1998; Bradley, Switkes, and Valois, 1988; Chui et al., 2005), which resulted in an insufficient retinal photoreceptor sampling. A different work argued that the insufficient sampling might be compensated by the positive magnification of the retinal images, as the eye itself is enlarged. The previously reported reduced visual performance of high myopes can be attributed to the employed correction method. Correcting lenses can introduce a minification effect, thus naturally lowering the achievable VA. Contact lenses can even introduce additional aberrations, worsening the optical quality (Collins and Carney, 1990; Strang, Winn, and Bradley, 1998). AOVS eliminates those problems, as the aberrations are accurately corrected in the pupil plane, which can be an explanation for high VA values in this experiment.

The low VA values for subjects S1, S2, S3 and S4 when doing visual testing with the correction of the manifest refraction were rather unexpected. Considering the normal VA values which they achieved with the AO-guided refraction correction, it might be due to the difficulty of obtaining accurate refraction with a standard optometric procedure, which uses trial lenses, for high myopes. In contrast, this experiment shows that the developed AOVS is a superior alternative, with higher precision of the obtained refraction and a faster measurement procedure.

Astigmatism may also be the reason for low VA in some cases. However, objective HS based measurement procedure provided an almost perfect estimation of the astigmatism, allowing to reach higher VA values.

In three subjects (S5, S6, S7) visual simulation was also performed for full wavefront correction, i.e., refraction combined with HOA. We have found a slight increase in visual performance, although it was not statistically significant ($p > 0.05$). That may be explained by the chosen pupil size, for the HOA amplitude is usually low for a pupil of 4.5 mm in young subjects. The benefit of full wavefront correction may increase for larger pupil diameters. Older population may have a larger visual benefit from HOA correction.

3.2 Vision through modified longitudinal chromatic aberration (LCA)

The effect of LCA on visual performance is a controversial topic. Some previous studies have found an increase in VA as well as in CS when LCA was corrected (Yoon and Williams, 2002; Artal et al., 2010). Others have reported no significant visual improvement (Campbell and Gubisch, 1967; Thibos, 1987; Thibos, Bradley, and Zhang, 1991; Bradley, Zhang, and Thibos, 1991; Benny et al., 2007) associated to the correction of LCA. In this context, through-focus visual performance with corrected, or modified, LCA has not been thoroughly studied. Through focus performance of vision under modified chromatic conditions might lead to a better understanding of the issue. Through-focus LCA correction has been studied primarily in the context of IOLs (Franchini, 2007; Fernández and Artal, 2017), reporting a connection between LCA and spherical aberration. Those works studied mainly changes in optical quality, without considering the perceptual part of vision. The LCA across the visible spectrum reaches almost 2 D (Campbell and Gubisch, 1967), so certain extent of perceptual chromatic effects, e.g. color halos would be expectable. On the contrary, in everyday vision most of the subjects never report such effects. This fact might be an indicator of certain neural compensation or adaptation mechanism to the effects of LCA.

Nowadays it is technically feasible to induce a range of LCA values in IOLs, contact lenses or even ophthalmic lenses. It can be done for the correction of LCA, or for inducing any value or sign of LCA in general. As IOLs are usually implanted in the aged and fully presbyopic eye, any possibility of extending the depth of focus is valuable and provides an advantage compared to other designs.

In this experiment the AOVS was used to investigate the effect of different LCA conditions on VA through-focus. Previously, studies with compensation of LCA (at the best focus) used manufactured achromatizing lenses (Bradley, Zhang, and Thibos, 1991; Thibos, Bradley, and Zhang, 1991; Benny et al., 2007) or a diffractive phase element (Artal et al., 2010). However, a method has recently been described (Martínez et al., 2017)

where chromatic aberration was controlled by the means of a phase mask generated by a LCoS-SLM.

Figure 3.6 graphically shows the three LCA conditions considered in the experiment. Baseline measurements were done with the natural LCA, and then compared to compensated and doubled LCA conditions. The spectral range considered for visual testing was 450 to 630 nm (Schnapf, Kraft, and Baylor, 1987).

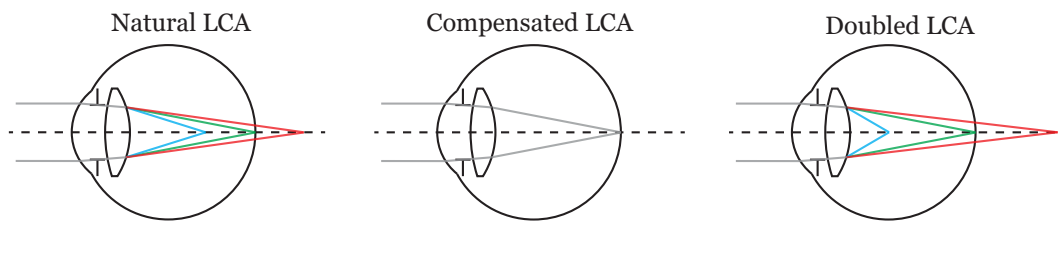


FIGURE 3.6: Representation of the three chromatic conditions used in the experiment (not to scale)

To complement the experimental results, ray-tracing simulations with a chromatic eye model were done, as described in section 3.2.2. The chromatic eye model was coupled with the LCA conditions to obtain the modulation transfer functions (MTF) through-focus. To transition from optical quality to visual performance, a semi-empirical method to estimate VA was adopted (Alarcon et al., 2016). The eye model included a weighed spectral function (accounting for the spectrum of the stimulus, spectral sensitivity of the eye and the absorption of the ocular media), and Stiles-Crawford effect of the first kind (SCE-I).

Comparison of experimental results with predictions from simulations allowed to separate the optical effects from neural effects coming from a modified chromatic condition.

3.2.1 Experimental measurements

The method to control LCA (Martínez et al., 2017) takes advantage of the 2π - phase wrapping required to modulate any phase above a wavelength in amplitude. Due to this phase wrapping, the modulated profile is diffractive in nature, which results in a chromatic dispersion of the wavefront when

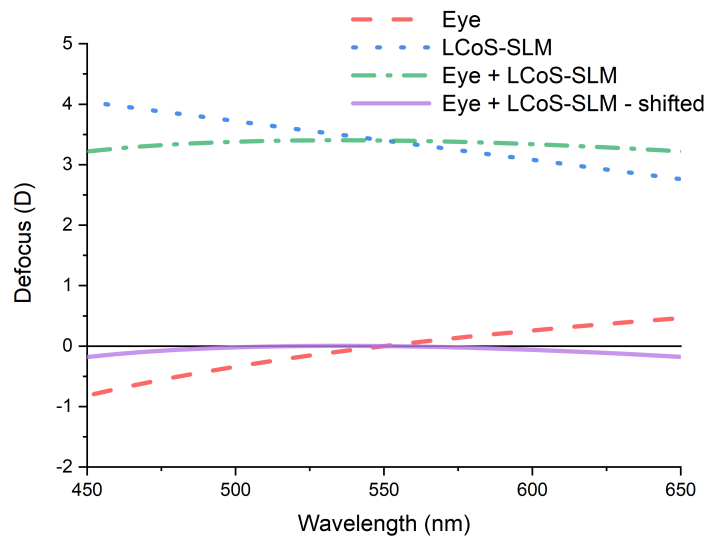


FIGURE 3.7: Theoretical produced defocus as a function of the wavelength in the visible range. Red dashed line represents an emmetropic eye. Blue dotted line shows the LCoS-SLM (3.4 D for 550 nm) contribution. Green dash-dotted line shows the eye combined with the LCoS-SLM. Purple solid line represents the eye after the defocus shift with a TL.

LCoS-SLM is illuminated with polychromatic light. When a defocus-only lens is programmed on the modulator, a linear dispersion of the wavelengths is produced.

The slope of the chromatic dispersion depends on the power of the lens generated on the modulator. Thus, for a given spectral range, a power can be calculated to produce the required chromatic shift. Then the carrier power of the lens at the reference wavelength can be compensated by the TL, producing a pure chromatic shift. The so generated chromatic shift was then combined with the eye's natural LCA, producing the desired chromatic condition. The procedure is graphically shown in Fig. 3.7. The LCA of the eye was taken from a different study (Atchison and Smith, 2005). The reference wavelength was taken at 543 nm.

For setting the desired experimental chromatic conditions, the following carrier defocus were set at the LCoS-SLM: 0 D (no modulation) for natural LCA (chromatic shift of 1.2 D in the eye); 3.4 D for compensated LCA (total chromatic shift of 0 D in the eye); and -3.4 D for doubled LCA (total

chromatic shift of 2.4 D in the eye).

In order to perceive a flatter spectrum, accounting the photopic spectral sensitivity of the photoreceptors, the channels red and blue of the illuminating LEDs were raised in the display. Considering spectral sensitivity of the photoreceptors of the eye (Schnapf, Kraft, and Baylor, 1987), this resulted in a slight magenta-colored tint of the stimulus. Luminance at the pupil plane was 100 cd/m^2 . The motorized pupil was set at 4.5 mm.

3.2.1.1 Subjects

Four healthy adults (ages of 26, 42, 45, and 44 years old) participated in the experiment. The subjects exhibited a mean spherical refractive error of $-0.3 \pm 1.67 \text{ D}$; and astigmatism of $-0.5 \pm 0.12 \text{ D}$. Cycloplegics were instilled in the eye in order to paralyze accommodation. The subjects were informed about the purpose of the experiment, and they consented to participate in the measurements.

3.2.1.2 Validation of the chromatic shift

For objective validation of the chromatic shift, an auxiliary CMOS camera (DMK 72AUC02, The Imaging Source Europe GmbH, Bremen, Germany) was placed in the intermediate image plane after the lens L2, as shown in Fig. 3.8 in order to verify that the experimental chromatic shifts corresponded to the theoretical values. The camera had a resolution of 2592×1944 pixels, with a pixel pitch of $2.2 \mu\text{m}$.

Carrier defocus values for generating the desired LCA conditions were programmed on the LCoS-SLM. The TL compensated the bulk or carrier defocus at 550 nm. Interference filters centered at 430, 550 and 630 nm wavelengths (10 nm bandwidth) were introduced into the system close to the motorized pupil, as shown in 3.8. The image on the auxiliary camera was first defocused by 1 D by the TL. Best focus position was found by changing the defocus of the TL and analyzing images of a standard USAF-1951 object on the camera. The procedure was repeated for each wavelength, allowing to retrieve the chromatic shift curve. Defocus values were then shifted to the reference wavelength of 550 nm.

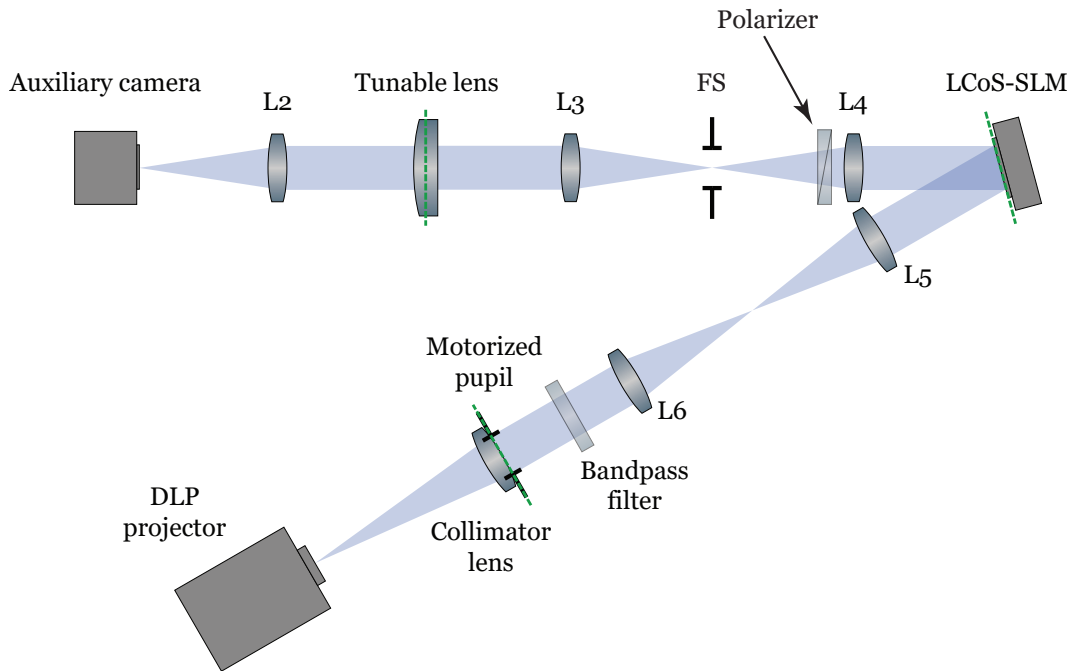


FIGURE 3.8: Experimental measurements of chromatic shift. Bandpass filter denotes the place where one of three interference filters were introduced into the system. Dashed green lines show conjugated planes.

The procedure for finding the best focus was based on the maximum variance of the image received on the camera. The measurements were repeated three times to account for the uncertainty introduced by the TL, which reached 0.15 D, as described in section 2.6.1. Results are shown in Fig. 3.9

The maximum difference between experimental measurements and theoretical calculations was 0.04 D with a standard deviation (SD) of 0.081 D. The error can be explained by the defocus inaccuracy of the TL.

The validation was repeated visually, asking the subjects to find their best focus under modified LCA conditions, looking at a Maltese cross with a size of 1 degree. The results are shown in Fig. 3.10. Subjective measurements combined the natural LCA of the eye with the LCA introduced by the LCoS-SLM, which is reflected by the theoretical curves, which combine theoretical data from Fig. 3.9 with natural LCA. Natural LCA measurements are shown as a baseline, with no modulation from LCoS-SLM.

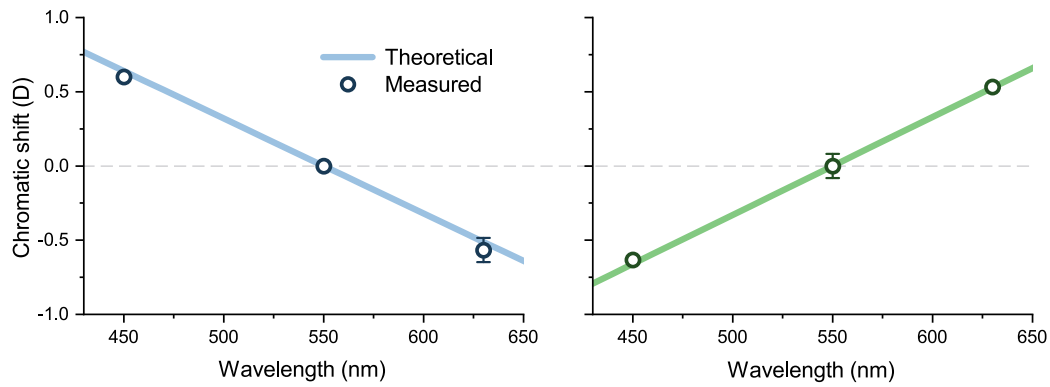


FIGURE 3.9: Measured chromatic shift for compensation of the eye's LCA (left panel) and for doubling of the eye's LCA (right panel). The error bars show the standard deviation.

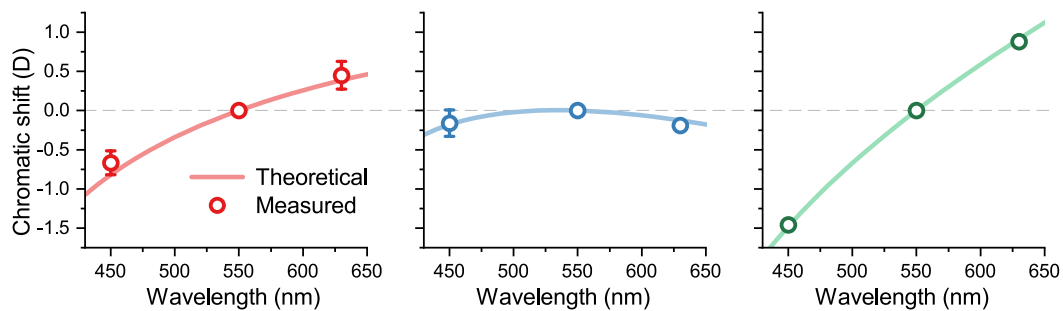


FIGURE 3.10: Averaged measured LCA curves for four subjects. Left panel shows natural LCA, middle - compensated LCA, right - doubled LCA. Error bars represent standard deviation, omitted when too small for the figure.

In the case of subjective measurements, maximum deviation of experimental points from the theoretical curve reached 0.22 D for the case of doubled LCA, with maximum SD of 0.17 D. The depth of focus of the eye for 4.5 mm (Wang and Ciuffreda, 2006) explained the increased variability when compared to measurements with the camera.

Overall, both objective and subjective measurements showed that the method of LCA control using the LCoS-SLM produced the expected chromatic shift.

3.2.1.3 Through-focus VA measurements

The subjects were fixed to the system by a chin rest instead of a dental impression for extra comfort. The pupil position was constantly monitored. The subjects first found their best focus position for polychromatic light using a keyboard to act over the TL for each LCA condition. The fixation target was a black Maltese cross subtending 1 degree with concentric circles on a white background.

The through-focus VA measurements were taken for each LCA condition within the range of -1.5 to +1.5 D. One step equaled to 0.3 D, resulting in a total of 11 VA measurements for a single chromatic condition.

The VA was obtained using the Freiburg test (Bach, 1996) with 90 trials. Each trial presented an E letter in one of four possible orientations. The participants used a keyboard to indicate the orientation of the letter while looking through the system. Responses of the subjects were fit to a Boltzmann sigmoid function, with the VA threshold set at 75% of correct answers. Results are shown in Fig. 3.11.

Maximum VA values were found to be: 1.37 ± 0.06 for natural LCA; 1.27 ± 0.02 for compensated LCA; and 1.08 ± 0.04 for double LCA. To provide an analytical description of the VA curves, the data was fitted to Gaussian functions in order to calculate full width half maximum (FWHM) values. The FWHM values were: 1.67 for natural LCA; 1.31 for compensated LCA; and 2.39 for doubled LCA. Results show that compensation of chromatic aberration provides a slightly lower VA curve than for the baseline condition of natural chromatic aberration. Doubling chromatic aberration dropped the VA curve further, while flattening its shape.

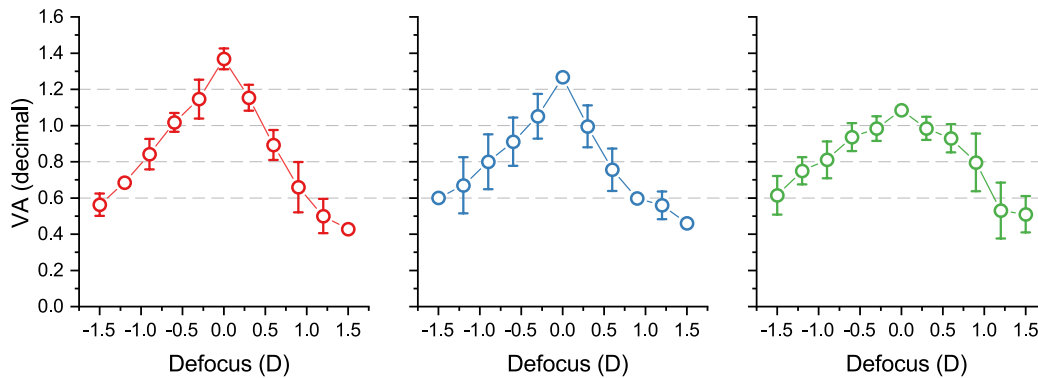


FIGURE 3.11: Average VA across the depth-of-focus for four subjects. Error bars indicate standard deviation. Left panel shows natural LCA, middle - compensated LCA, right - doubled LCA.

Performing a statistical analysis using a Student's two-sided t-test on natural LCA and compensated LCA VA curves, no statistical difference was found ($p > 0.05$) for any of the sampled defocus points. Comparing natural LCA with doubled LCA, differences between VA values at defocus points of 0 D and 0.3 D were statistically significant ($p < 0.05$).

3.2.2 Ray-tracing simulations

3.2.2.1 Optical model

The chromatic eye model was based on a previous work (Fernández and Artal, 2017) with corneal conic constant optimized for producing a diffraction-limited image on the fovea for the reference wavelength (550 nm). The model provided accurate LCA on axis. The parameters of the eye are shown in Table 3.2. A pupil size of 4.5 mm, same as in the experimental measurements, was used. Ray-tracing simulations were done using optical design professional software (Zemax, LLC, Washington, USA).

Dealing with LCA, it was especially important to consider the spectral weighting. In order to simulate experimental conditions as close as possible, weighting was done using a retinal spectral luminance, which calculation is shown in Eq. 3.2. It considers the spectral irradiance of the stimulus, spectral transmittance of the ocular media, and the spectral sensitivity of the

TABLE 3.2: Parameters of eye model. Unit for radius, thickness and semi-diameter is mm.

Surface	Radius	Thickness	Refractive index	Abbe number	Semi-diameter	Conic constant
Anterior cornea	7.77	0.55	1.3766	55.7029	5	-0.708
Posterior cornea	6.4	3.16	1.3375	50.6963	5	-0.6
Iris	Infinity	—	—	—	2.25	—
Anterior lens	10.2	4	1.4201	50.7824	5	-3.132
Posterior lens	-6	16.503	1.3361	53.5626	5	-1
Retina	-12	—	—	—	—	—

photoreceptors (Campbell and Gubisch, 1967) were taken into account to model the experimental conditions as close to reality as possible. Equation 3.2 summarizes the weighting function applied in the model.

$$E(\lambda) = L_n(\lambda) \cdot T_n(\lambda) \cdot S_n(\lambda), \quad (3.2)$$

where $L_n(\lambda)$ is proportional to the spectral irradiance of the source, $T_n(\lambda)$ is the normalized ocular transmittance (Boettner and Wolter, 1962), and $S_n(\lambda)$ is the photopic spectral sensitivity of the eye (Schnapf, Kraft, and Baylor, 1987).

Figure 3.12 shows the resulting retinal spectral illuminance. The function was then resampled into 13 points which were in the ray-tracing simulations.

Another factor taken into account in the simulations was the Stiles-Crawford effect (SCE) of the first kind (Stiles and Crawford, 1933; Snyder and Pask, 1973). It has been shown that it has an effect on VA (Atchison et al., 2002). It can be modeled as a Gaussian apodization filter of the pupil (Zhang et al., 1999). The SCE directionality parameter ρ was set at 0.055 (Applegate and Lakshminarayanan, 1993). The ray-tracing software defined the Gaussian apodization factor as 1 divided by e^2 and ratio between

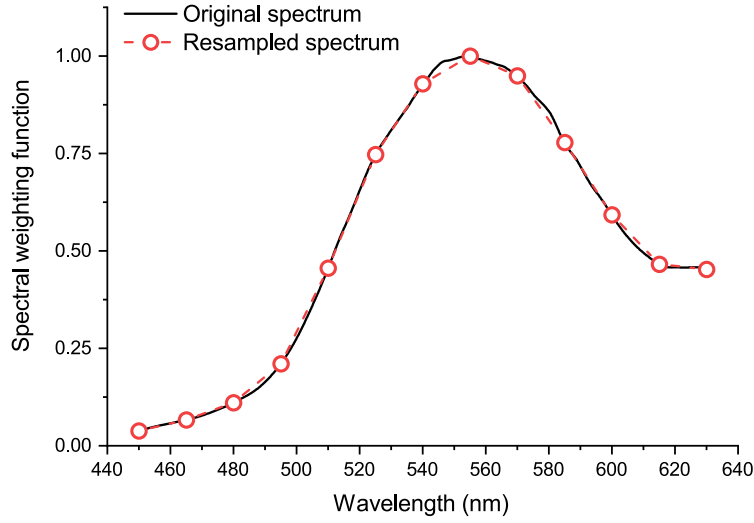


FIGURE 3.12: Spectral weighting function used for the simulations. The red circles represent the function resampled for 13 points used in the ray-tracing software.

the intensity in the center of the pupil and at the edge of the pupil (Elliott, 2016). Eq. 3.3 shows the calculation of the apodization factor (assuming the maximum intensity is at the center of the pupil). The apodization factor calculated from Eq. 3.3 equaled 0.24.

$$A_G(x, y) = e^{-2} \cdot \eta_{edge}(x, y) / \eta_{max}, \quad (3.3)$$

where $A_G(x, y)$ - Gaussian apodization factor, η_{max} is the maximum relative sensitivity (assumed to be in the center of the pupil, equal to 1), $\eta_{edge}(x, y)$ is the relative sensitivity at the edge of the pupil, found from the SCE directionality parameter ρ .

As the directionality parameter depends on the wavelength, a value of ρ equal to 0.075 (Stiles, 1937) was tested as well. The modulation transfer function (MTF) areas for two different directionalities were compared, with the maximum difference (depending on optical aberrations) of around 0.15%. Due to this, for further ray-tracing simulations, the directionality parameter was assumed to be independent of wavelength, similar to other studies (Atchison et al., 2002).

For modeling the LCA conditions, two ideal chromatic triplets were designed. These produced the required chromatic shifts corresponding to compensated LCA (T_{comp}) and doubled LCA (T_{doub}). The parameters of the perfect or ideal triplets are shown in Table 3.3. The triplets were symmetrical to avoid extra high order aberrations, and they were placed next to the eye.

TABLE 3.3: Parameters of achromatizing triplets. Unit for radius, thickness and semi-diameter is mm.

Surface	Radius		Thickness	Refractive index	Abbe number	
	T_{comp}	T_{doub}			T_{comp}	T_{doub}
1	Infinity	Infinity	0.9	1.61	36.4	28.3
2	14.085	-14.085	5.2	1.61	57.0	39.2
3	-14.085	14.085	0.9	1.61	36.4	28.3
4	Infinity	Infinity	—	—	—	—

The chromatic shifts generated by the combination of the eye model and the triplets are shown on Fig. 3.13.

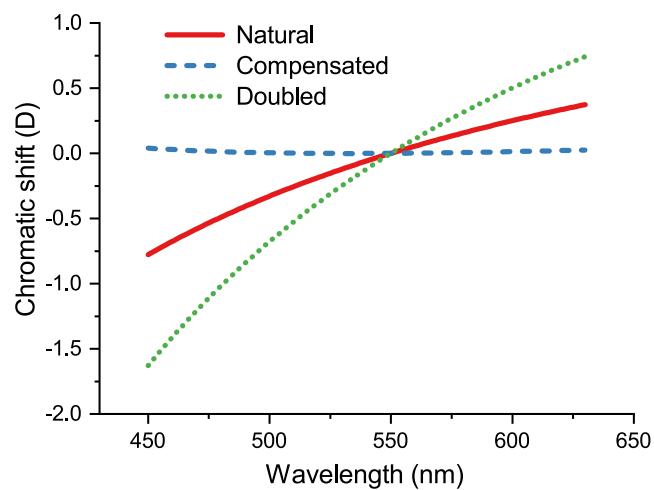


FIGURE 3.13: LCA produced in ray tracing simulations.

The chromatic shifts of the model were 1.21 D for natural LCA; 0.06 D for compensated LCA; and 2.39 for doubled LCA.

3.2.2.2 VA prediction

A semiempirical formula (Alarcon et al., 2016) was used to predict the VA from the optical quality of the retinal images of the eye model. The formula was developed to model the VA through-focus under polychromatic conditions for patients implanted with intraocular lenses. It showed remarkable correlation with the experimental VA measurements. The metric employs the area under the MTF up to 60 cycles per degree, weighted with a typical human eye CSF.

Eq. 3.4 and Eq. 3.5 show the calculation of the VA from the MTF (cycles per mm is used in the calculations).

$$wMTFa = \sum_{f=1}^{150/d} \frac{d}{150} MTF(fd) CS_{th}(fd), \quad (3.4)$$

where $wMTFa$ is the weighted MTF area, d is sampling size of the spatial frequency f , $MTF(fd)$ is the optical MTF, $CS_{th}(fd)$ is a contrast sensitivity threshold, or contrast sensitivity function (CSF).

The transition from the weighted MTF area to visual acuity is given by the following parametrized expression:

$$VA_{dec}(wMTFa) = 10^{-(a \cdot wMTF^b + c)}, \quad (3.5)$$

where VA_{dec} is decimal VA, $a = 1.9793$, $b = -0.8$, $c = -0.18$.

Parameters a , b and c were taken from the work of Alarcon et al. (Alarcon et al., 2016), where through-focus VA was measured for 243 subjects and correlated with the weighted MTF area.

Figure 3.14 graphically shows the effect of weighting the MTF. The left panel shows the MTF achieved in the compensated LCA case, for 0.3 D of defocus. The CSF used here is a classic model by Campbell & Green (Campbell and Green, 1965). The right panel shows the weighted MTF, produced by multiplication of the MTF with the CSF. Frequencies around 6 to 8 cpd are given more importance than frequencies from 0 to 5 cpd, even though MTF was higher for the lower frequencies. At higher frequencies around 30 cpd, MTF is showing values around 0.1, while weighting makes them much less importance. Shaded area in Fig. 3.14 shows the area of the weighted MTF which is calculated in Eq. 3.4.

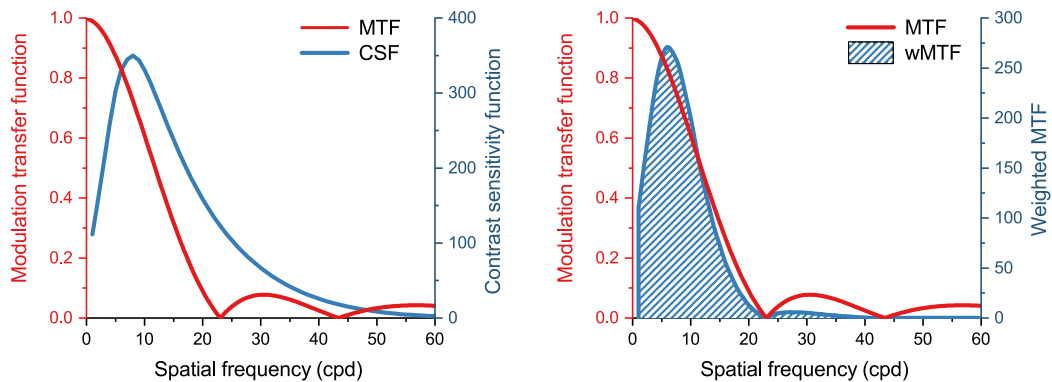


FIGURE 3.14: Weighted MTF area calculation. Left panel - MTF (red line) with the CSF (blue line). Right panel - MTF (red line) with weighted MTF (blue line). Weighted MTF area is shaded.

Mirroring the experimental conditions, the area of the weighted MTF was calculated through focus, from -1.5 to $+1.5$ D with a step of 0.3 D. 13 values of wMTFa were produced for each chromatic conditions, out of which the resulting VA values were calculated using Eq. 3.5. Figure 3.15 shows the results. Left panel shows the MTF areas (not weighted, in order to highlight the importance of considering the CSF), while right panel shows the corresponding VA predicted for every condition.

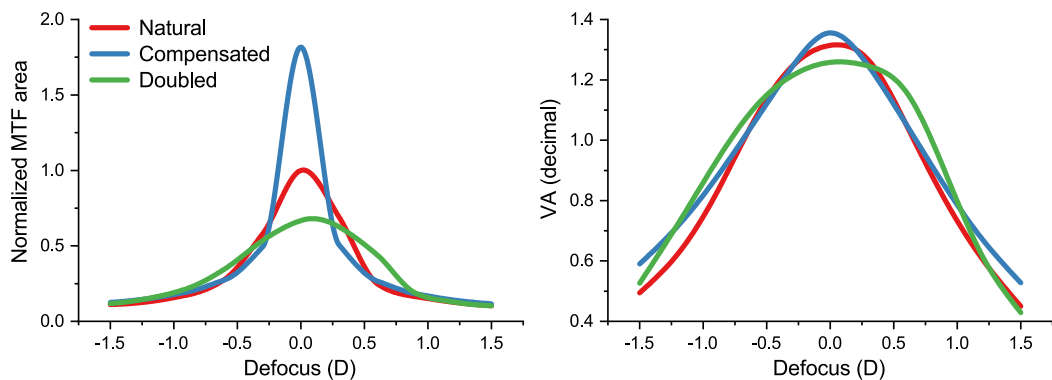


FIGURE 3.15: MTF area and predicted VA values comparison. Left panel - through-focus MTF area values. Right panel - predicted VA values.

Comparing compensated LCA to the natural LCA, the MTF area is almost doubled. However, this does not translate to that extent into the VA. The predicted benefit of VA is modest, around 3.2%. Moreover, doubling the LCA resulted in a reduction of MTF area of 32%, while the predicted VA decreased only by 4.2%.

3.2.3 Discussion

The method to control the LCA was tested and proved to be very precise. The effect of manipulating the LCA was also tested in real subjects, who were asked to find their best focus monochromatically, reproducing the theoretical curves.

The method of LCA control using an LCoS-SLM imposes certain limitations. For any wavelength different from the one used for calculating the phase masks, multiple diffractive orders occur, distributing the energy between them, thus reducing the contrast. According to the existing literature, a moderate contrast drop does not affect the results of VA (Johnson and Casson, 1995). In this work, the contrast drop associated to diffraction in the AOVS was measured for the case of compensated LCA using a camera at an intermediate image plane, as described in section for objective LCA modulation measurements. For a stimulus being a tumbling E letter corresponding to VA of 1, the drop on contrast equaled 10%, down from 98% to 88% in white light. VA at contrast of 88% would be indistinguishable from VA at contrast of 100% (Johnson and Casson, 1995). As an extra test, VA for one of the subjects was obtained in the AOVS for two conditions: with the phase mask corresponding to compensated LCA (case 1), and with no modulation of LCA (case 2), leaving LCoS-SLM off. This way the negative effect introduced by the diffractive nature of LCoS-SLM was isolated from effect of modulated LCA. VA in case 1 was 1.33 ± 0.12 , while in case 2 it was 1.31 ± 0.17 . This result suggests that the observed difference in the VA curves is due to the visual perception of modified LCA and not due to the method itself.

Regarding the through-focus measurements, it was found that not only the correction of the LCA did not result in an improvement of VA at the best focus, but even a slight drop of 0.1 VA decimal was measured. Doubling

the LCA produced a considerable decrease of VA at the best focus position, around 0.29 units in decimal scale. The evolution of through focus VA under compensated LCA was not significantly different from the natural case.

Manipulating the LCA could produce different effects for mesopic or scotopic vision. Some of the experimental conditions might have had an impact in the results. For example, HOA were uncorrected in order to not disturb the chromatic modulation by the LCoS-SLM. It has been suggested before that the presence of HOA may diminish the effect of LCA correction (Zhang, Thibos, and Bradley, 1997; McLellan et al., 2002; Ravikumar, Thibos, and Bradley, 2008). However, the HOA of the subjects were in a normal range, and a relatively small pupil of 4.5 mm was used. The average wavefront RMS error of the subjects was 0.21 ± 0.05 (mean \pm SD). In order to correct HOA, a separate corrector not introducing any chromatic effect, such a deformable mirror would have to be used. For the similar reason, astigmatism was also left uncorrected. Although, since it was below 0.75 D for all subjects, little effect if any is expected on the results.

Thorough ray-tracing simulations of the eye coupled to the studied chromatic conditions allowed a better understanding of the LCA's influence on the optics and vision.

It was noted earlier (Tabernerero and Artal, 2012) that the difference between achromatizing axis location and center of the pupil may affect the visual performance. However, when the achromatizing axis position was measured, the difference mentioned above was below 0.2 mm for all four subjects. HOA were present as well, and were under consideration to put into the model. Figure 3.16 shows the comparison between VA predictions for all three chromatic conditions for the eye used in the results, and for the eyes with HOA included or TCA included. Angle between the visual axis and achromatizing axis was taken at 3 degrees (Rynders et al., 1995).

As it can be seen in Fig. 3.16, the inclusion of either TCA or HOA has the most effect on the case of compensated LCA, which is intuitive since this is the case with the highest optical quality at best-focus. For natural LCA the difference between the eye models is less significant, while for the doubled LCA case the difference becomes negligible. Nonetheless, inclusion of TCA or HOA mostly affects the through-focus visual performance, as the difference between best focus VA for different chromatic conditions is below 0.03

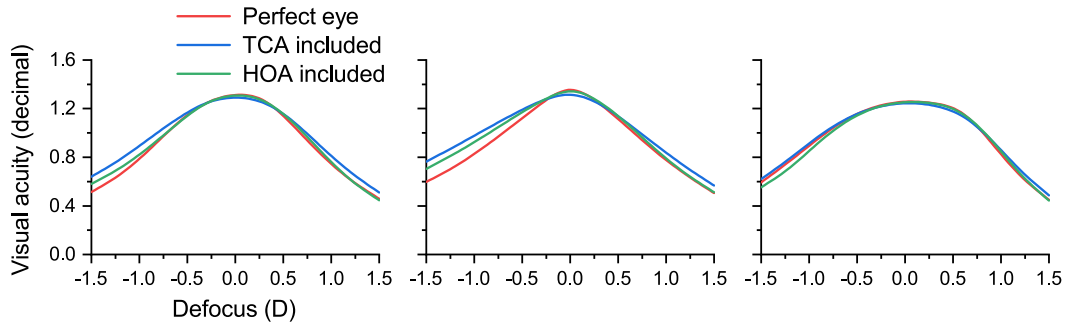


FIGURE 3.16: Comparison between predicted VA for different eye models. Left panel - natural LCA; middle panel - compensated LCA; right panel - doubled LCA. TCA is taken for the angle of 3 degrees between achromatic and visual axis.

decimal in all cases.

The semiempirical formula allowed to predict VA based on the optical quality of the retinal images. Comparison of the experimental and predicted VA is shown in Fig. 3.17.

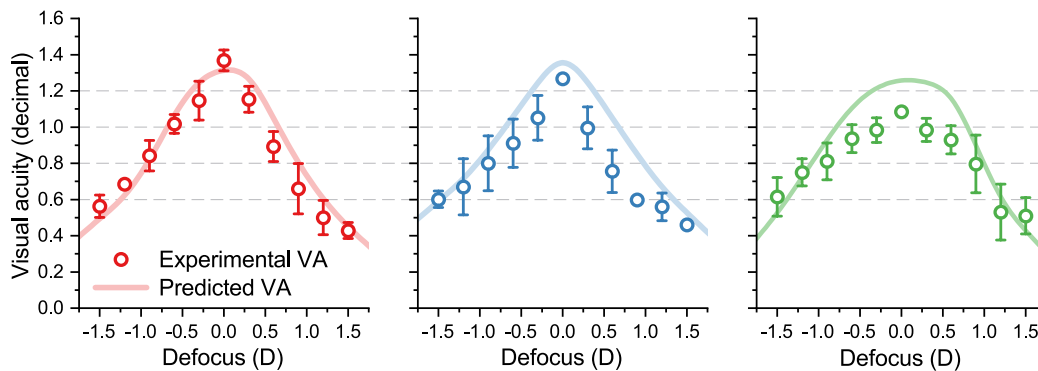


FIGURE 3.17: Visual acuity from simulations and experimental measurements. Left panel - natural LCA; middle panel - compensated LCA; right panel - double LCA. Error bars represent standard deviation.

To have a better comparison between the predicted and experimental VA, a correlation between set of data was performed. The coefficient of correlation R^2 for the natural case was 0.92; compensated LCA resulted in a $R^2 = 0.84$; and doubled LCA produced an $R^2 = 0.59$. For the natural LCA, the

correlation was remarkable, confirming the reliability of the method to predict VA. Even though initially it was conceived for patients implanted with IOL, which typically exhibit lower VA values, the method performs for the group of healthy young adults with normal vision. However, for the modified chromatic LCA, the accuracy of the prediction decreases, especially for doubled LCA condition. The method was developed for the natural LCA in polychromatic light, and it uses a CSF for weighting the MTF before transitioning into VA values. CSF seems to play a key role here. The prediction of VA could be adjusted to experimental results by modifying CSF. This fact provides an interesting clue about the possible explanation of the results: CSF might be tuned depending on the chromatic conditions, revealing a possible new effect of neural adjusting or adaptation to visual conditions.

It is known that neural system drives the perception of light under a certain chromatic state. For example, it has a significant effect on accommodation (Kruger and Pola, 1986; Kruger et al., 1993; Aggarwala, Nowbotsing, and Kruger, 1995; Graef and Schaeffel, 2012) and color perception (Flitcroft, 1989). It has been shown that human eye can adapt to sinusoidal gratings of certain colors (Bradley, Switkes, and Valois, 1988). Taking into account the results presented in this chapter, together with previous literature, the neural aspect of chromatic vision should be accounted when LCA manipulation is performed. Considering the ability of the visual system to adapt to monochromatic aberrations (Artal et al., 2004) and to color gratings (Bradley, Switkes, and Valois, 1988), the results can point to some neural adaptation.

3.3 Adaptation to corrected LCA

The results obtained in the through focus measurements of the VA under modified LCA conditions raised the question of possible neural components affecting the perception. In particular, the lack of benefit over the VA when correcting the LCA at best focus and high contrast and luminance was surprising and counterintuitive. Previous studies offer different results, including a benefit (Yoon and Williams, 2002; Artal et al., 2010), and no significant visual improvement (Campbell and Gubisch, 1967; Thibos, 1987; Thibos, Bradley, and Zhang, 1991; Bradley, Zhang, and Thibos, 1991; Benny et al., 2007). In the experiment presented in this chapter the issue is further addressed, specifically exploring new adaptation effects under modified LCA. The experimental conditions, the generation of the different cases of LCA, were like those presented in the previous chapter.

3.3.1 Experimental procedure

Subjects were fixed at the system using a chinrest, allowing for more comfort compared to the dental impression, considering that the entire procedure took about 1 hour.

In order to get the subjects used to the experimental procedure they underwent 4 baseline VA measurements in high contrast at luminance level of 100 cd/m^2 .

The second step involved subjects looking through their natural LCA and doing continuous VA tests, with no breaks allowed. 10 sets of VA measurements were done, with each taking an average of 1.88 ± 0.07 (mean \pm SD) minutes, for a total of 19 minutes. Immediately after the last step, LCA modulation using the LCoS-SLM was turned on, and subjects continued doing the VA testing with corrected LCA, doing another 10 sets of VA measurements. The same procedure was repeated for both high contrast (100%) and low contrast (10%) conditions. The 4 baseline VA measurements were always done in high contrast conditions. During the whole experiment subjects were looking through the system without a break or any external

distractions. VA was calculated from the raw data using a Boltzmann sigmoid fit, with VA threshold at 75% and a bottom asymptote at 0.25, same as in the studies described in sections 3.1 and 3.2.

3.3.2 Subjects

5 subjects (42, 27, 45, 44 and 35 years old) participated in the experiment, all of them nearly emmetropic adults with refraction of -0.7 ± 1.3 D (mean \pm SD). Cycloplegics were instilled every 30 minutes in order to paralyze accommodation.

3.3.3 Results

Figure 3.18 shows the results of the VA measurements obtained in high contrast, while Fig. 3.19 shows results obtained in low contrast. The results with the compensated LCA condition (right panel) exhibited lower VA compared to those obtained under natural LCA (left panel).

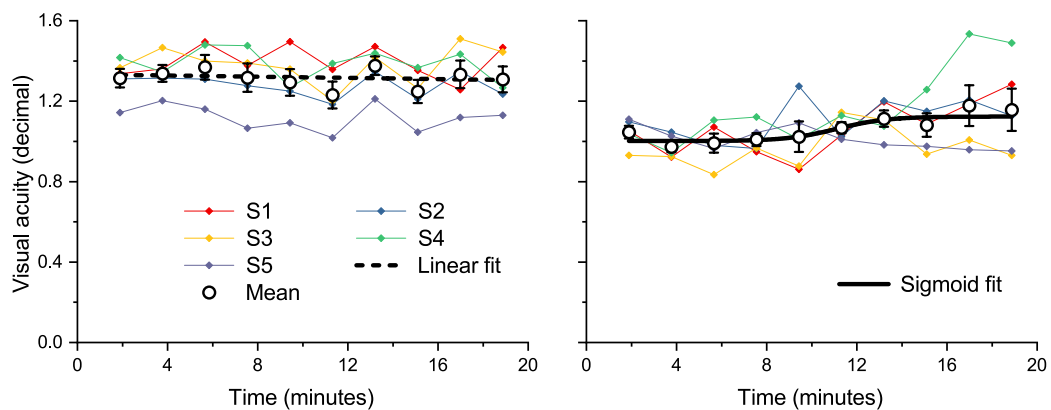


FIGURE 3.18: Visual acuity measured through time in high contrast. A Boltzmann sigmoid function is fitted to the mean data, shown by the solid line in the right panel. Linear fit is shown in left panel to show lack of VA evolution. Error bars indicate standard error of mean. Further explanation is in the text.

VA in natural LCA conditions did not evolve in time, as it turned evident from the linear fits shown in the left panels of Fig. 3.18 and Fig. 3.19, with

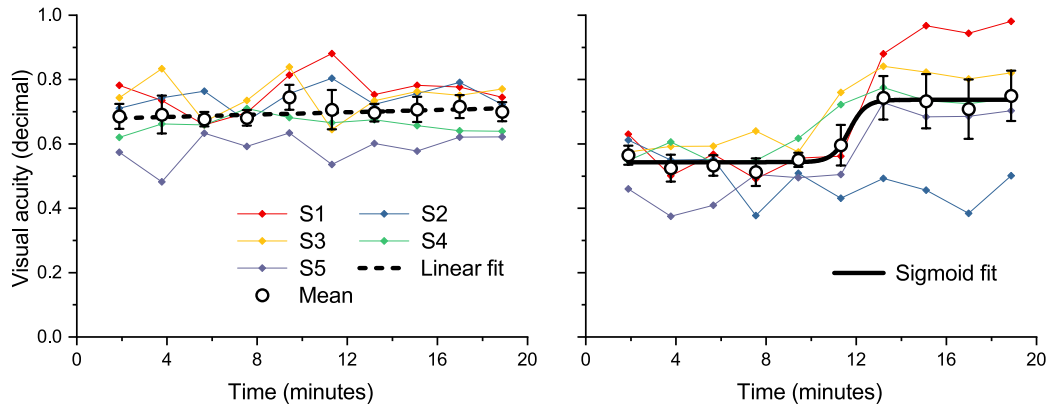


FIGURE 3.19: Visual acuity measured through time in low contrast. A Boltzmann sigmoid function is fitted to the mean data, shown by the solid line in the right panel. Linear fit is shown in left panel to show lack of VA evolution. Error bars indicate standard error of mean. Further explanation is in the text.

R^2 of 0.05 for high contrast and R^2 of 0.26 for low contrast. Vision through compensated LCA exhibited a subtle evolution of the VA in time for some subjects.

In order to better understand the results, Boltzmann sigmoid functions (using Levenberg-Marquardt fitting algorithm with all parameters left free) were fitted to all individual data with compensated LCA, as well as to the mean values across subjects. Eq. 3.6 shows the equation describing the sigmoid fit. Fits of the mean data can be seen in the right panels of Fig. 3.18 and Fig. 3.19.

$$y = A_2 + \frac{A_1 - A_2}{1 + \exp\left(\frac{x - x_0}{dx}\right)}, \quad (3.6)$$

where A_1 , A_2 , x_0 , and dx are fitting parameters.

The fitting is useful since it permits to define several parameters for characterizing a possible evolution of the VA through time. Those are: the gain in VA, calculated as the difference between the two horizontal asymptotes of the sigmoid ($A_1 - A_2$); adaptation delay would be represented by the starting point of the sigmoid's slope ($x_0 - 2 \cdot dx$); and adaptation time would be described by the projection of the slope on the X axis ($4 \cdot dx$).

A summary of the sigmoid fits in high contrast is shown in Table 3.4. Even though the fit quality was good (R^2 of 0.846), the mean data seem to be heavily skewed by the subject S4, as the individual fits for the rest of the subjects fail to produce meaningful results, as evident by their low R^2 values. The adaptation delay for subject S4 was at an almost 15-minute mark, closer to the end of the experiment. That suggests a possibility of other subjects being able to adapt as well, but in a longer time frame. The subject S4 was the youngest of the participants, being 27 years old.

TABLE 3.4: Responses to corrected LCA in high contrast. VA gain is given in decimal, time and latency in minutes.

Subject	VA gain	Time	Latency	R^2
S1	—	—	—	0.637
S2	—	—	—	0.491
S3	—	—	—	0.412
S4	0.45	0.37	14.83	0.920
S5	—	—	—	0.408
Mean	0.17	8.82	8.53	0.846

In low contrast, all of the subjects but one (S2) exhibited an evolution of their VA with time under compensated LCA viewing. The table 3.5 shows the summary of the results. The sigmoid fit of the average data produced a correlation coefficient $R^2 = 0.931$. All of the individual fits for exhibited R^2 values above 0.9. Subject S2 failed to show any change. Although it is not shown in the figures, the subject S2 underwent VA testing in low contrast with compensated LCA for extra 20 minutes, and no evolution was found. That suggests that this reported VA evolution in time associated to vision through corrected LCA is highly individual.

Figure 3.20 shows the VA evolution for the subjects S1, S3, S4 and S5 along with graphical representation of VA gain, time and delay calculation.

If only subjects S1, S3, S4 and S5 are considered (80% of the sample), the fit quality of the sigmoid to the mean data improves to R^2 of 0.99. In those

TABLE 3.5: Responses to corrected LCA in low contrast.

Subject	VA gain	Time	Latency	R^2
S1	0.41	1.56	11.89	0.966
S2	—	—	—	0.417
S3	0.23	0.62	11.09	0.971
S4	0.18	2.28	8.79	0.944
S5	0.25	0.64	11.23	0.912
Mean	0.19	1.48	10.93	0.931

subjects experiencing a VA evolution, the phenomenon appears highly predictable and well characterized with the sigmoid function.

3.3.4 Discussion

The results suggested that for some subjects there is a kind of adaptation to the compensated LCA condition, so that after some time their VA objectively improved. Showcasing an example of individual nature of the adaptation, subject S2 failed to adapt in both high and low contrast, even when low contrast VA testing was extended for another 20 minutes. Meanwhile the other 4 subjects successfully adapted to the compensated LCA in the low contrast. However, only one subject (S4) showed adaptation in high contrast as well. CSF measurements in natural and modified LCA conditions should provide a deeper insight into this adaptation effect. However, the temporal frame to sample the CSF with high precision at different frequencies might affect the results. In the other hand, in practice retrieving the CSF continuously in time appears as unaffordable with the current methods. In addition, the drop in contrast associated to the use of the LCoS-SLM would play a role, contrary to the case of VA estimations. Previous studies are in line with the discovered adaptation to compensated LCA. Neural system affects the perception of light for a given chromatic state. For example, it is well known that accommodative response is affected by the chromatic condition experienced by the subject (Kruger et al., 1993; Aggarwala, Nowbotsing, and Kruger, 1995; Graef and Schaeffel, 2012). Perception of color

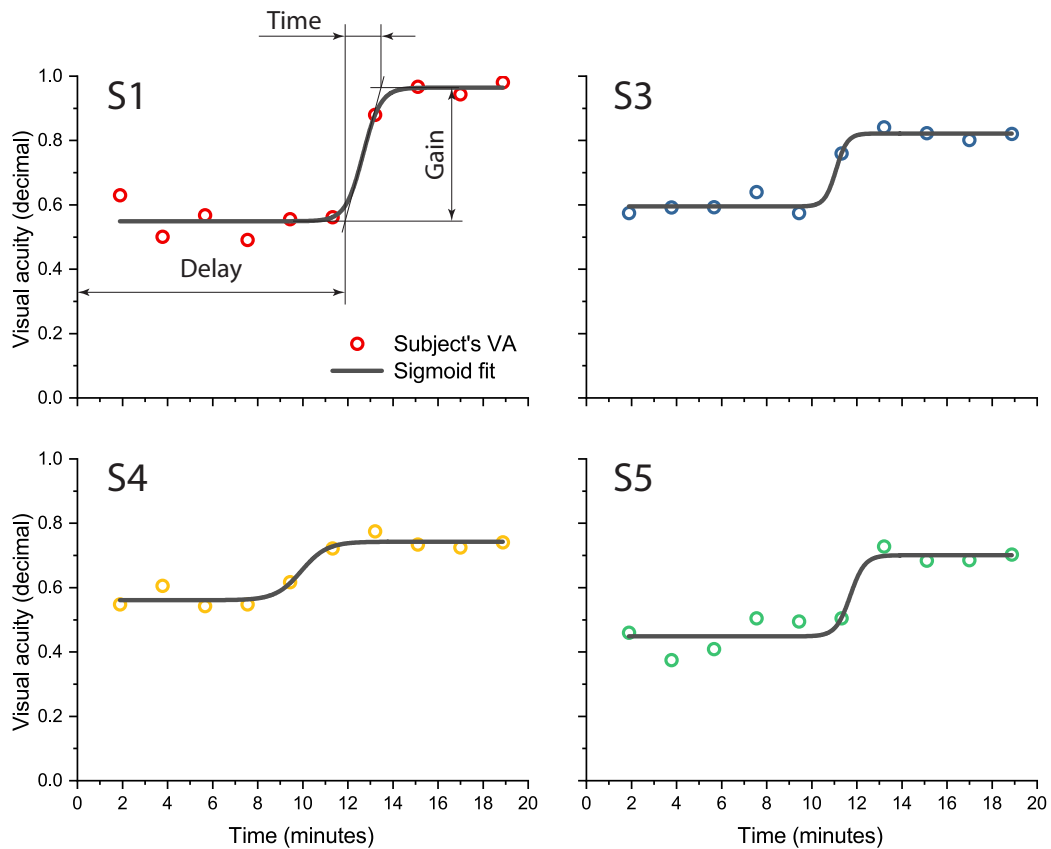


FIGURE 3.20: Adaptation to compensated LCA for subjects S1, S3, S4 and S5. Top left panel for subject S1 shows the calculation of the sigmoid's parameters describing the adaptation process.

also changes depending on the experienced LCA state (Flitcroft, 1989). Contrast sensitivity threshold was reported to increase when the eye adapted to sinusoidal gratings of certain colors (Bradley, Switkes, and Valois, 1988). Taking this into account, the adaptation to compensated LCA corresponds well to the current knowledge, especially as the visual system is in general highly adaptive, as has been previously shown for monochromatic aberrations (Bradley, Switkes, and Valois, 1988; Johnson and Casson, 1995; Artal et al., 2004; Chen et al., 2007; Sawides et al., 2010a; Venkataraman et al., 2015).

Higher prevalence of adaptation in low contrast can be explained by the increased sensitivity of visual system, as it was shown by Johnson et al. (Johnson and Casson, 1995), where VA was tested for different amounts of

blur. Sensitivity to blur shown in that case is relevant to the presented work, as in the compensated LCA case, the amount of defocus on the retina (in other words, blur) is reduced for the extreme wavelengths (blue and red).

Considering that previous literature shows conflicting results on the effects of LCA correction (Campbell and Gubisch, 1967; Thibos, 1987; Bradley, Zhang, and Thibos, 1991; Thibos, Bradley, and Zhang, 1991; Yoon and Williams, 2002; Benny et al., 2007; Artal et al., 2010), this experiment might help with understanding of color vision and of LCA's effect on vision. From a perspective of real-life application, the demonstrated effect of adaptation to compensated LCA affects the research of intraocular lenses with included LCA correction (Franchini, 2007; Fernández and Artal, 2017), as the neural effects have to be considered aside from just the optical quality.

4 Conclusions

- An enhanced adaptive optics visual simulator was successfully developed and tested, extending the benefits of AO visual simulation to patients suffering from virtually any refractive error, including those with high myopia. The system is compact, made from off-the-shell components, and it can be transferred to the clinics for performing experiments on a larger population. The enhanced AOVS incorporated a liquid-crystal-on-silicon spatial light modulator and a tunable lens for controlling defocus independently. This configuration significantly expanded the operating dioptric range of the visual simulator. A motorized iris allowed to enforce any pupil size within the full physiological range of the eye. A DMD-based projector provided the stimuli for visual testing, allowing to control the illuminance and the spectral characteristics of the stimuli. The developed system was used for a variety of experiments to advance our understanding of the visual process.
- The developed AOVS was tested with a small population of young highly myopic subjects, which would typically be outside of a working range of an AO-based clinical instrument. The AO guided refraction of the subjects was superior in precision to traditional refraction, allowing the subjects to achieve VA values similar to emmetropes. The correction of HOA produced an increase in the visual performance of those high myopes, again similar to what has been measured in the emmetropic eyes. The instrument demonstrated to be a faster and a more reliable alternative for obtaining refraction for every patient, irrespective of the refractive error.
- The measurements of the HOA in high myopes showed a similar amplitude to the one found in emmetropic eyes. The instrument allowed to measure HOA with a higher accuracy, as the tunable lens was used

to pre-compensate the equivalent sphere of the eye before the HS sensor, thus assuring a linear operation of the sensor.

- The AOVS was used to manipulate the longitudinal chromatic aberration, allowing to study its effects on vision. The LCA modulation accomplished by combining diffractive lens phase masks with the compensation of defocus at the central wavelength by the TL was tested both objectively and visually. The experimental results were in a good agreement with the theoretical predictions, demonstrating the capabilities of this approach.
- Visual acuity through-focus was measured with modified longitudinal chromatic aberration conditions. Measurements were done for natural LCA, acting as a baseline, compensated LCA and doubled LCA. Correcting the LCA did not improve the VA compared to the natural LCA case, while doubling the LCA further reduced the VA. Ray-tracing simulation of the human eye with the tested chromatic conditions was done in order to better understand the results. A semiempirical formula was used for transitioning from optical quality to VA values. In the natural LCA case, there was an excellent agreement between the predicted VA and the measured one ($R^2 = 0.93$). However, for compensated and doubled LCA, the predicted VA was consistently higher, suggesting that contrast sensitivity function (assumed to be constant in the semiempirical formula) changes with the chromatic condition. This behavior points to the change in neural function as well.
- VA predictions from ray-tracing simulations of the chromatic conditions showed that the VA change is not directly proportional to the optical quality. In fact, it was found that the through-focus predicted VA curves corresponding to each chromatic condition were relatively similar. The change in depth-of-focus was also moderate, raising a question of feasibility of LCA manipulation to improve vision through-focus in real-life applications.
- The AOVS allowed to conduct a series of experiments to study the evolution on time of the VA under modified LCA conditions. A new adaptation effect was discovered, producing a boost in the VA after a

period of continuous viewing under a corrected LCA. The effect was found to occur mostly in low contrast (10%), and it was highly individual dependent. VA values raised by 0.2 in decimal scale on average. These adaptation effects are of a significant importance for ophthalmic design, as they introduce a new variable - the observed neural effects - to account for when testing or predicting the effects of LCA.

Bibliography

- Aggarwala, K. R., Nowbotsing, S., and Kruger, P. B. (1995). "Accommodation to monochromatic and white-light targets". In: *Investigative Ophthalmology & Visual Science* 36.13, pp. 2695–2705.
- Alarcon, A., Canovas, C., Rosen, R., Weeber, H., Tsai, L., Hileman, K., and Piers, P. (2016). "Preclinical metrics to predict through-focus visual acuity for pseudophakic patients". In: *Biomedical Optics Express* 7.5, pp. 1877–1888.
- Algvere, P. V., Jahnberg, P., and Textorius, O. (1999). "The Swedish Retinal Detachment Register. I. A database for epidemiological and clinical studies". In: *Graefe's Archive for Clinical and Experimental Ophthalmology* 237.2, pp. 137–144.
- Anderson, B. Y., J., S., Mullen, K. T., and Hesst, R. F. (1991). "Human Peripheral Spatial Resolution for Achromatic Retinal Factors". In: *Journal of Physiology* 442, pp. 47–64.
- Applegate, R. A. and Lakshminarayanan, V (1993). "Parametric representation of Stiles-Crawford functions: normal variation of peak location and directionality." In: *Journal of the Optical Society of America A* 10.7, pp. 1611–23.
- Applegate, R. A., Ballentine, C., Gross, H., Sarver, E. J., and Sarver, C. A. (2003). "Visual acuity as a function of Zernike mode and level of root mean square error." In: *Optometry and Vision Science* 80.2, pp. 97–105.
- Artal, P., Benito, A., and Taberero, J. (2006). "The human eye is an example of robust optical design." In: *Journal of Vision* 6.1, pp. 1–7.
- Artal, P. and Taberero, J. (2008). "The eye's aplanatic answer". In: *Nature Photonics* 2.10, pp. 586–589.
- Artal, P., Chen, L., Fernández, E. J., Singer, B., and Manzanera, S. (2003). "Adaptive optics for vision: The eye's adaptation to point spread function". In: *Journal of Refractive Surgery* 19.5, S585–S587.

- Artal, P., Chen, L., Fernández, E. J., Singer, B., Manzanera, S., and Williams, D. R. (2004). "Neural compensation for the eye's optical aberrations". In: *Journal of Vision* 4.4, pp. 281–287.
- Artal, P., Manzanera, S., Piers, P., and Weeber, H. (2010). "Visual effect of the combined correction of spherical and longitudinal chromatic aberrations". In: *Optics Express* 18.2, pp. 1637–1648.
- Atchison, D. A., Charman, W. N., and Woods, R. L. (1997). "Subjective depth of focus of the eye". In: *Optometry and Vision Science* 74.7, pp. 511–520.
- Atchison, D. A. and Smith, G. (2000). *Optics of the human eye*.
- (2005). "Chromatic dispersions of the ocular media of human eyes". In: *Journal of the Optical Society of America A* 22.1, pp. 29–37.
- Atchison, D. A., Scott, D. H., Strang, N. C., and Artal, P. (2002). "Influence of Stiles-Crawford apodization on visual acuity." In: *Journal of the Optical Society of America A* 19.6, pp. 1073–1083.
- Babcock, H. (1953). "The possibility of compensating astronomical seeing". In: *Astronomical Society of the Pacific* 65.386, pp. 229–236.
- Bach, M. (1996). "The Freiburg visual acuity test - automatic measurement of visual acuity". In: *Optometry and Vision Science* 73.1, pp. 49–53.
- Bedford, R. E. and Wyszecki, G. (1947). "Axial chromatic aberration of the human eye". In: *Journal of the Optical Society of America* 47.6, pp. 564–565.
- Benny, Y., Manzanera, S., Prieto, P. M., Ribak, E. N., and Artal, P. (2007). "Wide-angle chromatic aberration corrector for the human eye". In: *Journal of the Optical Society of America A* 24.6, pp. 1538–1544.
- Bergeron, A., Gauvin, J., Gagnon, F., Gingras, D., Arsenault, H. H., and Doucet, M. (1995). "Phase calibration and applications of a liquid-crystal spatial light modulator." In: *Applied optics* 34.23, pp. 5133–5139.
- Bigelow, C. E., Iftimia, N. V., Ferguson, R. D., Ustun, T. E., Bloom, B., and Hammer, D. X. (2007). "Compact multimodal adaptive-optics spectral-domain optical coherence tomography instrument for retinal imaging". In: *Journal of the Optical Society of America A* 24.5, pp. 1327–1336.
- Boettner, E. A. and Wolter, J. R. (1962). "Transmission of the ocular media". In: *Investigative Ophthalmology & Visual Science* 1.6, pp. 776–783.
- Born, M. and Wolf, E. (1993). *Principles of Optics*. Pergamon Press, Oxford.
- Bourne, R. R., Stevens, G. A., White, R. A., Smith, J. L., Flaxman, S. R., Price, H., Jonas, J. B., Keeffe, J., Leasher, J., Naidoo, K., Pesudovs, K., Resnikoff,

- S., and Taylor, H. R. (2013). "Causes of vision loss worldwide, 1990-2010: A systematic analysis". In: *The Lancet Global Health* 1.6, pp. 339–349.
- Bowmaker, J. K. and Dartnall, H. J. (1980). "Visual pigments of rods and cones in a human retina." In: *The Journal of Physiology* 298.1, pp. 501–511.
- Bradley, A., Switkes, E., and Valois, K. D. E. (1988). "Orientation and spatial frequency selectivity of adaptation to color and luminance gratings". In: *Vision Research* 28.7, pp. 841–856.
- Bradley, A., Zhang, X., and Thibos, L. N. (1991). "Achromatizing the human eye". In: *Optometry and Vision Science* 68.8, pp. 608–616.
- Campbell, F. W. and Green, D. G. (1965). "Optical and retinal factors affecting visual resolution". In: *The Journal of Physiology* 181, pp. 576–593.
- Campbell, F. W. and Gubisch, R. W. (1967). "The effect of chromatic aberration on visual acuity." In: *The Journal of Physiology* 192.2, pp. 345–358.
- Campbell, F. (1957). "The depth of field of the human eye". In: *Optica Acta: International Journal of Optics* 4.4, pp. 157–164.
- Cánovas, C., Prieto, P. M., Manzanera, S., Mira, A., and Artal, P. (2010). "Hybrid adaptive-optics visual simulator". In: *Optics Letters* 35.2, pp. 196–198.
- Carkeet, A., Dong Luo, H., Tong, L., Mei Saw, S., and Tan, D. T. (2002). "Refractive error and monochromatic aberrations in Singaporean children". In: *Vision Research* 42.14, pp. 1809–1824.
- Chamot, S. R., Dainty, C., and Esposito, S. (2006). "Adaptive optics for ophthalmic applications using a pyramid wavefront sensor". In: *Optics Express* 14.2, pp. 518–526.
- Charman, W. N. (2005). "Aberrations and myopia". In: *Ophthalmic and Physiological Optics* 25.4, pp. 285–301.
- Chen, L., Artal, P., Gutierrez, D., and Williams, D. R. (2007). "Neural compensation for the best aberration correction". In: *Journal of Vision* 7.10, pp. 1–9.
- Cheng, X., Bradley, A., Hong, X., and Thibos, L. N. (2003). "Relationship between Refractive Error and Monochromatic Aberrations of the Eye". In: *Optometry and Vision Science* 80.1, pp. 43–49.
- Chui, T. Y., Yap, M. K., Chan, H. H., and Thibos, L. N. (2005). "Retinal stretching limits peripheral visual acuity in myopia". In: *Vision Research* 45.5, pp. 593–605.

- Collins, J. and Carney, L. (1990). "Visual performance in high myopia". In: *Current eye research* 9.3, pp. 217–223.
- Collins, M. J., Wildsoet, C. F., and Atchison, D. A. (1995). "Monochromatic aberrations and myopia". In: *Vision Research* 35.9, pp. 1157–1163.
- Curcio, C. A., Sloan, K. R., Kalina, R. E., and Hendrickson, A. E. (1990). "Human photoreceptor topography". In: *The Journal of Comparative Neurology* 292.4, pp. 497–523.
- Dalimier, E. and Dainty, C. (2005). "Comparative analysis of deformable mirrors for ocular adaptive optics". In: *Optics Express* 13.11, pp. 4275–4285.
- Daly, E. M. and Dainty, C. (2010). "Ophthalmic wavefront measurements using a versatile pyramid sensor". In: *Applied Optics* 49.31, G67–G77.
- Dehnert, A., Bach, M., and Heinrich, S. P. (2011). "Subjective visual acuity with simulated defocus". In: *Ophthalmic and Physiological Optics* 31.6, pp. 625–631.
- Delori, F. C., Webb, R. H., and Sliney, D. H. (2007). "Maximum permissible exposures for ocular safety (ANSI 2000), with emphasis on ophthalmic devices". In: *Journal of the Optical Society of America A* 24.5, pp. 1250–1265.
- Doble, N., Yoon, G., Chen, L., Bierden, P., Singer, B., Olivier, S., and Williams, D. R. (2002). "Use of a microelectromechanical mirror for adaptive optics in the human eye". In: *Optics Letters* 27.17, pp. 1537–1539.
- Dreher, A. W., Bille, J. F., and Weinreb, R. N. (1989). "Active optical depth resolution improvement of the laser tomographic scanner". In: *Applied Optics* 28.4, pp. 804–808.
- Elliott, E. (2016). *Using Physical Optics Propagation (POP), Part 2: Inspecting the beam intensities*.
- Engström, D., Persson, M., Bengtsson, J., and Goksör, M. (2013). "Calibration of spatial light modulators suffering from spatially varying phase response". In: *Optics Express* 21.13, pp. 16086–16103.
- Fernández, E. J. and Artal, P. (2003). "Membrane deformable mirror for adaptive optics: performance limits in visual optics". In: *Optics Express* 11.9, pp. 1056–1069.
- (2005). "Study on the effects of monochromatic aberrations in the accommodation response by using adaptive optics". In: *Journal of the Optical Society of America A* 22.9, pp. 1732–1738.

- (2017). “Achromatic doublet intraocular lens for full aberration correction”. In: *Biomedical Optics Express* 8.5, pp. 2396–2404.
- Fernández, E. J. and Drexler, W. (2005). “Influence of ocular chromatic aberration and pupil size on transverse resolution in ophthalmic adaptive optics optical coherence tomography”. In: *Optics Express* 13.20, pp. 8184–8197.
- Fernández, E. J., Iglesias, I., and Artal, P. (2001). “Closed-loop adaptive optics in the human eye”. In: *Optics Letters* 26.10, pp. 746–748.
- Fernández, E. J., Prieto, P. M., and Artal, P. (2009a). “Binocular adaptive optics visual simulator”. In: *Optics Letters* 34.17, pp. 2628–2630.
- Fernández, E. J., Prieto, P. M., and Artal, P. (2009b). “Wave-aberration control with a liquid crystal on silicon (LCOS) spatial phase modulator”. In: *Optics Express* 17.13, pp. 11013–11025.
- (2010). “Adaptive optics binocular visual simulator to study stereopsis in the presence of aberrations”. In: *Journal of the Optical Society of America A* 27.11, A48–A55.
- Fernández, E. J., Unterhuber, A., Prieto, P. M., Hermann, B., Drexler, W., and Artal, P. (2005a). “Ocular aberrations as a function of wavelength in the near infrared measured with a femtosecond laser”. In: *Optics Express* 13.2, pp. 400–409.
- Fernández, E. J., Považay, B., Hermann, B., Unterhuber, A., Sattmann, H., Prieto, P. M., Leitgeb, R., Ahnelt, P., Artal, P., and Drexler, W. (2005b). “Three-dimensional adaptive optics ultrahigh-resolution optical coherence tomography using a liquid crystal spatial light modulator”. In: *Vision Research* 45.28, pp. 3432–3444.
- Fernández, E. J., Vabre, L., Hermann, B., Unterhuber, A., Považay, B., and Drexler, W. (2006a). “Adaptive optics with a magnetic deformable mirror: applications in the human eye”. In: *Optics Express* 14.20, pp. 8900–8917.
- Fernández, E. J., Unterhuber, A., Považay, B., Hermann, B., Artal, P., and Drexler, W. (2006b). “Chromatic aberration correction of the human eye for retinal imaging in the near infrared”. In: *Optics Express* 14.13, pp. 6213–6225.

- Flitcroft, D. I. (1989). "The interactions between chromatic aberration, defocus and stimulus chromaticity: implications for visual physiology and colorimetry". In: *Vision Research* 29.3, pp. 349–360.
- Flitcroft, D. I., He, M., Jonas, J. B., Jong, M., Naidoo, K., Ohno-Matsui, K., Rahi, J., Resnikoff, S., Vitale, S., and Yannuzzi, L. (2019). "IMI – Defining and Classifying Myopia: A Proposed Set of Standards for Clinical and Epidemiologic Studies". In: *Investigative Ophthalmology & Visual Science* 60.3, pp. M20–M30.
- Flitcroft, D. (2012). "The complex interactions of retinal, optical and environmental factors in myopia aetiology". In: *Progress in Retinal and Eye Research* 31.6, pp. 622–660.
- Franchini, A. (2007). "Compromise between spherical and chromatic aberration and depth of focus in aspheric intraocular lenses". In: *Journal of Cataract and Refractive Surgery* 33.3, pp. 497–509.
- Francisco Castejón-Mochón, J., López-Gil, N., Benito, A., and Artal, P. (2002). "Ocular wave-front aberration statistics in a normal young population". In: *Vision Research* 42.13, pp. 1611–1617.
- Graef, K. and Schaeffel, F. (2012). "Control of accommodation by longitudinal chromatic aberration and blue cones". In: *Journal of Vision* 12.1, pp. 1–14.
- Guirao, A. and Williams, D. R. (2003). "A method to predict refractive errors from wave aberration data". In: *Optometry and Vision Science* 80.1, pp. 36–42.
- Hansen, G. (1943). "Zur Kenntnis des physiologischen Apertur-Farbefektes (Sfites-Crawford-Effekt IL Art)". In: *Naturwissenschaften* 31, pp. 416–417.
- Hardy, J. W., Lefebvre, J. E., and Koliopoulos, C. L. (1977). "Real-time atmospheric compensation". In: *Journal of the Optical Society of America* 67.3, pp. 360–369.
- He, J. C., Sun, P., Held, R., Thorn, F., Sun, X., and Gwiazda, J. E. (2002). "Wavefront aberrations in eyes of emmetropic and moderately myopic school children and young adults". In: *Vision Research* 42.8, pp. 1063–1070.
- Heel, A. C. S. van (1946). "Correcting the Spherical and Chromatic Aberrations of the Eye". In: *Journal of the Optical Society of America* 36.4, pp. 237–239.

- Helmholtz, H. von (1873). *Popular lectures on scientific subjects*.
- Hemenger, R. P., Garner, L. F., and Ooi, C. S. (1995). "Change with age of the refractive index gradient of the human ocular lens". In: *Investigative Ophthalmology & Visual Science* 36.3, pp. 703–707.
- Hermann, B., Fernández, E. J., Unterhuber, A., Sattmann, H., Fercher, A. F., Drexler, W., Prieto, P. M., and Artal, P. (2004). "Adaptive-optics ultrahigh-resolution optical coherence tomography". In: *Optics Letters* 29.18, pp. 2142–2144.
- Hofer, H, Chen, L, Yoon, G. Y., Singer, B, Yamauchi, Y, and Williams, D. R. (2001a). "Improvement in retinal image quality with dynamic correction of the eye's aberrations". In: *Optics Express* 8.11, pp. 631–643.
- Hofer, H., Artal, P., Singer, B., Aragón, J. L., and Williams, D. R. (2001b). "Dynamics of the eye's wave aberration". In: *Journal of the Optical Society of America A* 18.3, pp. 497–506.
- Holden, B. A., Fricke, T. R., Wilson, D. A., Jong, M., Naidoo, K. S., Sankaridurg, P., Wong, T. Y., Naduvilath, T. J., and Resnikoff, S. (2016). "Global Prevalence of Myopia and High Myopia and Temporal Trends from 2000 through 2050". In: *Ophthalmology* 123.5, pp. 1036–1042.
- Holst, G. and Lomheim, T. S. (2007). *CMOS/CCD sensors and camera systems, Second Edition*, p. 408.
- Howarth, P. A. and Bradley, A. (1986). "The longitudinal chromatic aberration of the human eye, and its correction". In: *Vision Research* 26.2, pp. 361–366.
- Howarth, P. A. (1984). "The lateral chromatic aberration of the eye". In: *Ophthalmic and Physiological Optics* 4.3, pp. 223–226.
- Iglesias, I., Ragazzoni, R., Julien, Y., and Artal, P. (2002). "Extended source pyramid wave-front sensor for the human eye". In: *Optics Express* 10.9, pp. 419–428.
- Iwase, A., Araie, M., Tomidokoro, A., Yamamoto, T., Shimizu, H., and Kitazawa, Y. (2006). "Prevalence and Causes of Low Vision and Blindness in a Japanese Adult Population." In: *Ophthalmology* 113.8, pp. 1354–1362.
- Johnson, C. A. and Casson, E. J. (1995). "Effects of Luminance, Contrast, and Blur on Visual Acuity.pdf". In: *Optometry and Vision Science* 72.12, pp. 864–869.

- Kruger, P. B. and Pola, J. (1986). "Stimuli for accommodation: blur, chromatic aberration and size". In: *Vision Research* 26.6, pp. 957–971.
- Kruger, P. B., Mathews, S., Aggarwala, K. R., and Sanchez, N. (1993). "Chromatic aberration and ocular focus: Fincham revisited". In: *Vision Research* 33.10, pp. 1397–1411.
- Li, S., Xiong, Y., Li, J., Wang, N., Dai, Y., Xue, L., Zhao, H., Jiang, W., Zhang, Y., and He, J. C. (2009). "Effects of Monochromatic Aberration on Visual Acuity Using Adaptive Optics". In: *Optometry and Vision Science* 86.7, pp. 868–874.
- Liang, J., Williams, D. R., and Miller, D. T. (1997). "Supernormal vision and high-resolution retinal imaging through adaptive optics". In: *Journal of the Optical Society of America A* 14.11, pp. 2884–2892.
- Liang, J., Grimm, B., Goelz, S., and Bille, J. F. (1994). "Objective measurement of wave aberrations of the human eye with the use of a Hartmann-Shack wave-front sensor". In: *Journal of the Optical Society of America A* 11.7, pp. 1949–1957.
- Llorente, L., Diaz-santana, L., Lara-saucedo, D., and Marcos, S. (2003). "Aberrations of the Human Eye in Visible and". In: *Optometry and Vision Science* 80.1, pp. 26–35.
- Lundström, L., Manzanera, S., Prieto, P. M., Ayala, D. B., Gorceix, N., Gustafsson, J., Unsbo, P., and Artal, P. (2007). "Effect of optical correction and remaining aberrations on peripheral resolution acuity in the human eye". In: *Optics Express* 15.20, pp. 12654–12661.
- Manzanera, S. and Artal, P. (2016). "Minimum change in spherical aberration that can be perceived". In: *Biomedical Optics Express* 7.9, pp. 3471–3477.
- Manzanera, S., Prieto, P. M., Ayala, D. B., Lindacher, J. M., and Artal, P. (2007). "Liquid crystal adaptive optics visual simulator: application to testing and design of ophthalmic optical elements". In: *Optics Express* 15.24, pp. 16177–16188.
- Marcos, S., Moreno, E., and Navarro, R. (1999). "The depth-of-field of the human eye from objective and subjective measurements". In: *Vision Research* 39.12, pp. 2039–2049.

- Marcos, S., Burns, S. A., Moreno-Barriusop, E., and Navarro, R. (1999). "A new approach to the study of ocular chromatic aberrations". In: *Vision Research* 39.26, pp. 4309–4323.
- Marsack, J. D., Thibos, L. N., and Applegate, R. A. (2004). "Metrics of optical quality derived from wave aberrations predict visual performance". In: *Journal of Vision* 4.4, pp. 322–328.
- Martínez, J. L., Moreno, I., del Mar Sánchez-López, M., Vargas, A., and García-Martínez, P. (2014). "Analysis of multiple internal reflections in a parallel aligned liquid crystal on silicon SLM". In: *Optics Express* 22.21, pp. 25866–25879.
- Martínez, J. L., Fernández, E. J., Prieto, P. M., and Artal, P. (2016). "Interferometric method for phase calibration in liquid crystal spatial light modulators using a self-generated diffraction-grating". In: *Optics Express* 24.13, pp. 14159–14171.
- Martínez, J. L., Fernández, E. J., Prieto, P. M., and Artal, P. (2017). "Chromatic aberration control with liquid crystal spatial phase modulators". In: *Optics Express* 25.9, pp. 9793–9801.
- Mclellan, J. S., Marcos, S., Prieto, P. M., and Burns, S. A. (2002). "Imperfect optics may be the eye's defence against chromatic blur". In: *Nature* 417.May, pp. 174–176.
- Merino, D., Dainty, C., Bradu, A., and Podoleanu, A. G. (2006). "Adaptive optics enhanced simultaneous en-face optical coherence tomography and scanning laser ophthalmoscopy". In: *Optics Express* 14.8, pp. 3345–3353.
- Miller, D. T., Thibos, L. N., and Hong, X. (2005). "Requirements for segmented correctors for diffraction-limited performance in the human eye". In: *Optics Express* 13.1, pp. 275–289.
- Miller, D. T., Qu, J., Jonnal, R. S., and Thorn, K. E. (2003). "Coherence gating and adaptive optics in the eye". In: *Coherence Domain Optical Methods and Optical Coherence Tomography in Biomedicine VII* 4956, pp. 65–72.
- Millidot, M. (1981). "Effect of Ametropia on Peripheral Refraction". In: *American Journal of Optometry & Physiological Optics* 58.9, pp. 691–695.

- Mitry, D., Charteris, D. G., Fleck, B. W., Campbell, H., and Singh, J. (2010). "The epidemiology of rhegmatogenous retinal detachment: Geographical variation and clinical associations". In: *British Journal of Ophthalmology* 94.6, pp. 678–684.
- Morgan, I. G., Ohno-Matsui, K., and Saw, S.-M. (2012). "Myopia". In: *The Lancet* 379.9827, pp. 1739–1748.
- Pan, C.-W., Dirani, M., Cheng, C.-Y., Wong, T.-Y., and Saw, S.-M. (2015). "The age-specific prevalence of myopia in Asia: A meta-analysis". In: *Optometry and Vision Science* 92.3, pp. 258–266.
- Paquin, M. P., Hamam, H, and Simonet, P (2002). "Objective measurement of optical aberrations in myopic eyes". In: *Optometry and Vision Science* 79.1040-5488, pp. 285–291.
- Pérez-Merino, P., Dorronsoro, C., Llorente, L., Durán, S., Jiménez-Alfaro, I., and Marcos, S. (2013). "In vivo chromatic aberration in eyes implanted with intraocular lenses". In: *Investigative Ophthalmology & Visual Science* 54.4, pp. 2654–2661.
- Piers, P. A., Fernández, E. J., Manzanera, S., Norrby, S., and Artal, P. (2004). "Adaptive optics simulation of intraocular lenses with modified spherical aberration". In: *Investigative Ophthalmology & Visual Science* 45.12, pp. 4601–4610.
- Piers, P. A., Manzanera, S., Prieto, P. M., Gorceix, N., and Artal, P. (2007). "Use of adaptive optics to determine the optimal ocular spherical aberration". In: *Journal of Cataract & Refractive Surgery* 33.10, pp. 1721–1726.
- Pircher, M, Zawadzki, R. J., Evans, J. W., Werner, J. S., and Hitzenberger, C. K. (2008). "Simultaneous imaging of human cone mosaic with adaptive optics enhanced scanning laser ophthalmoscopy and high-speed transversal scanning optical coherence tomography". In: *Optics Letters* 33.1, pp. 22–24.
- Platt, B. and Shack, R. V. (1971). "Lenticular Hartmann screen". In: *Newsletter* 5, p. 15.
- Porter, J., Guirao, A., Cox, I. G., and Williams, D. R. (2001). "Monochromatic aberrations of the human eye in a large population". In: *Journal of the Optical Society of America A* 18.8, pp. 1793–1803.
- Powell, I. (1981). "Lenses for correcting chromatic aberration of the eye". In: *Applied Optics* 20.24, pp. 4152–4155.

- Prieto, P. M., Fernández, E. J., Manzanera, S., and Artal, P. (2004). "Adaptive optics with a programmable phase modulator: applications in the human eye". In: *Optics Express* 12.17, pp. 4059–4071.
- Primot, J. (2003). "Theoretical description of Shack–Hartmann wave-front sensor". In: *Optics Communications* 222.1-6, pp. 81–92.
- Radhakrishnan, A., Dorronsoro, C., and Marcos, S. (2016). "Differences in visual quality with orientation of a rotationally asymmetric bifocal intraocular lens design". In: *Journal of Cataract & Refractive Surgery* 42.9, pp. 1276–1287.
- Ravikumar, S., Thibos, L. N., and Bradley, A. (2008). "Calculation of retinal image quality for polychromatic light". In: *Journal of the Optical Society of America A* 25.10, pp. 2395–2407.
- Reichelt, S. (2013). "Spatially resolved phase-response calibration of liquid-crystal-based spatial light modulators". In: *Applied Optics* 52.12, pp. 2610–2618.
- Roddier, F. (1988). "Curvature sensing and compensation: a new concept in adaptive optics". In: *Applied Optics* 27.7, pp. 1223–1225.
- Roorda, A. (2011). "Adaptive optics for studying visual function: A comprehensive review". In: *Journal of Vision* 11.5, pp. 1–21.
- Roorda, A. and Williams, D. R. (1999). "The arrangement of the three cone classes in the living human eye". In: *Nature* 397.6719, pp. 520–522.
- Roorda, A., Romero-Borja, F., Donnelly III, W. J., Queener, H., Hebert, T. J., and Campbell, M. C. (2002). "Adaptive optics scanning laser ophthalmoscopy". In: *Optics Express* 10.9, pp. 405–412.
- Rose, A. (1948). "The sensitivity performance of the human eye on an absolute scale". In: *Journal of the Optical Society of America* 38.2, p. 196.
- Rose, K. A., Morgan, I. G., Smith, W., Burlutsky, G., Mitchell, P., and Saw, S.-M. (2008). "Myopia, Lifestyle, and Schooling in Students of Chinese Ethnicity in Singapore and Sydney". In: *Archives of Ophthalmology* 126.4, pp. 527–530.
- Rossi, E. A., Weiser, P., Tarrant, J., and Roorda, A. (2007). "Visual performance in emmetropia and low myopia after correction of high-order aberrations". In: *Journal of Vision* 7.8, pp. 1–14.
- Rynders, M., Lidkea, B., Chisholm, W., and Thibos, L. N. (1995). "Statistical distribution of foveal transverse chromatic aberration, pupil centration,

- and angle ψ in a population of young adult eyes". In: *Journal of the Optical Society of America A* 12.10, pp. 2348–2357.
- Sabesan, R. and Yoon, G. (2009). "Visual performance after correcting higher order aberrations in keratoconic eyes". In: *Journal of Vision* 9.5, pp. 1–10.
- Sabesan, R. and Yoon, G. (2010). "Neural compensation for long-term asymmetric optical blur to improve visual performance in keratoconic eyes". In: *Investigative Ophthalmology & Visual Science* 51.7, pp. 3835–3839.
- Sabesan, R., Jeong, T. M., Carvalho, L., Cox, I. G., Williams, D. R., and Yoon, G. (2007). "Vision improvement by correcting higher-order aberrations with customized soft contact lenses in keratoconic eyes". In: *Optics Letters* 32.8, pp. 1000–1002.
- Salmon, T. O. and Pol, C. van de (2006). "Normal-eye Zernike coefficients and root-mean-square wavefront errors". In: *Journal of Cataract & Refractive Surgery* 32.12, pp. 2064–2074.
- Saw, S. M., Gazzard, G., Shin-Yen, E. C., and Chua, W. H. (2005). "Myopia and associated pathological complications". In: *Ophthalmic and Physiological Optics* 25.5, pp. 381–391.
- Sawides, L., Marcos, S., Ravikumar, S., Thibos, L. N., Bradley, A., and Webster, M. (2010a). "Adaptation to astigmatic blur". In: *Journal of Vision* 10.12, pp. 1–15.
- Sawides, L., Gamba, E., Pascual, D., Dorronsoro, C., and Marcos, S. (2010b). "Visual performance with real-life tasks under adaptive-optics ocular aberration correction". In: *Journal of Vision* 10.5, pp. 1–12.
- Schnapf, J. L., Kraft, T. W., and Baylor, D. A. (1987). "Spectral sensitivity of human cone photoreceptors". In: *Nature* 325.6103, pp. 439–441.
- Schwarz, C., Prieto, P. M., Fernández, E. J., and Artal, P. (2011). "Binocular adaptive optics vision analyzer with full control over the complex pupil functions". In: *Optics Letters* 36.24, pp. 4779–4781.
- Snyder, A. W. and Pask, C. (1973). "The Stiles-Crawford effect - explanation and consequences". In: *Vision Research* 13.6, pp. 1115–1137.
- Stiles, W. S. (1937). "The luminous efficiency of monochromatic rays entering the eye pupil at different points and a new colour effect". In: *Proceedings of the Royal Society of London. Series B - Biological Sciences* 123.830, pp. 90–118.

- Stiles, W. S. and Crawford, B. H. (1933). "The luminous efficiency of rays entering the eye pupil at different points". In: *Proceedings of the Royal Society B: Biological Sciences* 112.778, pp. 428–450.
- Strang, N. C., Winn, B., and Bradley, A. (1998). "The role of neural and optical factors in limiting visual resolution in myopia". In: *Vision Research* 38.11, pp. 1713–1721.
- Taberner, J. and Artal, P. (2012). "Optical modeling of a corneal inlay in real eyes to increase depth of focus: Optimum centration and residual defocus". In: *Journal of Cataract & Refractive Surgery* 38.2, pp. 270–277.
- Thibos, L. N., Cheney, F. E., and Walsh, D. J. (1987). "Retinal limits to the detection and resolution of gratings." In: *Journal of the Optical Society of America A* 4.8, pp. 1524–1529.
- Thibos, L. N., Bradley, A., Still, D. L., Zhang, X., and Howarth, P. A. (1990). "Theory and measurement of ocular chromatic aberration". In: *Vision Research* 30.1, pp. 33–49.
- Thibos, L. N. (1987). "Calculation of the influence of lateral chromatic aberration on image quality across the visual field." In: *Journal of the Optical Society of America A* 4.8, pp. 1673–1680.
- Thibos, L. N., Bradley, A., and Zhang, X. (1991). "Effect of ocular chromatic aberration on monocular visual performance". In: *Optometry and Vision Science* 68.8, pp. 599–607.
- Thibos, L. N., Wheeler, W., and Horner, D. (1997). "Power vectors: an application of Fourier analysis to the description and statistical analysis of refractive error". In: *Optometry and Vision Science* 75.6, pp. 367–375.
- Thibos, L. N., Ye, M., Zhang, X., and Bradley, A. (1992). "The chromatic eye: a new reduced-eye model of ocular chromatic aberration in humans". In: *Applied Optics* 31.19, pp. 3594–3600.
- Thibos, L. N., Hong, X., Bradley, A., and Cheng, X. (2002). "Statistical variation of aberration structure and image quality in a normal population of healthy eyes". In: *Journal of the Optical Society of America A* 19.12, pp. 2329–2348.
- Thibos, L. N., Hong, X., Bradley, A., and Applegate, R. A. (2004). "Accuracy and precision of objective refraction from wavefront aberrations." In: *Journal of Vision* 4.4, pp. 329–351.

- Thomson, L. C. and Wright, W. D. (1947). "The colour sensitivity of the retina within the central fovea of man". In: *The Journal of Physiology* 105.4, pp. 316–331.
- Travinsky, A., Vorobiev, D., Ninkov, Z., Raisanen, A., Quijada, M. A., Smee, S. A., Pellish, J. A., Schwarz, T., Robberto, M., Heap, S., Conley, D., Benavides, C., Garcia, N., Bredl, Z., and Yllanes, S. (2017). "Evaluation of digital micromirror devices for use in space-based multiobject spectrometer application". In: *Journal of Astronomical Telescopes, Instruments, and Systems* 3.3, p. 035003.
- Vargas-Martín, F., Prieto, P. M., and Artal, P. (1998). "Correction of the aberrations in the human eye with a liquid-crystal spatial light modulator: limits to performance". In: *Journal of the Optical Society of America A* 15.9, pp. 2552–2562.
- Venkataraman, A. P., Winter, S., Unsbo, P., and Lundström, L. (2015). "Blur adaptation: Contrast sensitivity changes and stimulus extent". In: *Vision Research* 110.Part A, pp. 100–106.
- Villegas, E. A., Alcón, E., Mirabet, S., Yago, I., Marín, J. M., and Artal, P. (2014). "Extended depth of focus with induced spherical aberration in light-adjustable intraocular lenses". In: *American Journal of Ophthalmology* 157.1, pp. 142–149.
- Vitale, S., Ellwein, L., Cotch, M. F., Ferris, F. L., and Sperduto, R. (2008). "Prevalence of refractive error in the United States, 1999-2004". In: *Archives of Ophthalmology* 126.8, pp. 1111–1119.
- Wang, B. and Ciuffreda, K. J. (2006). "Depth-of-focus of the human eye: theory and clinical implications". In: *Survey of Ophthalmology* 51.1, pp. 75–85.
- Watson, A. B. and Fitzhugh, A. (1990). "The method of constant stimuli is inefficient". In: *Perception & Psychophysics* 47.1, pp. 87–91.
- Watson, A. B. and Pelli, D. G. (1983). "Quest: A Bayesian adaptive psychometric method". In: *Perception & Psychophysics* 33.2, pp. 113–120.
- Xun, X. and Cohn, R. W. (2004). "Phase calibration of spatially nonuniform spatial light modulators". In: *Applied Optics* 43.35, pp. 6400–6406.
- Yoon, G.-Y. and Williams, D. R. (2002). "Visual performance after correcting the monochromatic and chromatic aberrations of the eye". In: *Journal of the Optical Society of America A* 19.2, pp. 266–275.

- Zawadzki, R. J., Choi, S. S., Jones, S. M., Oliver, S. S., and Werner, J. S. (2007). "Adaptive optics-optical coherence tomography: optimizing visualization of microscopic retinal structures in three dimensions". In: *Journal of the Optical Society of America A* 24.5, pp. 1373–1383.
- Zawadzki, R. J., Jones, S. M., Pilli, S., Balderas-Mata, S., Kim, D. Y., Olivier, S. S., and Werner, J. S. (2011). "Integrated adaptive optics optical coherence tomography and adaptive optics scanning laser ophthalmoscope system for simultaneous cellular resolution in vivo retinal imaging". In: *Biomedical Optics Express* 2.6, pp. 1674–1686.
- Zhang, X., Bradley, A., and Thibos, L. N. (1991). "Achromatizing the human eye: the problem of chromatic parallax". In: *Journal of the Optical Society of America A* 8.4, pp. 686–691.
- Zhang, X., Thibos, L. N., and Bradley, A. (1997). "Wavelength-dependent magnification and polychromatic image quality in eyes corrected for longitudinal chromatic aberration". In: *Optometry and Vision Science* 74.7, pp. 563–569.
- Zhang, X., Ye, M., Bradley, A., and Thibos, L. N. (1999). "Apodization by the Stiles–Crawford effect moderates the visual impact of retinal image defocus". In: *Journal of the Optical Society of America A* 16.4, pp. 812–820.
- Zhang, Y., Cense, B., Rha, J., Jonnal, R. S., Gao, W., Zawadzki, R. J., Werner, J. S., Jones, S., Olivier, S., and Miller, D. T. (2006). "High-speed volumetric imaging of cone photoreceptors with adaptive optics spectral-domain optical coherence tomography". In: *Optics Express* 14.10, pp. 4380–4394.
- Zhang, Z. (1994). "Simple method for measuring phase modulation in liquid crystal televisions". In: *Optical Engineering* 33.9, pp. 3018–3022.
- Zhang, Z., You, Z., and Chu, D. (2014). "Fundamentals of phase-only liquid crystal on silicon (LCOS) devices". In: *Light: Science and Applications* 3.10, pp. 1–10.
- Zou, W., Qi, X., and Burns, S. A. (2008). "Dual-Deformable-Mirror Adaptive-Optics System". In: 33.22, pp. 2602–2604.

Acknowledgements

At the end of this manuscript, and at the end of my PhD journey, I would like to look back at my three years in Laboratorio de Optica de Universidad de Murcia – I'll call it LOUM from here on – which have passed much faster than I expected. Of course, the most important thing in any lab is the people. And, needless to say, none of the things that are written in thesis would've been possible without my fellow lab members helping me along the way.

First of all, I'd like express a special gratitude to Pablo, for giving me the opportunity to be a part of LOUM, and guiding me along. It has been a pleasure to be in the group that you have built from the ground up, with all the brilliant people working on a common goal. Thank you for all the scientific advice, for giving me the motivation to try and do my best, and, of course, for passing all wine-making knowledge.

I'd like to give a huge thank you to Josua for being a best supervisor I could've hoped for. Thanks for all the countless discussions we've had, which have helped me tremendously in these three years. Whenever I thought I've done everything I could when trying to solve some problem, you always had a suggestion that moved me forward. And thank you for being not just a supervisor, but also a friend.

I want to express my gratitude to all the LOUM members, past and present: Silvestre, for always having an answer to any question, and for being my most loyal subject; Pedro, for all our useful discussions; Juanma, for the funny stories in the kitchen; Eloy and Juan for having patience to be subjects in my time-consuming experiments. Thanks to all the people with whom I've shared the office with during my time in the lab - Fran, Dimitrios, Rahul, Alba and Rosa. Thanks to Adrian and Javi, who have always helped me with the software. A special gratitude to Carmen, who always helped me with complicated bureaucracy, without whom I definitely wouldn't be able to finish my studies. Thanks to all the people I've spent my time in the lab with, in no particular order: Dani, Esther, Augusto, Dibyendu, Vahid, Consu, Raul, Yiwei, Ben, Manu, Alberto, Lucie, Alex, Jose Luis, Martin – hopefully I haven't forgotten anyone.

Of course, I have to talk about Voptica, my second home base, where I had an opportunity to see scientific ideas being brought to the industry. And

of course, I would like to thank everyone with whom I've been working there. Firstly, enormous thanks to Rosa, who helped me with the countless paperwork – I would've never been able to figure it out by myself. Thank you to Luis, Lucia and Consu (again) for the fun time in ESCRS conferences where we had to play salesmen. Thanks to Jose, Roberto, Maria, Bart, Carmela, Paloma – even if I only had a chance to work briefly with some of you. Shoutout to Javi, who has also helped me in Voptica after helping me in LOUM.

This whole journey started because of the Marie Curie network I was a part of – Myopia: fundamental understanding needed, or MyFUN (even if I'm still not completely sold on that name). I think I am also contractually obligated to mention the grant agreement number – 675137... With the formalities out of the way, I'd like to thank all the people involved in the network. Special thanks to Brian in UCD and Linda in KTH, for hosting me during exchange visits, and to other principal investigators: Frank, Susana, and Saggi. Huge thank you to the fellows, with whom I've shared lots of fun times: Andrea, Alessandra, Pablo, Miguel, Vahid, Sandra, Geethika, Petros, Dibyendu, Dmitry, Najnin, Barbara, and Shrilekha.

On a more personal note, I would like to thank my mom – Lena, who has always been supporting me, even if I was far away – I know that wasn't easy. And thank you to my uncle Volodya, who's also given the moral support any time I needed it. I know you want me to stay in Murcia for a bit longer, just to have an excuse to visit Spain a few more times, hahaha.

And finally, a special thanks to Patri, my favourite pink elephant, for being in my life. You have helped me through the difficult times, you have shared the amazing times, and you have always made me happy.